



THE UNIVERSITY  
*of* ADELAIDE

**Thermal Performance of the  
Solar Expanding Vortex Receiver (SEVR)**

**Daniel J. T. Ang**

*A thesis submitted for fulfilment of the requirements for the degree of  
Master of Philosophy*

Centre for Energy Technology  
School of Mechanical Engineering  
The University of Adelaide  
Australia

**1<sup>st</sup> August 2021**

## Abstract

A novel windowless configuration of the Solar Expanding Vortex Receiver (SEVR) has been proposed to heat particles used in industrial applications, such as particle heaters, mineral-processing devices, and air heaters. Understanding the influence of different parameters on the thermal performance of the SEVR is essential for the success of the integration of the receiver for the generation of industrial process heat in potential applications such as the Bayer process in alumina production. However, there is a lack of understanding of the effects of some key dimensionless parameters and flow regimes on the thermal performance of the SEVR. Furthermore, most studies on the SEVR have been conducted under isothermal conditions, and there is a lack of analysis and understanding of the thermal performance of the SEVR, which is critical for the operational requirements in any industrial process.

This project aims to provide a new understanding of the thermal performance of the windowless vortex-based solar receiver under high-flux solar radiation by demonstrating the influence of critical parameters and flow regimes in single and two-phase flow conditions using both experimental and numerical methods. More specifically, the objective of the current study is to assess the thermal performance with an aerodynamic control strategy within a windowless SEVR under single-phase conditions. Meanwhile, the two-phase flow study seeks to characterise the essential influencing dimensionless parameters (particle loading, Froude and Stokes number) of initial inflow conditions on the reactor's thermal efficiency and heat transfer.

In the single-phase flow study, a proof-of-concept experimental study was conducted to assess the effects of overventilation on the thermal performance of the receiver by employing a 5-kW<sub>el</sub> single-lamp Xenon arc solar simulator. A primary aerodynamic control strategy was developed based on the application of suction to the outlet section of the device. It was utilized to prevent particle egress from the device through the windowless aperture. The influence of the air inlet mass flowrate and suction level on the thermal performance (thermal efficiency, heat losses and wall temperature distribution) was investigated. It was found that the trade-off between the suction level and thermal efficiency needs to be cautiously considered to prevent exergy destruction in the reactor.

In the two-phase flow study, the systematic research assesses the coupled influence of particle loading, Froude, and Stokes numbers through variation of the inlet volumetric flowrate, particle

size and loading on the performance of the SEVR under steady-state conditions. The experiments employ polydisperse CARBO CP ceramic particles heated with an 18-kW<sub>el</sub> Metal Halide three-lamp solar simulator. A numerical study was also performed using computational fluid dynamics (CFD) software ANSYS/CFX 2019 R1. It was found that the volumetric particle loading and Froude number have primary controlling influence, while the Stokes number has a secondary impact on the thermal performance for these conditions. Overall thermal efficiency of 67% was obtained under high particle loading and Froude numbers.

## Declaration

I, Daniel Ang, certify that this work, *Thermal Performance of the Solar Expanding Vortex Receiver (SEVR)*, contains no material which has been accepted for the award of any other degree or diploma in any university or other tertiary institution and, to the best of my knowledge and belief, contains no material previously published or written by another person, except where due reference has been made in the text. In addition, I certify that no part of this work will, in the future, be used in a submission in my name for any other degree or diploma in any university or other tertiary institution without the prior approval of the University of Adelaide and where applicable, any partner institution responsible for the joint award of this degree.

I acknowledge that the copyright of published works contained within this thesis resides with the copyright holder(s) of those works.

I give permission for the digital version of my thesis to be made available on the web, via the University's digital search repository, the Library Search and also through web search engines, unless permission has been granted by the University to restrict access for a period of time.

I also acknowledge the support I have received for my research through the provision of a Divisional Scholarship by the Faculty of ECMS, The University of Adelaide, as well as the funding from the ARENA research program *RND054: Integrating CST into the Bayer Process*.

X

---

Daniel J.T. Ang

## **Acknowledgements**

I would like to acknowledge my supervisors Dr Zhao Tian, Dr Woei Saw, and Prof. Gus Nathan in guiding me throughout this journey and for giving me an opportunity to work on this project. I would like to begin by thanking my principal supervisor, Dr Zhao, for sharing his expertise and knowledge on CFD numerical modelling. Apart from that, he has given me quite some handful of motivation and encouragement throughout my candidature, which helped me to become a more independent and professional researcher (Thank you for mentoring me throughout the process). Next, I would like to acknowledge my co-supervisor, Dr Saw, for his guidance in the experimental work and his eagerness to help me and meet deadlines, as well as sharing his knowledge on solar thermal systems and thermodynamics throughout the project (Thank you also for giving me encouragement and practical advice when I am encountering challenging obstacles). I would also like to acknowledge my co-supervisor, Professor Gus, for sharing his extensive knowledge in solar thermal technology and emphasizing the importance of dimensionless parameters in scientific research and for his help to improve my technical writing skills (Thank you also for giving me the divisional scholarship to work on this project). Furthermore, special thanks to Dr Alfonso Chinnici for his guidance and support throughout the project in both paper planning and experimental setup, as well as sharing his knowledge on the vortex flow solar receiver technology (Thank you for your eagerness to help me in meeting deadlines, as well as being my mentor and friend).

I would also like to thank all my colleagues and ex-colleagues: Dr Ling Yin, Dr Zhiwei Sun, Dr Timothy Lau, Mr Eyad Hassan, Houzhi, Gavin, Afifah, Shen Long, Heng Zheng, Yimin, Orddom, Yining, Shipu, Muna, Simon, Mujahid and those I did not forget but haven't mentioned, for giving me the encouragement and enlightenment throughout my research. Special thanks also to the workshop team as well as the team in Thebarton, Mr Marc Simpson, and Mr Darren Faulkner, for always helping in setting up the experiments on time and making sure that everything is safe in the lab.

Finally, I would like to thank my parents for their support and unconditional love. I would also like to thank all my friends who have given me support throughout my research, especially in these difficult times of the COVID-19 pandemic.

# Table of Contents

<i>Abstract</i>	<i>ii</i>
<i>Declaration</i>	<i>iv</i>
<i>Acknowledgements</i>	<i>v</i>
<i>Table of Contents</i>	<i>vi</i>
<i>List of Figures</i>	<i>viii</i>
<i>List of Tables</i>	<i>x</i>
<i>List of Publications</i>	<i>xi</i>
<i>Nomenclature</i>	<i>xii</i>
<i>Abbreviations</i>	<i>xiv</i>
<i>Chapter 1: Introduction</i>	<i>1</i>
1.1 Concentrating Solar Thermal and Vortex-based Solar Particle Reactor	1
1.2 The Solar Expanding Vortex Receiver (SEVR)	3
1.3 Thesis Structure	4
<i>Chapter 2 Literature Review</i>	<i>6</i>
2.1 Reactor Designs for Thermochemical Processes	6
2.2 Vortex-based Solar Cavity Receivers	8
2.2.1 Solar Vortex Receiver/Reactor (SVR)	8
2.2.2 Solar Expanding Vortex Receiver (SEVR)	8
2.2.3 A Windowless SEVR	9
2.3 Dimensionless Parameters	11
2.3.1 Reynolds Number	11
2.3.2 Froude Number	12
2.3.3 Stokes Number	13
2.3.4 Particle Loading Ratio	15
2.3.5 Swirl Number	16
2.4 Particle Residence Time Distribution	16
2.4.1 Particle Residence Time in Vortex-based Reactors	17
2.4.2 RTD study within the SEVR	18
2.5 Thermal Performance of Solar Receivers	20
2.5.1 Thermal Performance of Cavity Receivers	20
2.5.2 Thermal Performance Study in Vortex-based Receivers	21
2.6 Heat Transfer in Particle-laden Flows	22
2.7 Research Gaps	23
2.8 Aim and Objectives	24
<i>Chapter 3 Methodology</i>	<i>25</i>
3.1 Task Calibration and Setting up of the Three-Lamp Solar Simulator	26
3.1.1 Alignment of the Solar Simulator	26
3.1.2 Image Processing	27

3.1.3 Optical Calibration and Heat Flux Measurement	27
3.2 Experimental Study on Thermal Performance of the SEVR	31
3.2.1 Experimental Arrangement	31
3.2.2 Boundary Conditions	34
3.3 Proof-of-concept study on the effects of over-ventilation by suction	36
3.4 CFD Modelling of the Input Radiation Flux Profile	37
3.5 Numerical Model and Validation Results	38
3.6 Thermal Performance Analysis	43
3.7 Key Dimensionless Parameters	45
<i>Chapter 4 Experimental study on the thermal performance</i>	<i>47</i>
4.1 Single-phase study: Influence of overventilation by suction	47
4.1.1 Influence on wall temperature	47
4.1.2 Influence on outlet temperature	48
4.2 Two-phase study: Influence of key dimensionless parameters on wall temperature	51
4.3 Two-phase study: Influence of key dimensionless parameters on outlet temperature	54
4.3.1 Effects of Froude number	54
4.3.2 Effects of particle loading and Stokes number	57
4.4 Two-phase study: Influence of key dimensionless parameters on thermal efficiency and exergy factor	59
4.5 Two-phase study: Influence of key dimensionless parameters on the Fractional Convective, radiative heat losses	63
4.6 Two-phase study: Influence of key dimensionless inflow parameters on enthalpy ratio	67
<i>Chapter 5 Numerical study on the thermal performance</i>	<i>70</i>
5.1 Effects on outlet temperature	70
5.2 Effects on thermal efficiency	73
5.3 Temperature and particle distribution within the SEVR	75
5.4 Swirl number analysis	80
5.5 Normalised particle residence time	82
<i>Chapter 6 Conclusion and Future work</i>	<i>84</i>
6.1 Conclusion	84
6.2 Future work	86
<i>Reference</i>	<i>87</i>
<i>Appendix A – Journal Submitted to Renewable Energy Journal</i>	<i>92</i>

## List of Figures

Figure 1. Principle of the (a) beam-up, (b) beam-down concentrated solar system configuration [8,9].	2
Figure 2. Schematic Diagram of the Solar Expanding Vortex Receiver (SEVR).	4
Figure 3. Some Examples of Solar Thermochemical Receivers: (a) packed bed [26] (b) Fluidised bed [27] (c) vortex-flow [11].	7
Figure 4. Simplified schematic diagram of key flow features identified for the windowless SEVR [37].	10
Figure 5. Pictorial demonstration on the effect of Stokes number in turbulent flows [42].	14
Figure 6. Regimes of interaction between particles and fluid phase, here $\tau_e$ is the turnover time of large eddy, while $\tau_K$ is the Kolmogorov timescale [44].	15
Figure 7. An example of measured RTD of the SEVR under isothermal conditions at a constant particle size of $80\mu\text{m}$ with variation of inlet flow velocities [40].	18
Figure 8. Demonstration of SEVR behaviour derived from experimental and numerical analyses of the three-dimensional flow-field within the SEVR in both (a) Froude-Stokes and (b) cyclonic regimes [40].	19
Figure 9. Three-Lamp Solar Simulator (left), solar simulator under operation (right).	26
Figure 10. (a) Schematic diagram of the Lambertian target, (b) Reference position taken for the heat flux map.	28
Figure 11. Calibration graph of the Radiative heat flux of the three-lamp solar simulator.	29
Figure 12. Three-lamp solar simulator flux profile generated at the Lambertian target (focal point, aperture plane).	30
Figure 13: (a) Schematic Diagram of the SEVR (b) Geometrical details of the SEVR (c) arrangement of the SEVR experimental rig for the thermal performance study (Modified from earlier work [75]).	33
Figure 14. Particle screw feeder calibration graph for three different particle sizes.	34
Figure 15: Radiation Flux profile at the aperture plane generated by the numerical study.	37
Figure 16. Simulated outlet temperatures at 3 different mesh sizes for various inlet mass flowrates under single-phase flow conditions.	39
Figure 17. Boundary conditions of the lab-scale SEVR CFD model.	39
Figure 18. Thermal Efficiency of the SEVR as a function of the inlet mass flowrate under single-phase conditions with comparison between previous and present experimental studies [75].	41
Figure 19. Flowchart of the numerical simulation framework.	42
Figure 20: Axial distribution of the wall temperature of the receiver for a series of.....	48
Figure 21: Measured values of gas outlet temperature as a function of suction level for various inlet mass flowrates.	49
Figure 22: Measured values of Thermal Efficiency for different suction level and inlet mass flowrate.	50
Figure 23: Measured values of Exergy Factor for different suction level and inlet mass flowrate.	50
Figure 24: Measured values of wall Temperature and normalised wall temperature as a function of (a, b) Froude number (c, d) particle volumetric loading (d, e) particle size.	53
Figure 25: Measured values of (a) outlet air temperature at a constant particle loading for different values of Froude number. (b) Normalised outlet air temperature at a constant particle loading for different values of Froude number.	55
Figure 26: Measured values of (a) Outlet air temperature at a constant particle size for different values of Froude number. (b) Normalised outlet air temperature at a constant particle size for different values of Froude number.	56
Figure 27. Measured values of (a) Outlet air temperature at a constant Froude number for different values of particle loading. (b) Normalised outlet air temperature at a constant Froude number for different values of particle loading.	58
Figure 28. Measured thermal efficiency within the SEVR as a function of (a) Stokes number with different Froude number at a constant particle loading (b) particle loading with different Froude number at a constant particle size (c) Stokes number with different particle loading at a constant Froude number. Measured exergy factor within the SEVR as a function of (d) Stokes number with different Froude number at a constant particle loading (e) Stokes number with different particle loading at a constant Froude number (f) particle loading with different Froude number at a constant particle size.	62
Figure 29. (a) Measured radiative heat loss through the aperture for different Froude number at a given particle loading and size. (b) Measured convective heat loss through the aperture for different Froude number at a given particle loading and size.	65



Figure 30. (a) Measured fractional radiative heat loss through the aperture different particle loading at a given particle loading and particle size. (b) Measured fractional convective heat loss through the aperture different particle loading at a given Froude number and particle size.....	66
Figure 31. Calculated values from experimental and numerical study of the enthalpy ratio as a function of Stokes number with various (a) Froude number for a fixed particle loading. (b) Particle loading for a fixed Froude number. ....	68
Figure 32. Calculated values from experimental and numerical study of the enthalpy ratio normalised by gas/particle mass loading ratio as a function of Stokes number with various (a) Froude number for a fixed particle loading. (b) Particle loading for a fixed Froude number. ....	69
Figure 33. Calculated percentage difference between air and particle temperature on (a) Stokes number as a function of Froude number with constant particle loading. (b) Stokes number as a function of Particle loading with constant Froude number. (c) particle loading as a function of Froude number with constant particle size.	72
Figure 34. Simulated thermal efficiency within the SEVR as a function of Stokes number with (a) different Froude numbers at a constant particle loading (b) different particle loadings at a constant Froude number. (i.e, calculated with Equations 3.12 – 3.14) .....	74
Figure 35: Calculated air and Particle Temperature along with particle concentration within the SEVR under a fixed particle size of 155 $\mu$ m and particle loading, under the (a) Froude-Stokes and (b) cyclonic regime. ....	76
Figure 36. Representative maps estimated for the particle volume concentration across different radial and axial planes within the SEVR under the Froude-Stokes regime ( $Fr < 4$ ) with a constant particle size.....	77
Figure 37. Representative maps estimated for the particle volume concentration across different radial and axial planes within the SEVR under the cyclonic regime ( $Fr > 4$ ) with a constant particle size.....	78
Figure 38. Representative maps estimated for the temperature distributions across different radial and axial planes within the SEVR under the (a) Froude-Stokes regime ( $Fr < 4$ ) and, (b) cyclonic regime ( $Fr > 4$ ) with a constant particle size. ....	79
Figure 39. Simulated values of swirl number at positions ( $z/L = 0.18, 0.42, 0.89$ ) (a) particle loading with constant Froude number and particle size, (b) Stokes number (particle size) with constant particle loading and Froude number. ....	81
Figure 40. Simulated dimensionless particle residence time as a function of Stokes number within the SEVR as a function of (a) Froude number under a constant particle loading. (b) particle loading under a constant Froude number.....	83

## List of Tables

<i>Table 1: (a) Geometrical and (b) Thermal properties of the SEVR, insulation and particles. ....</i>	<i>31</i>
<i>Table 2. A summary of the experimental and numerical operational conditions chosen for this study.....</i>	<i>35</i>
<i>Table 3. A summary of operational conditions for the study on the effects of overventilation by suction.....</i>	<i>36</i>
<i>Table 4: Details of the validation process undertaken, and level of agreement obtained. The latter is reported as the difference between the experimental data and the numerical model regarding the agreement level of outlet and wall temperature.....</i>	<i>40</i>
<i>Table 5: The operational details of the Froude-Stokes and cyclonic regimes of operation, generated with four inlet tangential velocities and values of the key-dimensionless parameters based on CFD results. ....</i>	<i>45</i>

## List of Publications

The works included in this thesis are performed by the author and have been submitted for journal publications.

Main Authored:

**Ang D**, Chinnici A, Tian ZF, Saw WL, Nathan GJ. Influence of particle loading, Froude, and Stokes number on the global thermal performance of a vortex-based solar particle receiver. *Renewable Energy*; *Accepted for publication, 10<sup>th</sup> Nov 2021*.

Co-authored:

Chinnici A, Davis D, Lau TC, **Ang D**<sup>1</sup>, Troiano M, Saw WL, Tian ZF, Solimene R, Salatino P, Nathan GJ. Measured global thermal performance of a directly irradiated suspension-flow solar particle receiver with an open aperture. *Solar Energy*; *Accepted for publication, 7<sup>th</sup> Nov 2021*.

---

<sup>1</sup> Contributed to the experimental study on the utilization of aerodynamic control strategy under the single-phase flow conditions in both idea and lab-work.

## Nomenclature

$L$	Receiver Length [mm]
$D_c$	Receiver Diameter [mm]
$\theta$	Cone angle [°]
$d_{ap}$	Aperture diameter [mm]
$r_{ap}$	Aperture radius [mm]
$d_{in}$	Inlet jet diameter [mm]
$d_{out}$	Outlet jet diameter [mm]
$P_{sp}$	Particle Sphericity
$L_{ins}$	Insulation thickness [mm]
$k$	Thermal conductivity [W/mK]
$c_{p,p}$	Particle specific heat capacity [kJ/kg K]
$c_{p,a}$	Air specific heat capacity [kJ/kg K]
$\varepsilon_p$	Emissivity of Particle
$\varepsilon_{eff}$	Emissivity of the reactor wall
$\dot{V}_{in}$	Inlet volumetric flow rate [SLPM]
$U_f, U_{in}$	Inlet air flow velocity [m/s]
$U_t$	Tangential velocity of air [m/s]
$\dot{V}_{out}$	Outlet volumetric flow rate [SLPM]
$U_{out}$	Outlet flow velocity [m/s]
$\dot{V}_p$	Particle volumetric flowrate [m <sup>3</sup> /s]
$\dot{V}_g$	Gas volumetric flowrate [m <sup>3</sup> /s]
$V_r$	Volume of reactor [m <sup>3</sup> ]
$d_p$	Mean particle diameter [ $\mu m$ ]
$\dot{m}_{a,i}$	Air mass flowrate at the inlet [g/s]
$\dot{m}_{a,o}$	Air mass flowrate at the outlet [g/s]
$\dot{m}_{p,i}$	Particle mass flowrate at the inlet [g/s]
$\dot{m}_{p,o}$	Particle mass flowrate at the outlet [g/s]
$Fr$	Froude number
$Sk_c$	Stokes number
$\phi$	Inlet particle volumetric loading

$T_w$	Wall temperature [K]
$T_{a,o}$	Outlet air temperature [K]
$T_{p,o}$	Outlet particle temperature [K]
$T_{a,o,tp}$	Outlet air temperature of the two-phases in CFD [K]
$\Delta T_{p-a,o}$	Temperature difference between particle and gas [K]
$T_a$	Air temperature within the receiver [K]
$T_p$	Particle temperature within the receiver [K]
$\dot{Q}_s$	Input Solar [kW]
$\alpha$	Net Air Ingress/Egress [%]
$\dot{Q}_{abs}$	Energy Absorbed [W]
$\dot{Q}_{cond}$	Conductive heat loss [W]
$\dot{Q}_{loss,ap,conv}$	Convective heat loss through aperture [W]
$\dot{Q}_{loss,ap,rad}$	Radiative heat loss through aperture [W]
$\mu_{sim}$	standard deviation
$F_{peak}$	Peak Flux [kW/m <sup>2</sup> ]
$P_{in}$	Total power of Simulator [kW]
$\bar{e}_{T_o}$	Outlet temperatures mean standard error [%]
$\bar{e}_{T_w}$	Wall temperatures mean standard error [%]
$\eta_{th}$	Thermal Efficiency [%]
$\eta_{th,air}$	Thermal Efficiency of gas-phase [%]
$\eta_{th,particle}$	Thermal Efficiency of particle-phase [%]
$\Delta H_{a-p}$	Enthalpy ratio
$\bar{\tau}_p$	Mean particle residence time [s]
$\tau_{nom}$	Nominal particle residence time [s]
$V_R$	Internal volume of the receiver [m <sup>3</sup> ]
$\kappa$	Normalised heat capacity terms
$S$	Swirl number
$\psi$	Particle volume concentration
$R_g$	Universal gas constant [J mol <sup>-1</sup> K <sup>-1</sup> ]
$MW$	Molecular Weight [g mol <sup>-1</sup> ]

## Abbreviations

CFD	Computational Fluid Dynamics
SVR	Solar Vortex Receiver
SEVR	Solar Expanding Vortex Receiver
CSR	Concentrated solar radiation
CST	Concentrated solar thermal

# Chapter 1: Introduction

Recent climate studies have shown that the increase in global average temperature is closely related to greenhouse gas emissions over a certain period [1]. Likewise, the transition to net-zero carbon emissions by 2050 poses a significant challenge for both the industrial and energy sectors. The production of high-value products is vital to the global economy, such as aluminium, steel and cement, are also energy-intensive, difficult to abate and responsible for some 15% of global CO<sub>2</sub> emissions [2-4]. Current statistics reveal that the amount of CO<sub>2</sub> needs to be reduced by 45% over the coming decade to achieve the common goal [5, 6]. Therefore, the present thesis aims to provide a new understanding of sustainable solar thermal technologies involving heavy industrial processes.

## 1.1 Concentrating Solar Thermal and Vortex-based Solar Particle Reactor

Solar energy is among the most abundant resources that could be extracted directly from the earth's surface, which presently equates to around  $2.6 \times 10^{24}$  J annually, showing greater availability than the total energy demand of  $5.67 \times 10^{20}$  J annually worldwide [7]. This benefit indicates that harnessing solar energy through concentrated solar thermal (CST) technologies are a viable option for industrial processes that require intense heat due to the edge of eliminating carbon footprint. Hence, such technologies are encouraged for further development to allow for its utilization under industrial scale in parallel meeting high efficacy and cost-effectiveness standards.

Concentrated solar thermal (CST) systems use a field with a combination of mirrors or lenses to concentrate solar radiation from the sun onto solar receivers, consisting of both beam-down or beam-up configurations, as shown in Figure 1 [8, 9]. The capability of CST in generating heat offers a tenable potential for utilisation in areas such as power generation, downstream process sensible heating, water heating and gasification [10, 11]. These systems can mainly be categorized into gas receivers, liquid receivers, and solid particle receivers. For applications in heavy industry, the technology with the most significant potential to achieve high temperatures of 800 – 1400 °C is the particle-based solar receivers [12]. This technology is receiving growing interest due to the stability of selected particles at those temperatures, their efficient absorption of radiant energy and the high specific heat capacity of particles [13, 14]. A wide range of particle receivers has been tested, such as the fluidised bed receiver, falling particle receiver, vortex-flow particle receiver and centrifugal receivers [15-18]. Of these, the vortex-flow solar receiver is particularly well suited to heating reacting particles through radiation since it heats

the particles in suspension within a gaseous flow [19]. Therefore, to demonstrate that vortex-based solar particle receiver is viable for sensible heating and thermochemical processes, further research into the key mechanisms affecting the thermal performance and heat transfer of this technology is required.

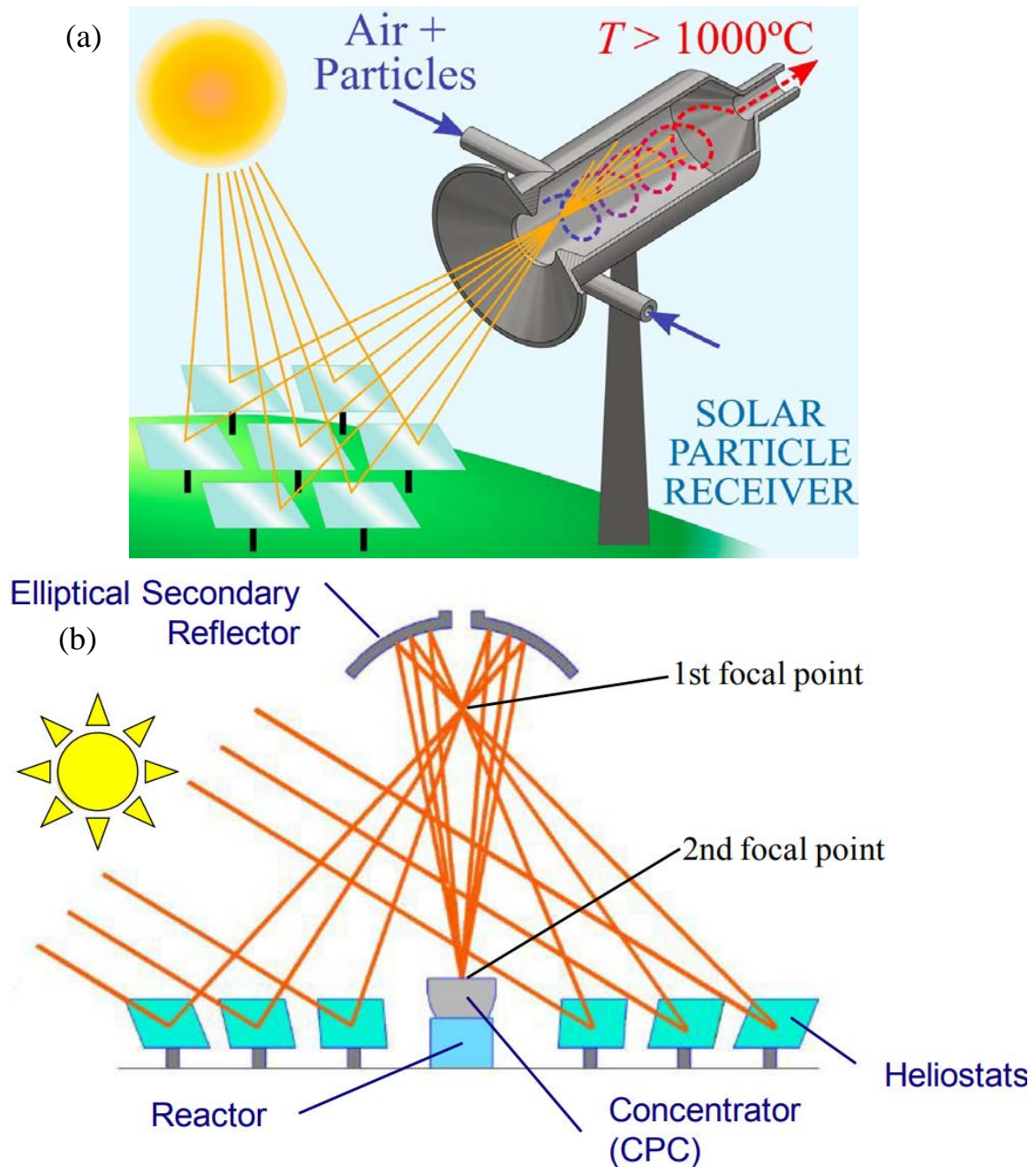


Figure 1. Principle of the (a) beam-up, (b) beam-down concentrated solar system configuration [8,9].



Some previous works of the vortex-based solar particle reactor technology include a testing scale conducted for the gasification process to convert raw feedstock material into syngas products such as hydrogen and aluminium bauxite [20, 21]. Preliminary research on the gasification of carbonaceous feedstock shows that the conversion efficiency of chemical energy has reached 87% [11]. Another study conducted by Davis et al. [21] reports that CST could be potentially applied for the calcination stage of alumina. This research has been proven feasible for the calcination of alumina, with results of chemical conversion efficiencies of up to 95.8% [21]. However, limited experimental and numerical datasets are presently available for their applications in sensible heating. Hence, the solar expanding vortex receiver (SEVR) was designed and partially tested to incorporate CST into the Bayer process. The application of this device is not limited to mineral processing but can be utilized for sensible heating of downstream processes.

## **1.2 The Solar Expanding Vortex Receiver (SEVR)**

In conventional vortex-based solar receivers, the propensity and deposition of hot particles on the window pose a risk for unnecessary maintenance cost and window failure during operation due to the strong vortex structure generated by the flow [22]. To resolve these concerns, the SEVR, shown in Figure 2, has been proposed and patented by the Centre for Energy Technology (CET), the University of Adelaide [23]. By altering the inlet and outlet positions, it reduces the vortex intensity relative to the momentum of the swirling flow at the inlet plane. Thus, this enables particles to propel away from the aperture and reduces particle deposition on the window. The working principle of SEVR is that injection of gas and particle flows from the tangential inlet(s) from the conical end, as concentrated solar radiation (CSR) from the aperture is used to heat the vortex flow. These particles are carried along by the vortex flow formed by the tangential inlet jets, and these particles are ejected through the radial outlet [22]. The heated particles or feedstock are then transported to various applications such as energy storage, alumina calcination, and syngas production. Detailed research of the SEVR conducted previously can be found in the literature review chapter.

For the current study, the windowless configuration will be examined across all studies to reduce potential particle deposition on the window and the high-cost maintenance in future scaled-up version of the reactor. The SEVR is the crucial component of the research in the project titled ‘RND054: integrating concentrated solar thermal into the Bayer process’ funded by the Australian Renewable Energy Agency that is potentially used for gibbsite calcination [24]. In addition, the understanding of the influence of different parameters on thermal

performance is essential for the integration of SEVR into the Bayer process. However, no previous work has been done to assess the thermal performance of the novel windowless configuration of the SEVR through both experimental and numerical methods. Therefore, this thesis aims to provide a new understanding on the thermal performance of the SEVR by varying key operational and operational parameters.

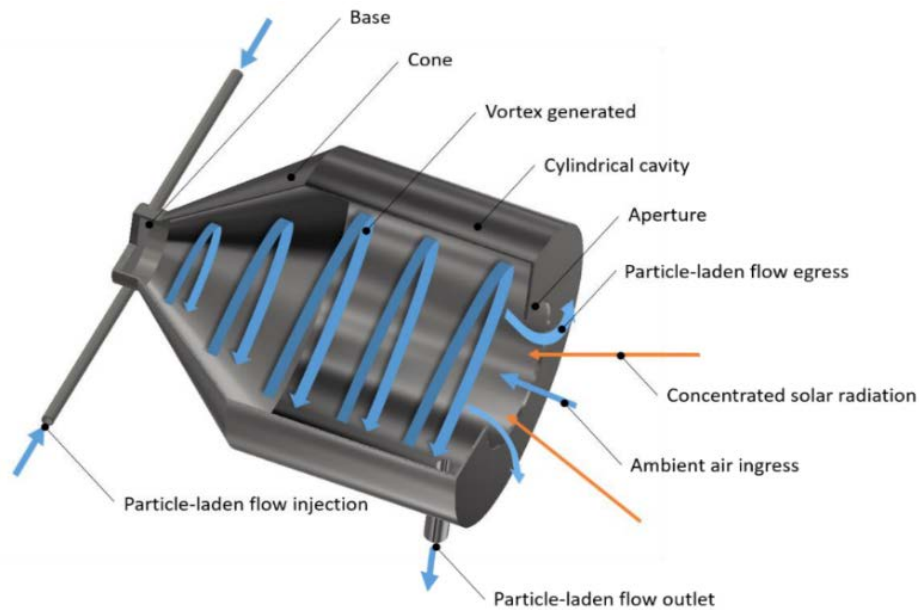


Figure 2. Schematic Diagram of the Solar Expanding Vortex Receiver (SEVR).

### 1.3 Thesis Structure

The present thesis consists of six chapters. The first chapter provides some background information concerning concentrated solar thermal and entrained flow vortex-based solar particle receiver. Chapter 2 of the thesis offers a systemic literature review highlighting several research gaps in the current SEVR regarding key operational and dimensionless parameters affecting the device's thermal performance. Based on these gaps, the aim and objectives of this project are formulated. Chapter 3 highlights the methodology applied both experimentally and numerically to address the goals attained from the literature. Chapter 4 presents the discussion of results undertaken from the experimental study, which mainly includes the influence of key operational parameters of suction level on the thermal performance under single-phase flow conditions. Meanwhile, the characterisation of key dimensionless parameters was also performed under two-phase flow conditions. Chapter 5 presents the results from the CFD study on the coupled effects of critical operational and dimensionless parameters on the device's

thermal performance. Chapter 6 summarises the understanding of key outcomes obtained from this study and provides an overview of the potential future work that needs to be done for the SEVR.

The thesis incorporates a combination of conventional and publication formats, following the guidelines of the University of Adelaide. The content of the journal articles was divided across Chapters 2 – 6, which has been accepted for publication. The manuscript of the journal article is included in the appendices of the thesis.

## Chapter 2 Literature Review

In this chapter, an overview of the successes and limitations of previously tested solar particle reactors will be discussed, followed by a review of vortex-based cavity receivers. Non-dimensional parameters will be included to better understand and quantify the reactor's thermal performance study for scaling up purposes. The background of heat transfer characteristics on particle-laden flows will also be covered, followed by a discussion of several thermal performance studies previously conducted under solar receivers. This is significant in identifying key objectives influencing the thermal performance of the solar expanding vortex receiver (SEVR).

### 2.1 Reactor Designs for Thermochemical Processes

Most particle-based solar receivers fall into two categories: direct and indirect particle heating receivers [12]. For direct particle receivers, the solar radiation is directly irradiated from the sun to the particles. In contrast, indirect particle receivers employ enclosures or tubes as a medium to transfer heat to particles. One of the advantages of a directly irradiated receiver includes reducing exergetic losses through a provisional heat exchanger. Furthermore, an advantage of the indirect particle receiver is its reduced maintenance and installation cost and prevention of particle egress (e.g. intermittent clouds) [25]. However, these requirements could not satisfy the level of process heat needed for heavy industrial processes. Hence, the current research mainly focuses on directly irradiated particle receivers.

Of several directly irradiated receiver designs for thermochemical processes, most fall within three categories: packed bed, fluidised bed, and vortex-flow configurations shown in Figure 3 [18, 26, 27]. For the packed bed receiver, raw products are stacked into the reactor through the vent, where concentrated solar radiation is focused on the feedstock at the window section [26]. Steam jets are located around the window interior to act as gasification agents for the feedstock. After the feedstock had been processed, the bed collapses to bring fresh feedstock from the pile to focus under CSR. However, one concern of this configuration is the potential of tar build-up on the window by gasified materials, which reduces process efficiency and causes permanent damage to the window [28]. The fluidised bed receiver shown in Figure 3b operates by projecting CSR through the column while feedstock is fed through tubes horizontally along with steam from the bottom of the reactor [27]. Small particles are required under this application (<150 microns) to allow for better radiative heat absorption and conversion efficiencies [11, 28]. Parameters such as the column size and purging gas and steam rate are

controlled to ensure that the feedstock is within the reaction zone. However, it is observed from some studies that the poor radiative and conductive heat transfer rate, coupled with high flow rates of required fluidizing gas contributes to uneven product conversion, which leads to a reduction of chemical conversion efficiency [29, 30].

Similar to fluidised bed receivers, previous studies show that the lab-scale testing for the vortex-based solar reactors must operate under small particle sizes (approximately  $< 250$  microns) to prevent particle deposition within the reactor. This is justified because the particles rely on the momentum generated by the vortex flow of the gas to transport the particles along the reactor, which is dependent on the particle properties (i.e., density, sphericity, and size). In addition, the reactor must be designed to account for sufficient particle residence time to synthesise the feedstock altogether [20, 31]. The high chemical conversion rate of the vortex-based receiver offers a high potential for it to operate as an industrial thermochemical reactor, which forms the basis aligning with the objectives of this project. Although previous research has demonstrated many features for thermochemical processes in the entrained flow reactors, sensible heating of non-reactive particles is currently unknown for this class of solar technology. Hence, this research utilizes a non-reactive process for sensible heating to increase understanding of the aspects with the coupled influence of key operational parameters such as inlet mass flowrate, particle loading and sizes on thermal performance within the SEVR.

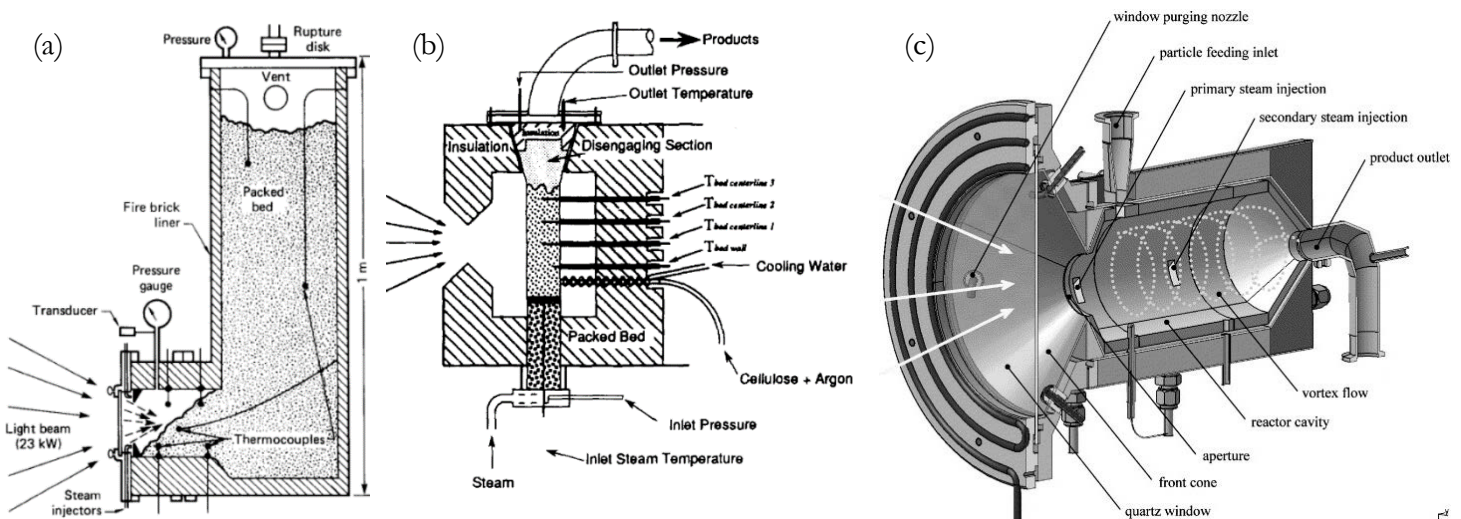


Figure 3. Some Examples of Solar Thermochemical Receivers: (a) packed bed [26] (b) Fluidised bed [27] (c) vortex-flow [11].

## **2.2 Vortex-based Solar Cavity Receivers**

### **2.2.1 Solar Vortex Receiver/Reactor (SVR)**

The SVR has been tested for the steam gasification of petroleum coke, coke-water slurry, and calcination of zinc and alumina by ETH Zurich [11, 18, 21, 32]. Components of the SVR consists of a quartz window, an aperture, a secondary concentrator (SC) and a cylindrical cavity. As shown in Figure 3c, steam and particles are injected tangentially into the SVR reactor to generate a vortex flow; particles flow along the reactor while absorbing the concentrated solar radiation from the aperture [33]. It was found that the chemical conversion efficiency of the SVR is up to 85%, which is more effective compared to most directly irradiated solar particle receivers [20, 29]. However, one of the challenges of the SVR is the propensity and deposition of particles on the reactor quartz window [33]. The tendency of particle deposition on the quartz window is mainly caused by the strong vortex structure generated by the flow, introducing potential risks for window failure due to overheating caused by deposited particles [18]. In addition, particle deposition on the window causes attenuation of solar radiation, reducing chemical conversion efficiency [33]. Likewise, the addition of a quartz window further increases the life cycle cost of the device in terms of cleaning and repair, which is deemed unfeasible in an extensive system. Hence, this prompts a motivation to propose an alternative configuration to address these issues.

### **2.2.2 Solar Expanding Vortex Receiver (SEVR)**

A novel back-flow configuration receiver known as the solar expanding vortex receiver (SEVR) is proposed to address the shortfall of the SVR, as shown in Figure 2. The working principle of the SEVR is similar to that of the SVR but with some important differences. One of the differences is that the tangential inlets of the SEVR are located at the opposite end of the conical, while the radial outlet is located at the cylindrical cavity close to the aperture. The symmetrical tangential conical inlets of the SEVR can generate a more stable vortex structure compared to a single asymmetric inlet used by the SVR, hence, reducing the swirl intensity of the vortex flow [33, 34]. By positioning the inlets at the opposite end of the reactor, the central recirculation zone drives the particles away from the aperture, thereby reducing the axial transport of particles through the vortex core [33, 35]. Experimental and numerical studies have been conducted under isothermal conditions to understand the aerodynamic mechanism of the vortex structure flow patterns, particle deposition and residence time within the SEVR [36]. It was hypothesised that, in the early development phase, selecting an aperture diameter smaller than the vortex core diameter and increasing the cone angle might inhibit the propensity of

particles through the aperture. According to the study conducted by [37], it was concluded that the critical parameters that affect the deposition of the particle on the window are the ratio of maximum vortex core,  $d_{v,max}$ , to the aperture diameter,  $d_{ap}$ , and the vortex intensity ( $S_{ap}$ ) at the aperture plane. Note that the vortex intensity refers to the swirl number at the aperture region. As a result, the design with a lower  $d_{v,max}/d_{ap}$  ratio and vortex intensity contribute to reduced particle propensity through the aperture plane. It was also reported that the vortex core size depends on the cavity length and the cone angle [37].

### **2.2.3 A Windowless SEVR**

Previous studies of the vortex based solar receivers were conducted in an enclosed cavity with a clear window fastened on the aperture plane. The window causes a reduction in reactor efficiency due to scattering and attenuation of solar radiation, window particle deposition, and an increment in operational cost for industrial application. Thus, a solution is applied by applying a windowless approach for the aperture of the SEVR. One of the key concerns regarding the windowless configuration is that the particle-laden flow within the SEVR tends to escape through the aperture to the open atmosphere due to particle propensity caused by the precessing vortex core (PVC) within the chamber [36, 37]. To mitigate particles egressing through the aperture, overventilation by suction has been proposed at the radial outlet to allow air ingress from the aperture, potentially reducing particles from egressing through the aperture. However, limited knowledge is currently available on the effects of a windowless aperture on the thermal performance of the device. Thus, there is a need to identify the key dimensionless and operational parameters affecting the thermal performance of the receiver under the windowless condition.

A previous study on the isothermal flow-field of the windowless SEVR shows that an increase in the outlet-to-inlet air flowrate ratio leads to a reduction of flow escaping through the aperture; however, this introduces more air ingressing into the device, as shown in Figure 4 [37]. In addition, implementing such a process changes the flow structure of the central recirculation zone. The peak tangential velocity within the SEVR is reduced by almost 60% compared to that in the closed aperture configuration. This indicates that an increment of outlet flow rate leads to a reduction in vortex strength within the cavity, further reducing the flow transported toward the aperture under the tangential motion. Although the introduction of suction is beneficial for a windowless device, it is essential to note that the mean axial velocity within the device is significantly reduced under sealed conditions, as there is no entrainment of air

from the aperture. The result shows that the mean axial velocity in the SEVR was increased by 70% compared to that on a closed-aperture when reducing the outlet-to-inlet mass flowrate ratio to a value of 1.1. This indicates that the outlet flow rate dominates the flow transportation from the aperture to the conical frustum under windowless operation [37]. The further increment of the inlet-to-outlet flowrate ratio changes the axial velocity profile at the outlet port; this shows that the location of the outlet port plays a significant role in the flow-field of the vortex-based device. As of current, limited data is available on the coupling influence of particle trajectory and flow structures on the thermal performance within the SEVR. Therefore, several significant operational and dimensionless parameters such as the particle loading, Froude number, and Swirl number needs to be evaluated to characterise the thermal performance of the vortex-based solar particle receiver.

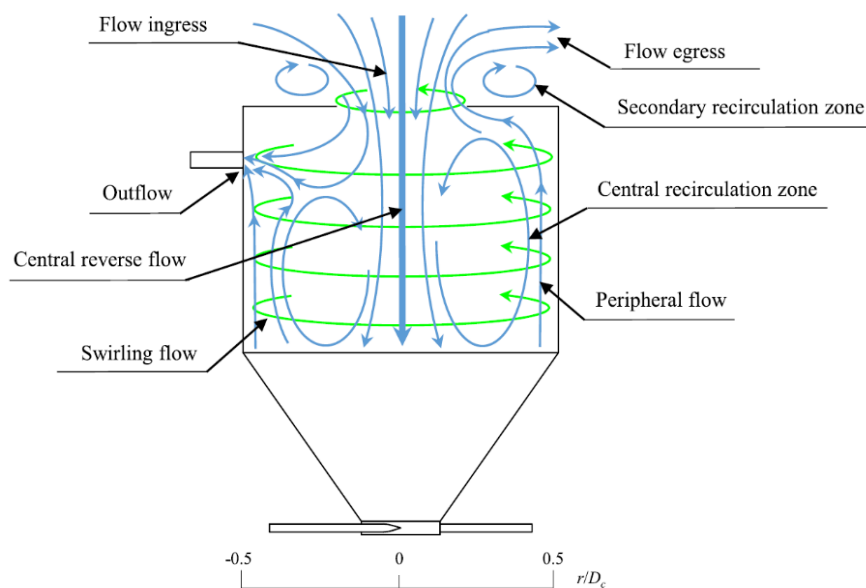


Figure 4. Simplified schematic diagram of key flow features identified for the windowless SEVR [37].



## 2.3 Dimensionless Parameters

Dimensionless parameters play a critical role in reducing the number of manipulative variables within a system by reducing the amount of experimental data required to correlate with the physical phenomenon occurring within a scalable system. The present thesis allows for a better understanding of the fluid dynamics and heat and mass transfer processes of a potentially scaled-up SEVR device through the experimental and numerical data obtained from the small-scale prototype reactor. This aims to ensure that a comparable trend is attained for the operation of the system, where dimensions and parameters defined for flow-field and heat transfer may behave differently under different scales. Therefore, suitable dimensionless parameters should be identified and utilised in both experimental and numerical studies to allow adequate characterisation of the thermal performance within the device.

The thermal performance of the device can be characterised through several dimensionless parameters. Of such, the key dimensionless parameters of the SEVR system could be distinguished by Reynolds number, Froude number, Stokes number and swirl number. As observed, it is believed that Reynolds number has lesser influence compared to their other counterparts. This is because the vortex flow within the cyclonic chamber is conducted under the fully turbulent regime. Although this does not significantly influence the flow field and heat transfer within the SEVR, a minimum velocity of 20 m/s is required to maintain the particle phase flow. The gas velocity should not be above 45 m/s to prevent the high-pressure drop in the vortex flow. Meanwhile, the Froude number is seen to have a significant influence when coupled with the particle residence time of the reactor since two prominent regimes were reported from previous studies; however, little is known of this parameter when correlated with the thermal performance of the SEVR. Hence, more research is required to understand the coupling effects of these parameters on the heat transfer processes.

### 2.3.1 Reynolds Number

To begin with, the Reynolds number,  $Re$ , is defined as the ratio of inertia effect to the viscous force within a fluid, which is used to indicate whether the fluid flow lies in the laminar or turbulent regime.

$$Re = \frac{\rho_f U_f D_f}{\mu_f}, \quad (2.1)$$

where  $\rho_f$  is the density of the fluid,  $U_f$  being the velocity of the fluid,  $D_f$  is the characteristic length of the inlet pipe diameter, and  $\mu_f$  is the dynamic viscosity of the fluid. It is observed

that most fluid flows in large-scale cyclonic devices operate under a turbulent regime with a high Reynolds number as turbulent mixing occurs within the cyclonic chamber. Similarly, thermochemical processes such as calcination are carried out under fully turbulent flow regimes to ensure that calciner products are uniformly mixed [38]. Therefore, all current experimental and numerical studies should implement the inlet Reynolds number within the fully turbulent regime to ensure the results correlate closely with a scaled-up device.

### 2.3.2 Froude Number

The Froude number is the ratio between the inertial effect and gravitational force within a hydrodynamic system. This formula (Equation 2.2) is assumed to be similar to a cyclone separator, which aims to centrifuge particles along the walls [39]. Since the SEVR possesses a similar trait to a cyclone separator, the utilisation of tangential velocity as the critical factor acting on the fluid can be accounted as the ratio of the inertial effect of the vortical flow to that of the external gravitational field.

$$Fr = \frac{U_t^2}{gD_c}, \quad (2.2)$$

where  $U_t$  is the tangential velocity of the gas phase,  $g$  is the gravitational acceleration and  $D_c$  is the characteristic length scale (i.e., the cylindrical diameter of the SEVR). The previous study conducted on the SEVR shows that two operational regimes were discovered, namely the Froude-stokes regime ( $Fr < 4$ ) and the cyclonic regime ( $Fr > 4$ ) [40]. In the first regime, particles are most likely to recirculate through the central recirculation zone. Particles tend to distribute near the receiver wall in the second regime, away from the recirculation zone [40]. The employment of the threshold value is to verify whether the flow field is inertially dominated or dominated by the gravitational field. Although the coupling influence on particle residence time and the tilt angle is known [41], the effects of the parameter on thermal performance are yet to be understood. Therefore, there is a need to investigate the coupled influence of this parameter on the device's thermal performance.

### 2.3.3 Stokes Number

Another critical parameter that needs to be defined is the Stokes number, which can be defined as the ratio of the particle response time to the characteristic time of the fluid. Particle response time ( $\tau_p$ ) refers to the time required by a particle to react to changes of the fluid velocity, while the characteristic time of the fluid ( $\tau_f$ ) is the time required for changes to occur within the fluid flow.

$$\begin{aligned} Sk &= \frac{\tau_p}{\tau_f}, \\ \tau_p &= \frac{\rho_p d_p}{18\mu_f}, \\ \tau_f &= \frac{V_f}{D_f}, \\ Sk &= \frac{\rho_p U_f d_p^2}{18\mu_f D_f}, \end{aligned} \quad (2.3)$$

where  $\rho_p$  is the density of the particle,  $U_f$ , the characteristic velocity of the fluid phase (i.e., the tangential velocity at the cylindrical diameter of the SEVR),  $d_p$ , particle diameter,  $\mu_f$  is the fluid dynamic viscosity, and  $D_f$  being the length scale of the fluid. From the definition, when  $Sk \ll 1$ , particle responds immediately to changes within the fluid flow velocity and hence follows the fluid; If  $Sk \cong 1$ , the particle partially follows the streamline of the flow, whereas, when the particle has  $Sk \gg 1$ , it becomes unresponsive to the fluid flow as it is more inertially dominated [42]. The behaviours of the particles with different Stokes numbers are presented in Figure 5. The current study is crucial in understanding how the particle responds to the fluid flow within the receiver. According to the study conducted [33], the design of the radial outlet allows for large particles ( $Sk \gg 1$ ) to be retained within the reactor as particles are more inertially dominated. This allows for a longer residence time within the reactor, which is hypothetically beneficial for heating large particles. Although the majority of findings demonstrate that the flow tends to be unresponsive when  $Sk \gg 1$ , it is observed that as Reynolds number increases, the trajectory of the particle tends to be slightly more responsive to the fluid flow [43]. This implies that the range of study investigated can have Stokes number between  $0 < Sk < 10$ . Although previous work has shown that the Stokes number has a significant effect on particle residence time, more work is required to be conducted to understand the coupling effects of Stokes number on the thermal performance of the SEVR.

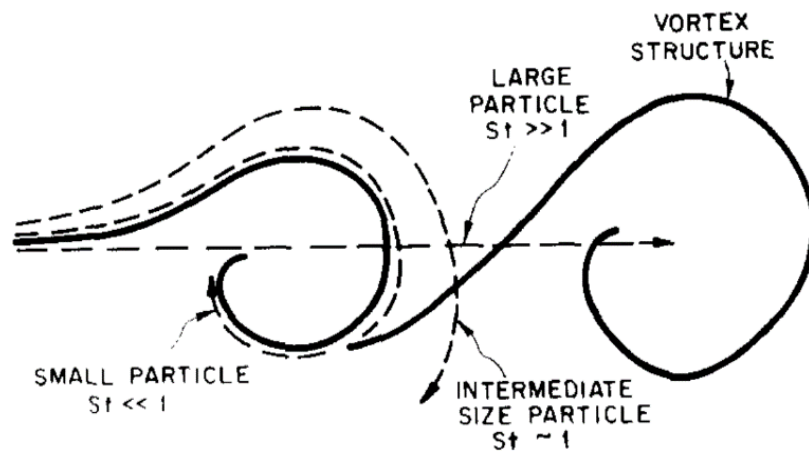


Figure 5. Pictorial demonstration on the effect of Stokes number in turbulent flows [42].

### 2.3.4 Particle Loading Ratio

Different regimes of particle-turbulence interaction were defined by Elghobashi (1994) based on the magnitude of particle volume fraction or better known as the volumetric particle loading, which is the ratio between particle and gas volumetric flowrate.

$$\phi = \frac{\dot{V}_p}{\dot{V}_f}, \quad (2.4)$$

where  $\dot{V}_p$  is the volumetric flowrate of particles and  $\dot{V}_f$  is the volumetric flowrate of the gas phase. The threshold value of the ratio indicates that when the particle has  $\phi$  less than  $10^{-6}$  the particle-phase effect on fluid flowfield is negligible; hence, this is referred to as one-way coupling. The second regime is the two-way coupling, which occurs when particles and fluid interact under the particle loading ratio of  $10^{-6} < \phi < 10^{-3}$ , implying effects of the particle on the fluid flowfield, which turbulence needs to be accounted for [44]. However, particle-to-particle collision is negligible as it does not significantly affect the flow trajectory. The particle-to-particle collision is prominent in the third regime, that is when  $\phi > 10^{-3}$ , indicating that the flows are of dense suspensions, which involves both particle-to-fluid and particle-to-particle interactions. This causes significant effects on particle and gas flows, referred to as the four-way coupling regime. For the current SEVR study, the coupling effects of particle loading on the reactor thermal performance is yet to be known. Hence, this is an essential critical operational parameter to consider. The detailed regime of the particle volume fraction is shown in Figure 6.

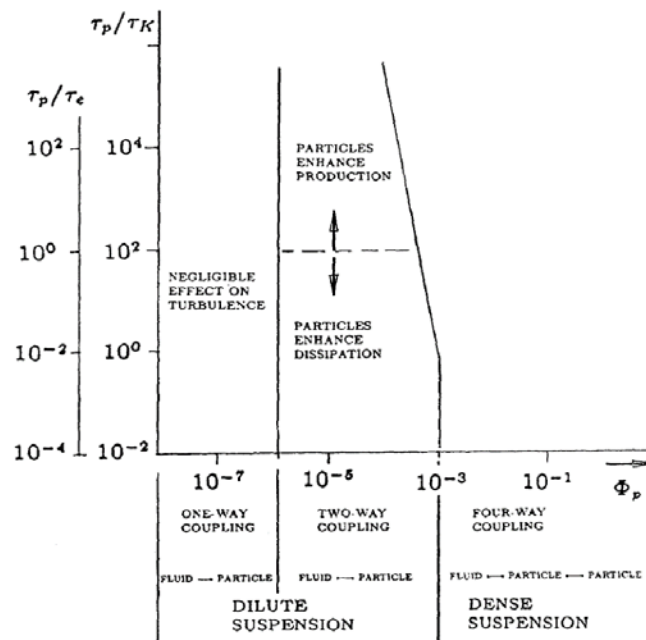


Figure 6. Regimes of interaction between particles and fluid phase, here  $\tau_e$  is the turnover time of large eddy, while  $\tau_k$  is the Kolmogorov timescale [44].

### 2.3.5 Swirl Number

The swirl number is defined as the ratio of tangential momentum flux to the axial momentum flux in a flow, which is mainly used to characterise the vortex intensity of a swirling flow,

$$S = \frac{\int_0^R \rho_f u_t u_{ax} r^2 dr}{R \int_0^R \rho_f u_t^2 r dr}, \quad (2.5)$$

where  $u_t$  and  $u_{ax}$  are the tangential and axial velocity components, respectively,  $R$  is the radius of the cylinder of the SEVR in this study. According to the study [45], the swirl number can be varied for  $S = 0 - 0.6$  (from no swirl to medium swirl) and intense swirling flows ( $S > 0.6$ ). To allow recirculation to occur within the flow, a swirl number greater than 0.6 is required [46]. Previously, the swirl number showed a significant impact on the propensity of particles on the aperture [46]. Thus, this implies that particle egressing has a direct correlation with the swirl intensity. Although swirl number has been evaluated under closed aperture conditions [22], it is necessary to determine the effect of swirl number on the flow field and thermal performance of the windowless SEVR.

### 2.4 Particle Residence Time Distribution

Chemical reactors are initially modelled as ideal reactors during the development phase. However, the flows and reactions in a thermochemical reactor usually are far from perfect in the real world. Therefore, the need to analyse and diagnose the behaviour of non-ideal reactors is critical. One of the key metrics is the particle residence time distribution (RTD), which is employed to characterise the performance within a chemical and mixing reactor [47]. The definition of RTD here could be explained as the probability distribution of time spent by a particle within a reactor under a given set of operational conditions [47]. The application of the RTD metric identifies the reactor's problem during operating state and predicts the conversion efficacy for a specific reaction within the system [48]. In particular, the RTD information is critical for recirculating flows dominated by strong turbulence and swirling characteristics due to their arbitrary nature, as seen in cyclones and vortex-flow devices [49]. In addition, the behaviour of particles tested is said to possess a different trajectory to the transporting gas, especially for test cases with Stokes number greater than unity. Although experimental studies have been conducted to identify critical parameters affecting the RTD in a lab-scale SEVR [40, 41], limited validated numerical data on RTD is presently available. Thus, there is a need to develop a numerical model to obtain data that validates well with the overall trend from the measured data to predict residence time distribution within a scaled-up device.

### 2.4.1 Particle Residence Time in Vortex-based Reactors

Previous research on RTD of vortex-based solar receivers is based on evaluating the reactor nominal residence time, which is defined as the ratio of the internal volume of the reactor on the inlet volumetric of the gas phase [48]. The nominal residence time can also be explained as the time taken for a pocket of injected air to exit the reactor.

$$\tau_{nom} = \frac{V_r}{\dot{V}_g}, \quad (2.6)$$

where  $V_r$  denotes the internal receiver volume ( $m^3$ ) and  $\dot{V}_g$  denotes the inlet volumetric flowrate ( $m^3/s$ ). The value of residence time is influenced primarily by gas density at the inlet for a given temperature and chemical reactions occurring within the flow. Without experimental and numerical data, most of the residence time is obtained from the basis of this formulation. However, such assumptions cannot be reasonably qualified as the residence time in the particle and gas phases differs significantly. They are dependent on a series of key operational parameters such as flux input, volumetric flowrate, reaction kinetics and flow-field characteristics. The earliest particle residence time study on the solar vortex reactor was conducted in [50], which shows that the average residence time between the two phases exceeds the nominal value. Therefore, there is a need to account for the actual particle residence time through the function of RTD. The distribution span of residence time is also an important data to consider as it is dependent on parameters such as inlet flowrate, particle polydispersity and Stokes number. In addition, different thresholds have been used to characterise the particle RTD, such as the time required for a given fraction of particles (e.g., 50%, 90% at the outlet to the inlet) to exit the vessel [41]. Although a previous study on RTD has been conducted experimentally and numerically within the SEVR under isothermal conditions [40, 41], there is still a limited amount of data of the SEVR operating under high-temperature conditions. Therefore, a new understanding of RTD must be established to observe the coupled influence between key operational parameters under a high-temperature environment.

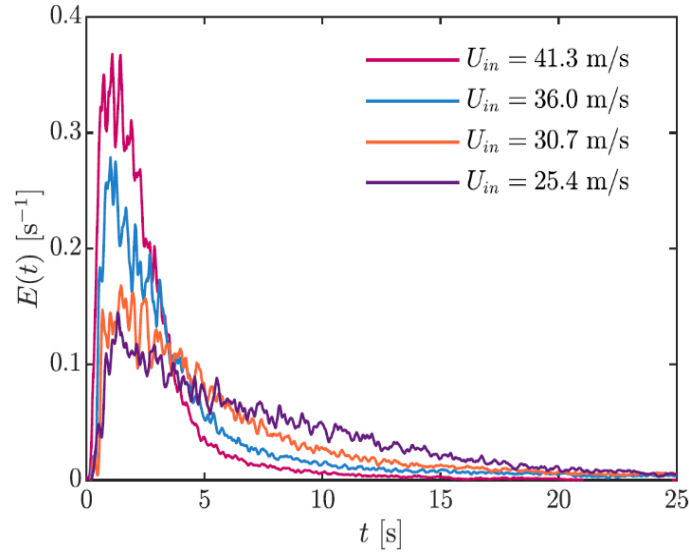


Figure 7. An example of measured RTD of the SEVR under isothermal conditions at a constant particle size of  $80\mu\text{m}$  with variation of inlet flow velocities [40].

## 2.4.2 RTD study within the SEVR

From previous numerical RTD results, the SEVR has successfully generated a greater RTD when particle size increases, which have a Stokes number greater than unity, being beneficial since large particles need more heating and reaction time than small particles [40]. This is due to the more significant inertial effect created by the flow when the outlet is positioned in a radial direction, inhibiting the escape of larger particles within the cavity. However, the experimental data is limited to assess the effects of heat transfer on the RTD of the device. Thus, there is a need to develop a model that accounts for RTD behaviour under a given thermal input.

Recently, an isothermal study on particle residence time distribution within the SEVR has been performed in [40] through a joint series of experimental, numerical, and theoretical methods. For the experiment, the pulse response method was employed. A short pulse of particles known as tracers is injected to measure the concentration of the particles at the inlet and outlet of the SEVR with time-resolved laser extinction measurements [49]. It is also worth noting that the orientation of the receiver in this study is of beam-down configuration. The working principle involves using a pulse response method monitored by a set of collimated laser diodes located at the inlet and outlet; the laser beam records the attenuation injected from the diode through a photodetector. The concentration of particles and time at the outlet were recorded instantaneously. The key findings from this analysis reported that two regimes were found, namely, the Froude-Stokes regime (low Froude number,  $Fr < 4$ ) and the cyclonic regime (high Froude number,  $Fr > 4$ ). Here, it determines whether the flow within the cavity is gravity



( $Fr < 4$ ) or inertially dominated ( $Fr > 4$ ). The Stokes number at the outlet has the most significant effect on the particle residence time in the Froude-stokes regime because of the greater inertia at the radially oriented outlet, making it likely to recirculate within the receiver. It also demonstrates that particles may return to the receiver's base as the flow is being gravitationally dominated. Meanwhile, the Stokes number is less significant under the cyclonic regime because the centrifugal inertia forces act independently of the tangential velocity, which keeps them from the central reversed flow zone resulting in shorter residence time. The two distinctive regimes are shown in Figure 8. Although the RTD data has been obtained under the isothermal state, there is still a need to understand how these regimes would affect the thermal performance within the device. Hence, there is a need to develop a numerical model to gain a fundamental understanding of the coupling influence of reactor flow-field and heat transfer within the device.

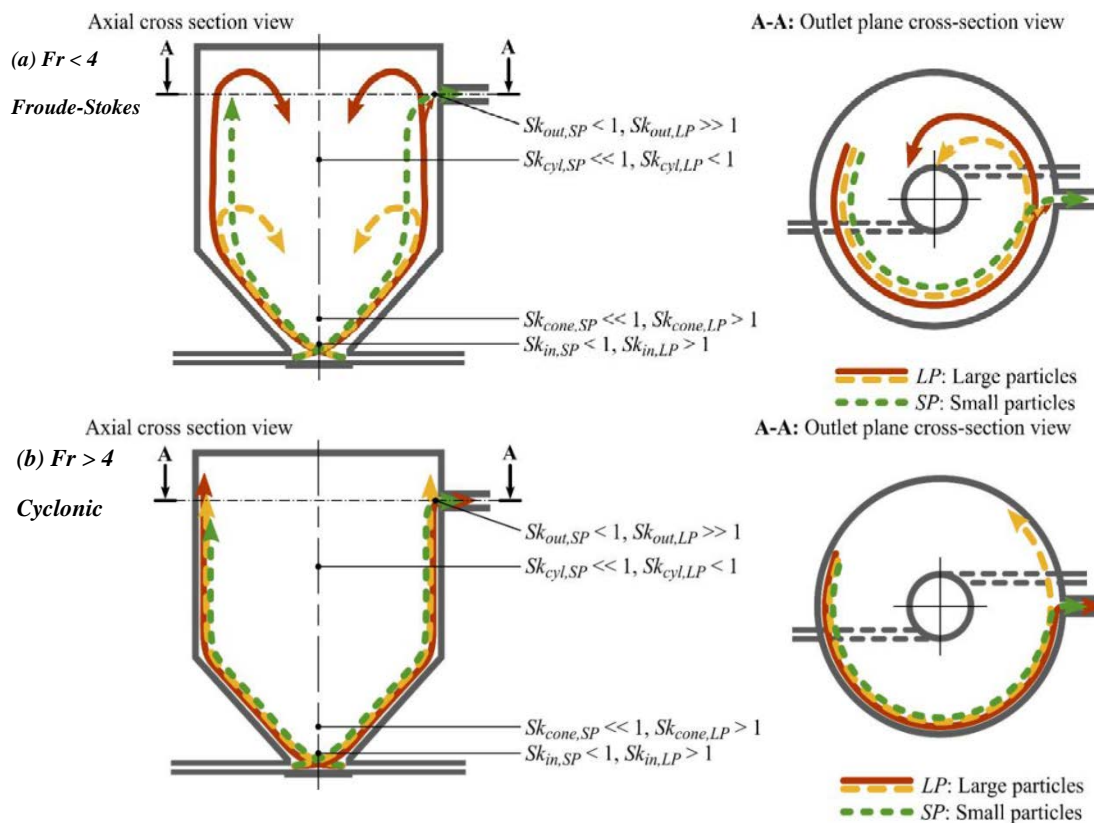


Figure 8. Demonstration of SEVR behaviour derived from experimental and numerical analyses of the three-dimensional flow-field within the SEVR in both (a) Froude-Stokes and (b) cyclonic regimes [40].

### **2.4.3 Influence of Receiver Orientation on RTD within the SEVR**

Another study has been conducted to observe the influence of receiver tilt angle on particle RTD [41]. Gravity was found to have a significant impact on RTD for large particles ( $Sk > 1$ ) while negligible for small particles ( $Sk \leq 1$ ). The result found that the receiver's horizontal orientation has less significant effects on RTD for both Froude-Stokes and cyclonic regimes. This is because the inertial effect rather than gravity dominates the particle behaviour within the receiver [41]. With an agreement that particle RTD is dependent on the particle size under the Froude-stokes regime, it could be hypothesised that different stokes numbers could affect the thermal performance within the SEVR. Although the previous one-dimensional numerical study has been performed [9] to assess the thermal performance of both the SVR and the SEVR, the assumption that particles are evenly distributed within the receiver is unrealistic. Temperature fluctuations in the vortex flow are expected, affecting the reactor's thermal efficiency. Nevertheless, the influence of the Stokes number on thermal performance within the SEVR is not understood.

## **2.5 Thermal Performance of Solar Receivers**

Thermal performance analyses are crucial in determining the heat transfer within a solar receiver to assess the system's heat losses and efficiencies [51]. In previous studies, hot test analysis had been performed across various types of solar receivers to define the key controlling operational parameters affecting the thermal performance of the receiver [52].

### **2.5.1 Thermal Performance of Cavity Receivers**

Cavity receivers are usually preferred for solar thermal applications due to their large surface areas and lower thermal losses than external receivers [53]. Many research studies on cavity receivers are mainly focused on heat loss mechanisms affecting the overall thermal performance of the system [54]. These are dependent on various key operational and geometric parameters, such as solar flux inputs, aperture ratios, receiver lengths, inlet mass flow rates and outlet suction. Heat transfer analysis was previously conducted on cylindrical cavity receivers to assess the effects of geometric parameters on the thermal performance of the systems [55]. It was found that increasing the aperture diameter can reduce the thermal efficiency due to increased radiation losses, while increasing the diameter of the inner cavity induces an increase in convective heat losses. In contrast, the rise in heat losses is complementary to the increase of cavity length [55]. Furthermore, the study conducted [56] shows that increasing the inlet mass flow rate further increases the thermal efficiency of the receiver. To this end, a thermal

performance experiment has not been conducted on the existing SEVR test rig. Thus, there is a need to understand key operational parameters, such as air ingress, inlet flowrate, and suction flowrate and heat loss mechanisms on the thermal performance within the SEVR.

### **2.5.2 Thermal Performance Study in Vortex-based Receivers**

Thermal performance analysis for sensible heating on vortex based receivers through analytical modelling has been conducted in [9]. The study was conducted using the one-dimensional analytical model developed based on the zonal method [57, 58], which considers heat and mass transport within the enclosure. The thermal performance study focuses on particle mass loading, flow direction, particle size and receiver length on the global performance [9]. The Gauss-Siedel method adapted from [59] was applied for this sensitivity study using MATLAB software. From this technique, shape factors, radiosity and energy balance are calculated iteratively. The method operates by using the known dimension of SVR and discretizing it into many volume and surface zones. However, the technique assumes gas and particles are uniformly distributed, which is oversimplified under actual working environments.

From the analytical model in [9], the maximum change in thermal efficiency can be seen from the values of mass loading and flow entry direction. The inlet mass loading ( $\dot{m}_p/\dot{m}_{air}$ ) is defined as the mass flow rate of particles in the air to the mass flow rate of air entering through the inlet tubes. It is found that when mass loading is greater than the critical value of 1, the device acts as a particle heater. While mass loading is less than 1, the device acts as an air heater [21]. An air heater refers to mainly heating the air in the receiver, while a particle heater allows more heat to be carried away by the particle phase. To achieve optimal efficiency during operation, enthalpy recovery from both air and particle streams is necessary. It is showed that a maximum mass loading of 5.657 within the SEVR configuration could achieve a thermal efficiency of 88%. This is clarified as flow direction on the back entry allows for a greater particle exit temperature caused by greater heating of particle phase in the front sections of the receiver. The reduction of conductive heat loss results in re-radiation occurring in the internal surface rather than the aperture compared to the front entry configuration [9]. Although the analytical models of the SVR and SEVR have been developed, there is a need to validate and optimise these models using thermal performance measurements. Moreover, the inclusion of a steady-state experimental study is required to provide a validation dataset for future techno-economic assessment models and the scaling-up processes.

## 2.6 Heat Transfer in Particle-laden Flows

In most cases, solar particle receivers utilize air as a carrier fluid due to its high transparency to radiation, where most of the incident radiative flux is entirely absorbed by particles [60]. In this process, particles transfer the absorbed heat via conduction and convection to the surrounding carrier gas while convective heat loss occurs through the rest of the stagnant gas [61]. Based on the understanding of the flow characteristics, it is said that the flow pattern in the solar receiver has a significant effect on heat transfer. Another important phenomenon of heat transfer in particle-laden flows is the preferential concentration of particles within the flow [62]. The phenomenon usually occurs within the turbulent regime of the fluid and can be defined under high Reynolds number ( $Re > 4000$ ), where the accumulation of inertial particles are not able to comply with rapid velocity fluctuations leading to a high local concentration under zones of high strain resulting in the interaction between the particle and flow vortices [63].

Various studies conducted have confirmed that preferential concentration has compelling effects on the heat transfer within the flow. The key controlling dimensionless parameter that dominates preferential concentration is the particle Stokes number ( $Sk$ ). It has been characterised that the highest preferential concentration occurs as Stokes number closes to unity, and solid spatial clusters are formed within the flow region, which results in strong fluctuations of heat transfer to the gas phase [64]. Moreover, clustering of particles also influences the radiation absorption by particles through shadowing effects which indirectly affects the radiative heat transfer [65]. Another study by [66] shows that turbophoresis affects the heat transfer within the particle-laden flow, which is defined as the particle's tendency to migrate in the direction with reduced turbulence intensities. The effect of turbophoresis causes particle density near the walls to be higher than the centreline region, resulting in non-uniform absorption of incoming radiation through the aperture [66]. This forms a hypothesis that different flow regimes within the SEVR could contribute to other effects in heat transfer of particles (i.e. Froude-Stokes and cyclonic flow regimes, narrow and wide particle spread, suction effect on the flow structure of the particle-laden flow).

In addition, a recent study [67] shows that particle size distribution can significantly affect the preferential concentration within the one-direction turbulent flows. From previous modelling results, polydispersed particles performed better in transferring heat to the gas phase than narrow range monodisperse particles. This is because the widespread of a greater range of sizes in the polydispersed regime occupies a greater region in the flow, thus, providing a more

uniform distribution of temperature for the gas phase [67]. Uniformity of particles in the polydispersed system can be explained as the interaction of different particle sizes in vortices under turbulent gas flow, which experiences an additional lag in timescale concerning the accelerating gas resulting in a more uniform heat transfer between the particle and gas phase. Conversely, studies previously performed are for turbulent uniaxial flows, which may differ for devices in swirling vortical flows. Therefore, particle size effects and mass loadings may pose a non-linearity result in the vortex structured particle-laden flows under directly irradiated conditions in heat transfer. To add on, the heat transfer of particles within the receiver under intermittent solar irradiation needs to be investigated to understand the response of particle heat gain/losses through different particle loading and sizes in the vortex flows.

## **2.7 Research Gaps**

From the literature review, several critical operational (i.e., inlet flowrate, particle loading and particle size) and dimensionless (i.e. Froude number, Stokes number and swirl number) parameters have a significant influence on the thermal performance of the SEVR. It is also regulated by the non-linear radiative and particle trajectory that is challenging to predict without experimental and numerical study. Hence, new experimental data is required to understand better the coupling effects of these parameters on thermal performance. At the same time, the numerical study allows for better fundamental knowledge on the flow-field and heat transfer characteristics within the SEVR. The specific gaps in understanding the thermal performance of the SEVR is summarised as follows.

- Thermal equilibrium between gas and particle phases was previously assumed to account for the thermal performance of vortex receivers; however, limited data is available for the qualification of this assumption.
- CFD models have been generated to assess the fluid mechanics and particle trajectories of the vortex receiver; however, little is known about modelling the SEVR under irradiated conditions for possible applications in heated two-phase flows.
- Minimal experimental and numerical data were found to support and understand the effects of inlet volumetric loading, particle size and loading on the convective and radiative heat transfer mechanisms and thermal efficiency between these two phases.
- The influence of the Froude-Stokes and cyclonic regime is known to affect the isothermal flow field, but no work has been presented to assess the difference in thermal performance of the SEVR under these regimes.

- Limited work has been conducted to assess the effects of overventilation by suction on the thermal performance within the SEVR.

## **2.8 Aim and Objectives**

This project aims to systematically assess the trend of thermal performance in both single and two-phase flows (i.e. overventilation, particle/gas efficiency, heat losses, particle and temperature distribution) and provide a new understanding of the temperature and particle behaviour through both experimental and numerical methods as a function of the critical parameters (particle size, particle loading and inlet flowrates) within a lab-scale windowless SEVR with a radiation input. The objectives of this project are as follows:

- To understand the influence of overventilation by suction on the thermal efficiency and heat transfer within the SEVR.
- To characterise the key influencing dimensionless parameters (particle loading, Froude and Stokes number) of initial inflow conditions on the thermal efficiency and heat transfer within the SEVR.
- To understand the fraction of thermal energy partitioned between the gas and particle phases within the SEVR.
- To study the combined effects between the two distinctive flow regimes (i.e., Froude-Stokes and Cyclonic regime), particle residence time and distribution on the thermal performance of the SEVR.
- To develop a robust computational fluid dynamics (CFD) model with validated experimental data for assisting the fundamental understanding of key controlling parameters affecting the thermal performance within the SEVR.

## **Chapter 3 Methodology**

This chapter includes the research methodology, including the overall procedure for setting up the experimental campaign and the numerical simulation model. In the experimental study, a combination of techniques has been devised to obtain thermal performance data of the lab-scale SEVR. A numerical simulation framework was also developed with the CFD software to complement the validated experimental data in understanding the key mechanisms affecting the thermal performance inside the SEVR.

To outline each of the specific objectives, the methodology on characterising the key influencing dimensionless parameters of initial inflow conditions under irradiated conditions within the SEVR are highlighted in sections 3.1, 3.2, 3.6 & 3.7. Meanwhile, the methodologies listed in sections 3.3 and 3.6 aim to generate a new understanding of the effect of overventilation on the thermal efficiency and heat transfer. In addition, the development of a robust CFD model as highlighted in sections 3.4 & 3.5 is intended to determine the fraction of thermal energy partitioned between the gas and particle phases. This also includes assisting the fundamental understanding of key controlling parameters affecting the thermal performance, which explores the combined effects between the two distinctive flow regimes, particle residence time and distribution within the SEVR.

### 3.1 Task Calibration and Setting up of the Three-Lamp Solar Simulator

The thermal performance experiment adopts a piece of solar simulator equipment to replicate the realistic solar irradiation from the sun. The facility is located at the Thebarton Laboratory, the University of Adelaide, which is adopted based on several design methods [68]. The solar simulator design consists of three 6kW metal halide lamps (HMI 6000W/SE), as shown in Figure 9. These lamps are enclosed in their ellipsoidal reflector to concentrate radiative heat flux on the focal region. Metal halide lamps were used instead of Xenon arc lamps as they have a reduced risk of cascading failure and provide a better matching spectrum of the solar light source [69]. In addition, a Lambertian target is used to determine the flux profile projected by the three-lamp solar simulator.

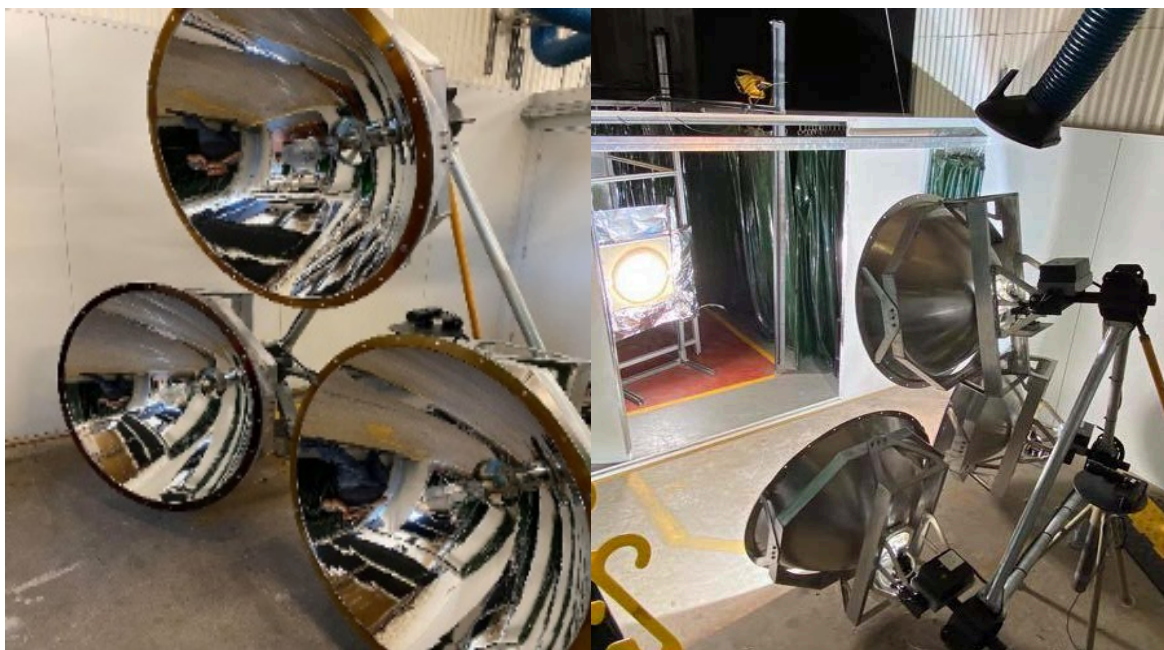


Figure 9. Three-Lamp Solar Simulator (left), solar simulator under operation (right).

#### 3.1.1 Alignment of the Solar Simulator

Alignment of the solar simulator is essential to ensure that the solar flux focuses accurately on the focal point of the aperture plane. The initial alignment is done using a ray simulation software known as *Tracepro* [70], which was applied to simulate and measure the distance of flux projected onto the focal point from the reflectors. After that, 3D Inventor CAD assembly drawing was used as a reference to provide an overview of the actual position from the lamp to the target. The distance of the target from the lamp reflectors was adjusted using a laser



measurement tool to ensure that the target is close to the position of the focal point. In addition, the tilt and yaw angles of each reflector were adjusted relative to that in the CAD drawing.

Before installing the actual lamps on the simulator, some alignment lamps were fitted on the socket to ensure that the light source intersects at the target centre. These lamps were adjusted individually using the 6-degree of freedom knobs that are located behind the lamp socket casing. When these lamps were concentrated at the centre, all alignment lamps were turned on and further adjusted until all rays were converged together on the target centre. Once this had been completed, the actual lamps were installed and turned on for secondary calibration. A CMOS camera (THORLABS DCC1240M) within the enclosure was used to inspect the target's pixel intensity and ensure that all rays are converged onto the target accurately. The process of secondary calibration involved the adjustment of the 6-degree freedom knobs for the rays to converge to the target centre. This is because the geometry of the lamp filament is slightly different, which influences the focal point at the target.

### **3.1.2 Image Processing**

The camera was placed orthogonally to the Lambertian target to capture the image of the flux projected, but before that, a grid calibration process was required to compare the size of the pixel number to the length scale of the image. A MATLAB code was developed to translate the number of pixels on the grid to an actual length scale based on the squares found in the grid.

### **3.1.3 Optical Calibration and Heat Flux Measurement**

The optical measurement technique adapted from [71] and [72] was applied to measure the radiative heat flux projected by the metal halide lamps. It uses a water-cooled plate with 250 mm x 250 mm dimensions coated with aluminium oxide shown in Figure 10a. At the same time, a camera captures the image of the target via a Neutral Density (ND) filter lens, which works by reflecting spectrally flat light onto the camera. The grayscale images taken from the camera are then calibrated against the radiative heat flux with respect to the grayscale range from the camera intensity [71, 72].

The heat flux gauge (Vatell TG1000-1 series,  $\pm 3\%$  accuracy,  $\pm 1\%$  repeatability) in Figure 10a was used to measure the voltage generated based on the heat flux intensity to account for possible calibration inaccuracies caused by spectral differences in the wavelength. The averaged heat flux value on the gauge area was taken at the three reference positions (A, B, C). The measurement of the heat flux gauge works by generating an electrical signal proportional (Voltage) to the total heat rate applied on the surface of the sensor. The measured voltage was

then converted to heat flux based on the manufacturer's scale factor. Locations of the gauge are then displaced across the positions to measure the intensity of the heat flux generated by the lamp at different points as shown in Figure 10b. After all measurements have been done, the heat flux data was used to correspond with the intensity of the camera to determine the radiative heat flux under different powers across the Lambertian target.

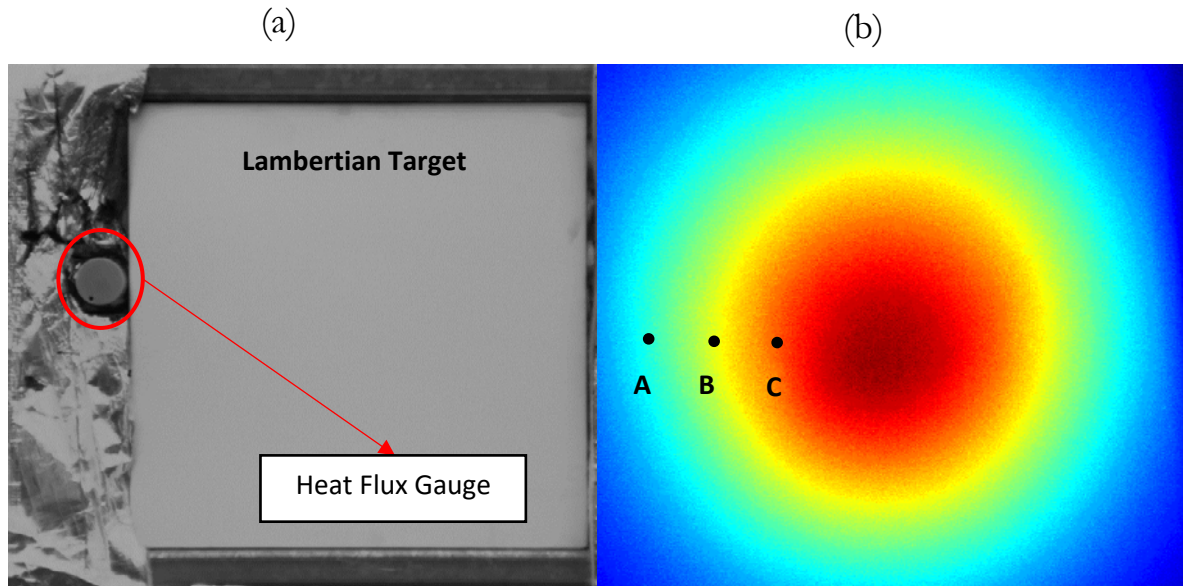


Figure 10. (a) Schematic diagram of the Lambertian target, (b) Reference position taken for the heat flux map.

The solar simulator's radiative heat flux and power need to be evaluated before experimenting. These steps were taken to assess the radiative heat flux projected by the solar simulator through the correlation of camera pixel intensity. The calibration line shown in the bottom graph of Figure 11 shows a calibration line between camera intensity (pixel value [0 – 255]: defines the brightness of the picture) to the radiative heat flux of the Lambertian target. The calibration line was extrapolated based on the heat flux gauge reading position and its position from the target centre. From this calibration graph, the three-lamp flux profile shown in Figure 12 shows that the three-lamp system can achieve  $338 \text{ kW/m}^2$  peak flux in the centre of the flux profile. To account for the heat flux entering the aperture of the SEVR, the masking function from the MATLAB image processing toolbox was used to define the total power entering the aperture, which was found to be approximately 2.10 kW.

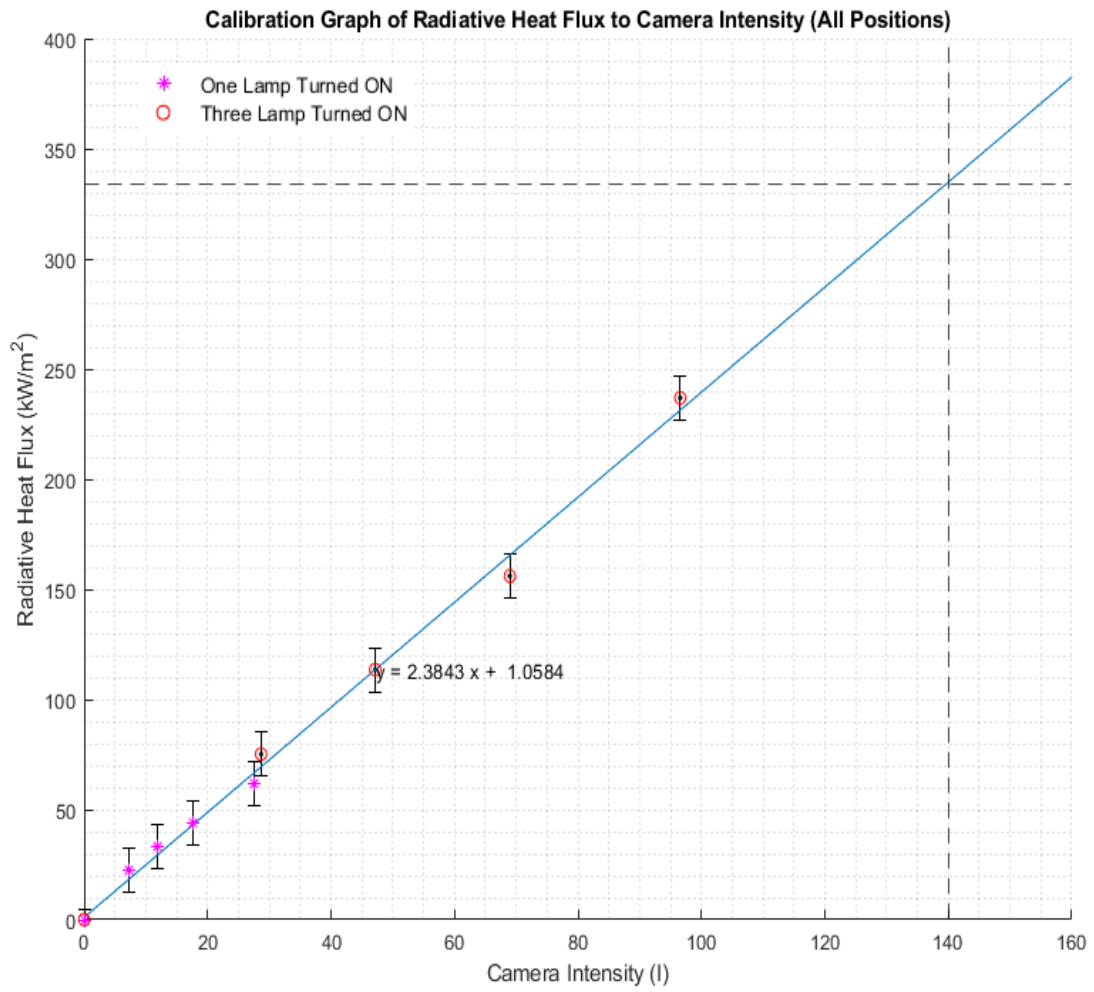


Figure 11. Calibration graph of the Radiative heat flux of the three-lamp solar simulator.

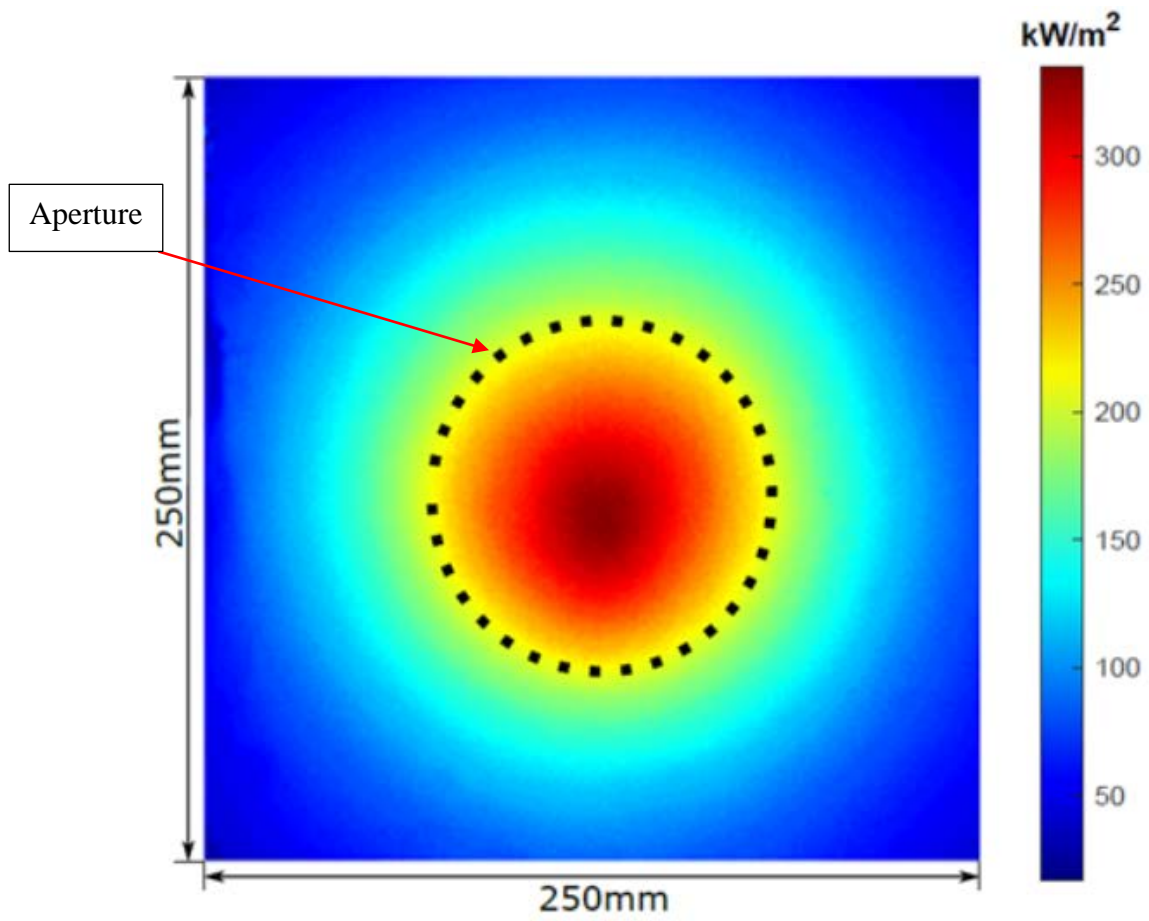


Figure 12. Three-lamp solar simulator flux profile generated at the Lambertian target (focal point, aperture plane).

## 3.2 Experimental Study on Thermal Performance of the SEVR

### 3.2.1 Experimental Arrangement

A schematic diagram of the device, showing key terminology and dimensions, is presented in Figures 13a and 13b, while the experimental rig setup is shown in Figure 13c. The SEVR features a 2-mm thick stainless-steel cavity with a 40° conical expansion to a cylindrical section that is insulated with ceramic and rockwool thermal insulation fibre mats (65-mm thick). It also features a radial outlet located at an axial position close to the aperture plane to expel the heated air and particles, together with two tangential inlet ports to inject compressed air and particles at the opposite end of the chamber. The particles selected for the investigation were made of CARBO CP ceramic due to their good stability in high temperature, high specific heat capacity and consistent near-spherical shape. The geometrical dimensions and thermal properties of the receiver and particles are presented in Table 1.

Table 1: (a) Geometrical and (b) Thermal properties of the SEVR, insulation and particles.

(a) Geometric properties		
	Parameter	Value
Receiver length	$L$ , (mm)	238
Receiver diameter	$D_c$ , (mm)	190
Cone angle	$\theta$ , (°)	40
Aperture diameter	$d_{ap}$ , (mm)	100
Inlet jet diameter (each)	$d_{in}$ , (mm)	6
Outlet jet diameter	$d_{out}$ , (mm)	11
Particle Sphericity	$P_{sp}$ , (-)	0.9
Particle Density	$\rho_p$ (kg/m <sup>3</sup> )	3250
(b) Thermal properties		
Insulation thickness	$L_{ins}$ , (mm)	65
Insulation Thermal conductivity	$k$ , (W/mK)	0.14
Particle specific heat capacity	$c_{p,p}$ , (KJ/kg K)	1.15
Emissivity of particles	$\varepsilon_p$ , (-)	0.95
Emissivity of reactor wall	$\varepsilon_{eff}$ , (-)	0.85

Two mass flow controllers (ALICAT MCR-Series,  $\pm 0.2\%$  accuracy) were used to control the mass flow rate of the compressed air for both tangential inlets. An ALICAT mass flow meter was used to measure the flow rate at the radial outlet of the device. A particle screw feeding system was applied to control the particle-feeding rate in the system. The solar source was introduced at the aperture plane of the device. For measurements of the thermal performance of the receiver, an array of 16 Type-K thermocouples with an acquisition rate of 1 second and specified standard error of  $\pm 1.5\text{ }^\circ\text{C}$  were installed throughout the device to obtain temperature measurements at the inlet, outlet ( $T_{a,o}$ ), internal and external wall ( $T_w$ ) sections. The outlet was connected to a water jacket heat exchanger to cool down the heated air and particles before being carried away by the induced draft fan. Overventilation by suction was employed at the outlet to control the particle and air egressing through the open aperture, as proven effective in previous studies [73, 74]. The methodology details on the influence of suction on the thermal performance of the SEVR will be discussed in Section 3.3. It is also important to note that the experiment is conducted under hot conditions with no wind factor.

All measurements of the device were conducted at the horizontal orientation, with the outlet facing downwards. The temperatures were logged continuously, with the time-averaged results were reported under steady-state conditions. During each test, particles were only introduced at steady-state conditions. The steady-state assumption was taken when all measured temperatures were within a fluctuation range of  $\pm 0.8\text{ }^\circ\text{C}/\text{min}$ . The warm-up time of the receiver to reach steady-state from cold conditions prior to particle injection was around 80 – 90 minutes, with gaps of 5 – 10 minutes required for each particle-laden test to reach the steady-state, while an additional 10 minutes was needed for the system to return its original condition before the subsequent tests. The maximum standard error in outlet temperature, thermal efficiency and energy balance was estimated to be  $\pm 0.5\text{ }^\circ\text{C}$ ,  $\pm 1.4\%$  and  $\pm 2.2\%$ , which are based on uncertainties associated with the mass flow, solar flux input and thermocouple measurements.

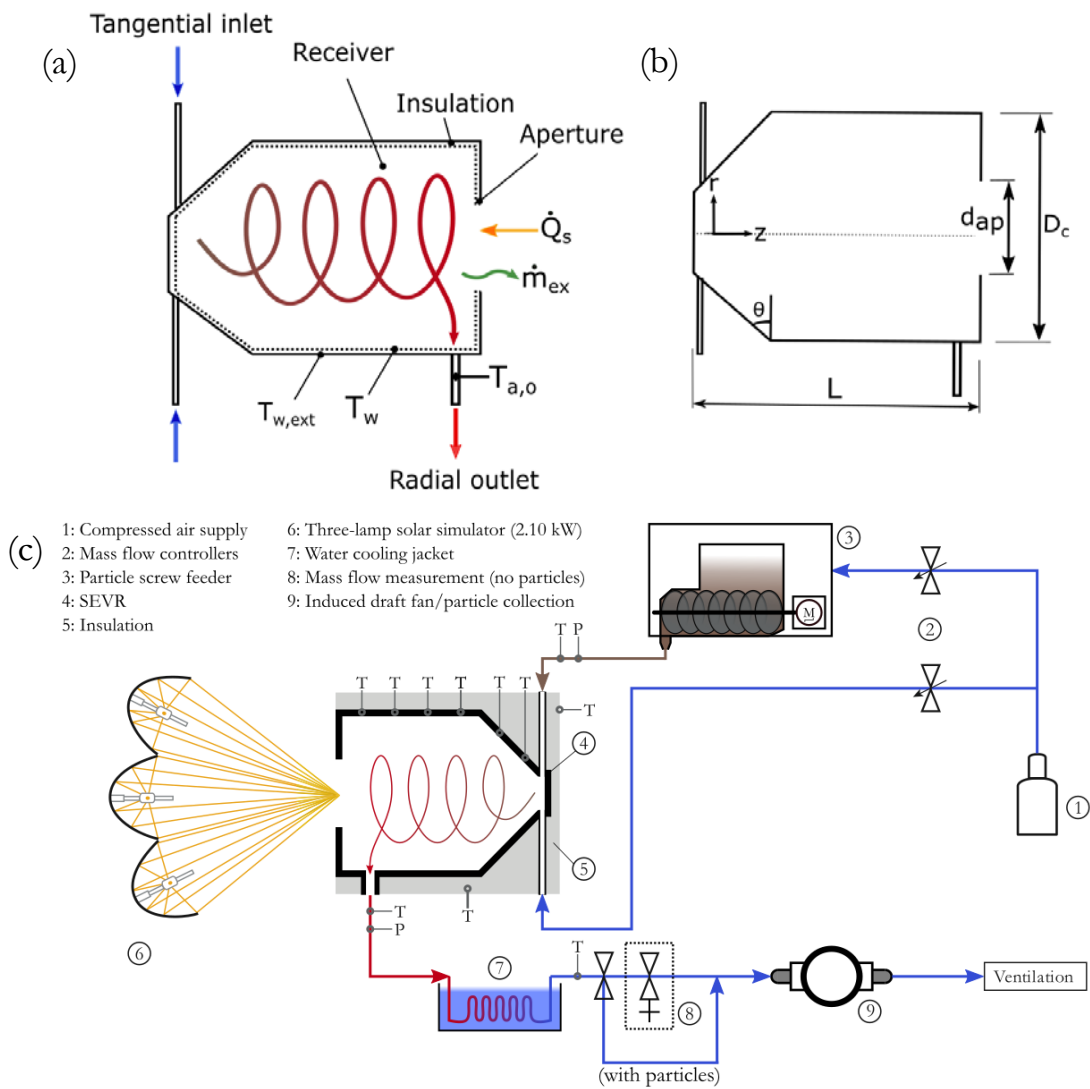


Figure 13: (a) Schematic Diagram of the SEVR (b) Geometrical details of the SEVR (c) arrangement of the SEVR experimental rig for the thermal performance study (Modified from earlier work [75]).

Throughout the experiments, the volumetric particle loading was maintained in the range between  $10e-5$  and  $10e-4$  to account for the two-way coupling regime on the interaction between gas and particles in the flow [44]. The particle flowrate is measured by weighting the mass of particles exiting the particle screw feeder instantaneously by evaluating the rate of mass change of the particles at an interval of 30 seconds. The calibrations were repeated five times for each sample of particle size. An averaged sample mass feeding rate was taken as a function of the value of the feeder controller display. The calibration graph for the particle screw feeder is shown in Figure 14.

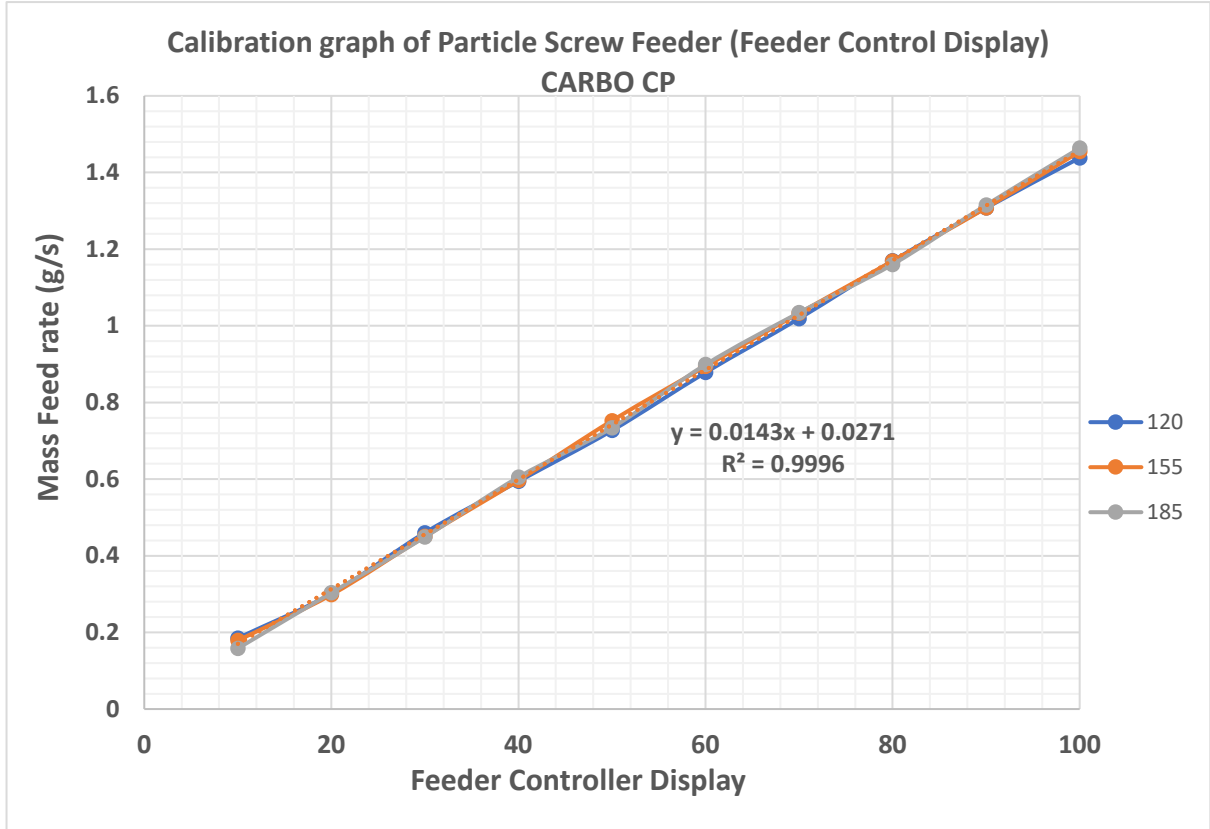


Figure 14. Particle screw feeder calibration graph for three different particle sizes.

### 3.2.2 Boundary Conditions

All measurements and simulations were undergone and assumed with the device fixed at a horizontal position (no tilt angle). Table 2 demonstrates all the operational conditions used for both experimental and numerical study. The inlet particle loading,  $\phi$ , defined as the ratio of particle-to-air volumetric flow rate, was varied between  $0 - 9.01e^{-5}$ , while the inlet air mass flowrate was varied between  $1.34e^{-3} - 2.68e^{-3}$  kg/s (i.e., 70 – 140 L/min, 20.63 – 41.26 m/s). The particle properties applied features a density of  $3250 \text{ kg/m}^3$  with mean particle sizes,  $d_p$ , of 120  $\mu\text{m}$ , 155  $\mu\text{m}$  and 185  $\mu\text{m}$ . To assume there are no particle egress, estimation through the measurements were taken based on the collection and weighting the particles escaping through the aperture. For a given level of suction, the measured value of the outlet mass flowrate,  $\dot{m}_{a,o}$ , was constant, and the value (in %) of the net air ingress (positive) into, or egress (negative) from the device as shown:

$$\alpha = 100 \left[ \frac{\dot{m}_{a,o} - \dot{m}_{a,i}}{\dot{m}_{a,i}} \right], \quad (3.1)$$

where  $\dot{m}_{a,o}$  and  $\dot{m}_{a,i}$  are air mass flow rate of the gas phase at the outlet and inlet section.



Table 2. A summary of the experimental and numerical operational conditions chosen for this study.

Parameters	Experimental		Numerical	
	Single-phase	Two-phase	Single-phase	Two-phase
Inlet air mass flow rate, $\dot{m}_{a,i}$ [g/s]	1.37, 1.57, 2.35, 2.75		1.37, 1.57, 2.35, 2.75	
Inlet air flow velocity, $U_{in}$ (m/s)	20.63, 23.57, 35.36, 41.26		20.63, 23.57, 35.36, 41.26	
Outlet air mass flow rate, $\dot{m}_{a,o}$ [g/s]	1.82, 2.08, 3.14, 3.65		1.82, 2.08, 3.14, 3.65	
Outlet air flow velocity, $U_{out}$ , (m/s)	16.31, 18.76, 28.10, 32.80		16.31, 18.76, 28.10, 32.80	
Mean particle diameter, $d_p$ ( $\mu\text{m}$ )	-	120, 155, 185	-	85, 120, 155, 185, 240
Inlet particle volumetric loading ( $\phi$ )	-	$2.96e^{-5}$ , $4.45e^{-5}$ , $9.01e^{-5}$	-	$2.96e^{-5}$ , $4.45e^{-5}$ , $9.01e^{-5}$
Input Solar (kW)	2.10	2.10	2.10	2.10
Net Air Ingress, $\alpha$ , (%)	33	33	33	33

According to a preliminary study [75], it was observed that an air ingress greater than approximately 15% is effective in preventing particles from egressing through the aperture. Thus, the study implements a greater tolerance of 33% for higher confidence to avoid the occurrence of particle egress, given that similar considerations were found experimentally elsewhere [74].

### 3.3 Proof-of-concept study on the effects of over-ventilation by suction

A  $5\text{kW}_{\text{el}}$  xenon lamp was initially applied as the radiation source for the initial proof-of-concept study on the effect of over-ventilation by suction on the thermal performance of the SEVR under single-phase flow conditions. In this study, the geometry of the receiver is similar to that found in Section 3.2.1. A total of 1.10 kW radiative heat was projected at the aperture plane of the SEVR. The lamp's solar flux distribution and focal point were identified based on a previous study conducted on the one lamp simulator [76]. A similar setup of the experimental rig was used, as shown in Figure 13c. These measurements were only performed for single-phase conditions to avoid the damage of the mass flowmeter by particles in the system. The detailed operational conditions can be found in Table 3. In addition, a similar procedure was undertaken with the three-lamp solar simulator at a later stage of the two-phase study, with similar trends of results found. According to previous works [74], the application of suction has been proven effective to prevent particle egress in other windowless particle-based solar receivers. Hence, the influence of overventilation by suction on the thermal performance was investigated for the windowless vortex-based solar reactor under single-phase flow conditions.

Table 3. A summary of operational conditions for the study on the effects of overventilation by suction.

Parameters	Value
Inlet air mass flow rate, $\dot{m}_{a,i}$ [g/s]	1.37 – 2.49
Inlet air flow velocity, $U_{in}$ (m/s)	20.63 – 38.30
Outlet air mass flow rate, $\dot{m}_{a,o}$ [g/s]	1.82 – 3.65
Outlet air flow velocity, $U_{out}$ , (m/s)	12.3 – 22.8
Input Solar (kW)	1.10
Net Air Ingress/Egress, $\alpha$ , (%)	-45 – 104

### 3.4 CFD Modelling of the Input Radiation Flux Profile

The commercial computational fluid dynamics (CFD) software, ANSYS/CFX 2019 R1, was chosen for the numerical study to provide insight into the heat transfer and particle distribution within the SEVR. The Gaussian-shaped solar flux input is modelled via the expression function adopting Equations (3.2) & (3.3) from the Gaussian power flux distribution over an aperture adapted from the previous work in [77], which measured the flux profile and distribution along with the receiver aperture.

$$\mu_{sim} = \sqrt{\frac{P_{in}}{2\pi F_{peak}}}, \quad (3.2)$$

$$\dot{Q}_s = 2\pi\mu_{sim}^2 F_{peak} [1 - \exp(-\frac{r_{ap}^2}{2\mu^2})], \quad (3.3)$$

here  $F_{peak}$  is the peak flux density at the centre line, and  $\mu_{sim}$  denotes the standard deviation,  $P_{in}$  is the total flux power entering from the simulator while  $\dot{Q}_s$  in Equation (3.3) is the power going into the aperture and  $r_{ap}$  is the radius of the aperture. Monte Carlo radiation ray tracing option was employed [78]. The total power obtained from the experiment as shown in Figure 12 was closely similar to the numerical study (i.e., less than 10% flux difference), which is modelled based on the Gaussian function equations. A total flux power of 2.25 kW was evaluated at the aperture plane, as shown in Figure 15. The Gaussian flux profile was similar to that seen in the previous study [79].

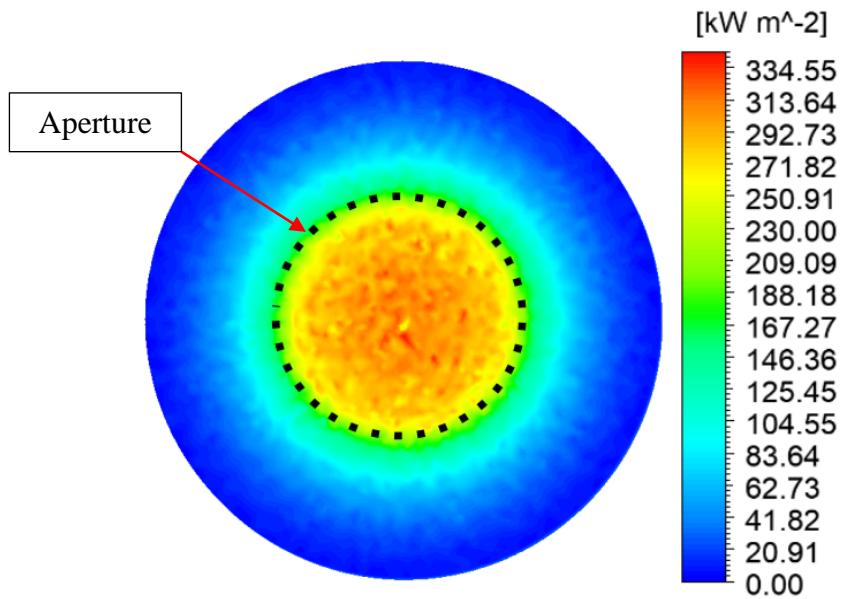


Figure 15: Radiation Flux profile at the aperture plane generated by the numerical study.

### 3.5 Numerical Model and Validation Results

The dimensions of the device were implemented into the numerical model using Design Modeller, and a non-uniform unstructured mesh was established with ANSYS/Meshing 19.3. A Mesh independence study was conducted using a coarse (0.8 million nodes), a medium mesh (1.8 million nodes) and a fine mesh (3.8 million nodes). Figure 16 compares the simulated outlet temperatures of the SEVR on all three meshes. It can be seen that the outlet gas temperature at 0.8 million nodes shows a more significant discrepancy when compared with the two other mesh sizes. It can also be seen that the simulated results of 1.8 and 3.8 million nodes have very minimal differences. Therefore, the mesh with the most refined nodes (i.e., 3.8 million nodes) was selected for this study.

The shear-stress-transport (SST) model was selected as the turbulence model. It shows a good agreement with flow-field results in strong curvature flows based on previous studies of particle-laden flows in rectangular jets and vortex gasifiers [80]. For each run, 100,000 spherical particles with specified diameters were injected into the CFD domain. The Lagrangian model was applied to track the trajectory of each particle through the discretised domain [81]. Effects of turbulence dispersion are also considered through the application of the random walk model [82].

The effects of gravity were included, and the device aperture was treated as an opening. The Semi-Implicit Method for Pressure Linked Equations (SIMPLE) algorithm was employed. Simulations were assumed to be converged upon temperature parameters reaching a steady state. All simulations were performed with 32-cores Intel Xeon-Skylake processors on the HPC Phoenix supercomputing facility located at the University of Adelaide. The CPU time for the simulations was between 5-8 hours for single-phase simulations and 25 – 40 hours for two-phase simulations. The boundary conditions of the CFD model are shown in Figure 17.

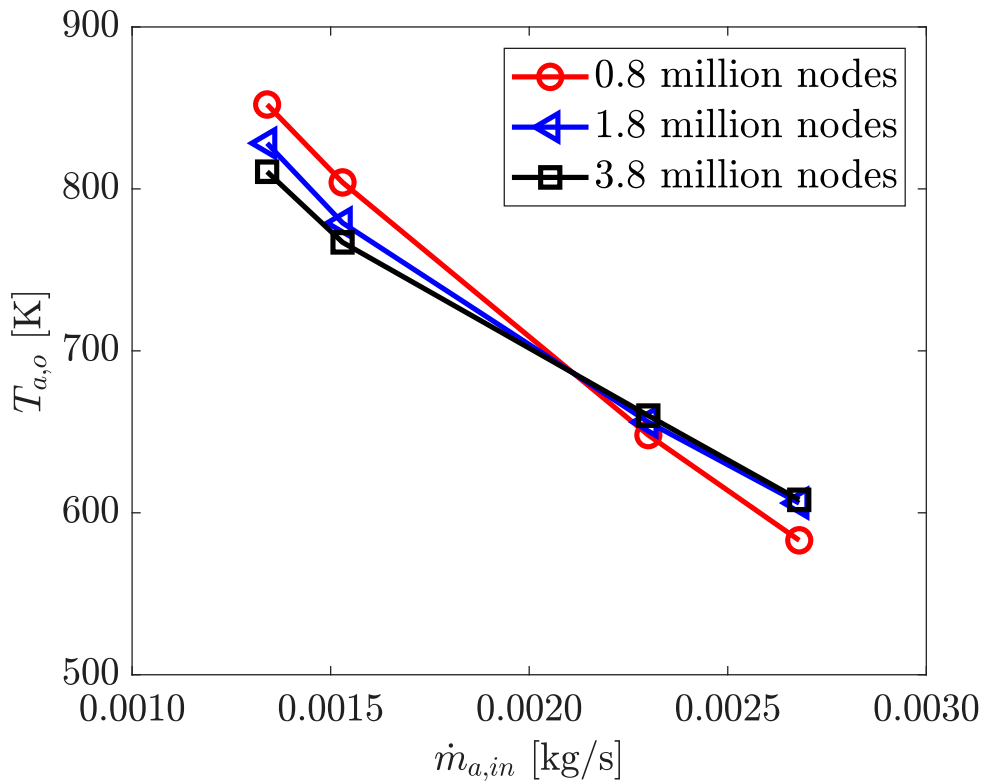


Figure 16. Simulated outlet temperatures at 3 different mesh sizes for various inlet mass flowrates under single-phase flow conditions.

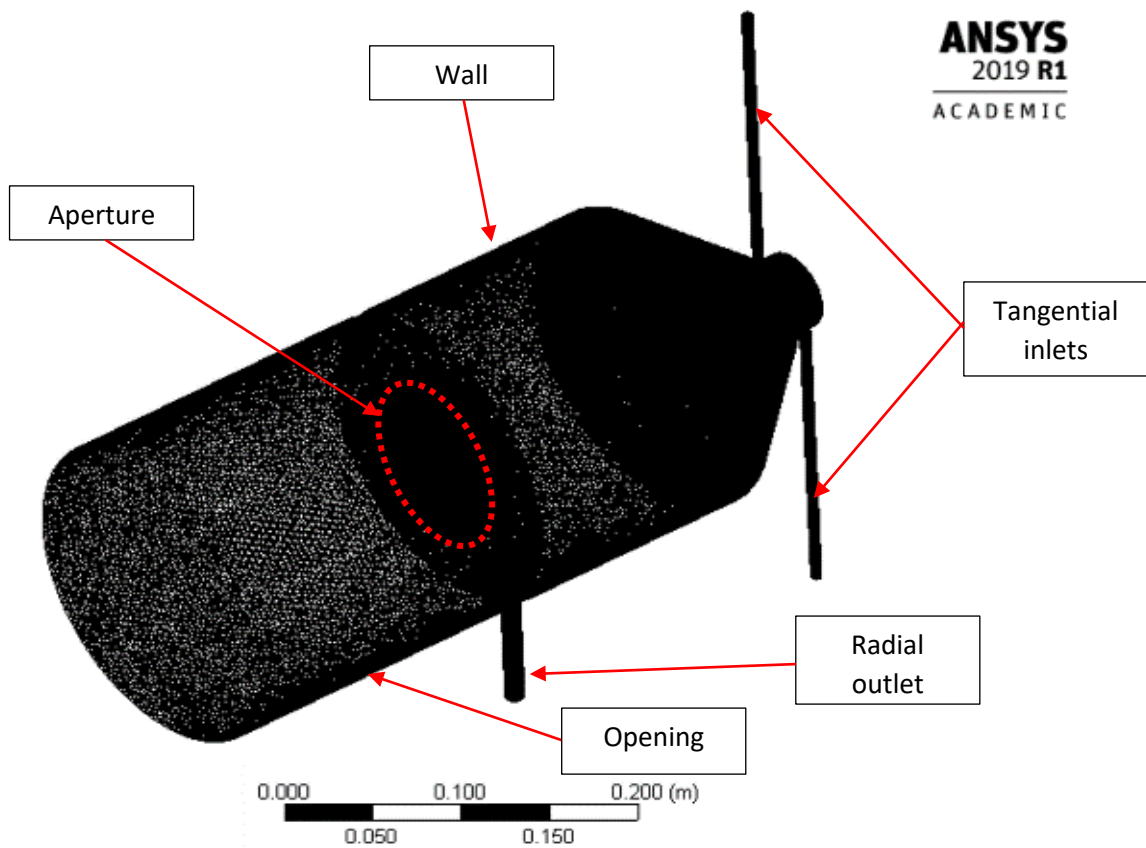


Figure 17. Boundary conditions of the lab-scale SEVR CFD model.

Table 4: Details of the validation process undertaken, and level of agreement obtained. The latter is reported as the difference between the experimental data and the numerical model regarding the agreement level of outlet and wall temperature.

Case(s)	$\dot{m}_{a,i}$ [kg/s] (x 10 <sup>-3</sup> )	$\phi$ (x 10 <sup>-5</sup> )	$d_p$ ( $\mu\text{m}$ )	$\bar{e}_{T_o}$ (%)	$\bar{e}_{T_w}$ (%)
SP-70	1.37	-	-	14.01	11.95
SP-80	1.57	-	-	12.61	11.43
SP-120	2.35	-	-	1.24	12.04
SP-140	2.75	-	-	3.62	11.35
TP-70-120-1	1.37	2.96	120	14.86	11.56
TP-70-120-2	1.37	4.45	120	15.75	11.33
TP-70-120-3	1.37	9.01	120	16.42	11.35
TP-70-155-1	1.37	2.96	155	14.04	12.14
TP-70-155-2	1.37	4.45	155	14.96	11.78
TP-70-155-3	1.37	9.01	155	16.21	11.10
TP-70-185-1	1.37	2.96	185	14.46	11.18
TP-70-185-2	1.37	4.45	185	14.69	12.52
TP-70-185-3	1.37	9.01	185	15.92	11.45
TP-80-155-1	1.57	9.01	155	14.72	11.24
TP-80-185-1	1.57	9.01	185	15.92	11.39
TP-120-120-1	2.35	2.96	120	3.27	12.41
TP-120-120-2	2.35	4.45	120	4.56	12.02
TP-120-120-3	2.35	9.01	120	4.39	12.37
TP-120-155-1	2.35	2.96	155	3.37	11.76
TP-120-155-2	2.35	4.45	155	5.55	11.84
TP-120-155-3	2.35	9.01	155	7.52	11.52
TP-120-185-1	2.35	2.96	185	2.88	11.43
TP-120-185-2	2.35	4.45	185	8.45	12.30
TP-120-185-3	2.35	9.01	185	8.01	11.36
TP-140-155-1	2.75	9.01	155	6.78	11.47
TP-140-185-2	2.75	9.01	185	6.44	11.22

Figure 18 shows the comparison of thermal efficiency within SEVR as a function of inlet air mass flowrate from previous and present studies for both measured and simulated cases [75]. For the current study, the enthalpy of air ingress in the device is neglected as the amount of air ingress is relatively minimal. The slight difference in thermal efficiency shows an acceptable level of confidence to validate experimental data. In addition, Table 4 also reports the details of the validation process undertaken and the level of agreement that was obtained with the experiment. The numerical study also involves an iterative process that requires the adjustment of parameters for various operational conditions. A simulation framework flowchart shown in Figure 19 was devised to understand and optimise the model. From the iterative process, the level of agreement of each study was assessed. The level of agreement is denoted by,  $\bar{e}$ , between the simulated and measured experimental outlet ( $\bar{e}_{T_{out}}$ ) and wall temperatures ( $\bar{e}_{T_w}$ )

for both single and two-phase conditions. The average error here can be denoted as the tolerant difference between the experimental and numerical study as described in Equations (3.4) and (3.5):

$$\bar{e}_{T_{a,o}} = 100 \left| \frac{\bar{T}_{a,o,exp} - \bar{T}_{a,o,num}}{\bar{T}_{a,o,exp}} \right|, \quad (3.4)$$

$$\bar{e}_{T_w} = 100 \left| \frac{\bar{T}_{w,exp} - \bar{T}_{w,num}}{\bar{T}_{w,exp}} \right|, \quad (3.5)$$

where  $T_{o,exp}$  and  $\bar{T}_{w,exp}$  is the outlet air temperature and averaged inner wall temperature from the experimental measurement, respectively, while  $\bar{T}_{a,o,num}$  and  $\bar{T}_{w,num}$  are the averaged air and wall temperature simulated from the numerical model. From Table 4, it was reported that all cases have a level of disagreement of less than 20%, which is sufficiently accurate to determine the trends of the thermal performance within the SEVR. Since the temperature of air from both measured and simulated cases are complementary, the comparison of outlet temperature between the two phases under simulated conditions are described by a percentage difference as follows:

$$\frac{\Delta T_{p-a,o}}{T_{a,o,tp}} = 100 \left| \frac{T_{p,o,tp} - T_{a,o,tp}}{T_{a,o,tp}} \right|, \quad (3.6)$$

Equation (3.6) determines the temperature difference between the air and particle phase in the numerical study with an averaged area at the outlet. Here, the air temperature of the two-phase flow is denoted by  $T_{a,o,tp}$ , while  $T_{p,o,tp}$  refers to the area weighted average particle temperature at the outlet.

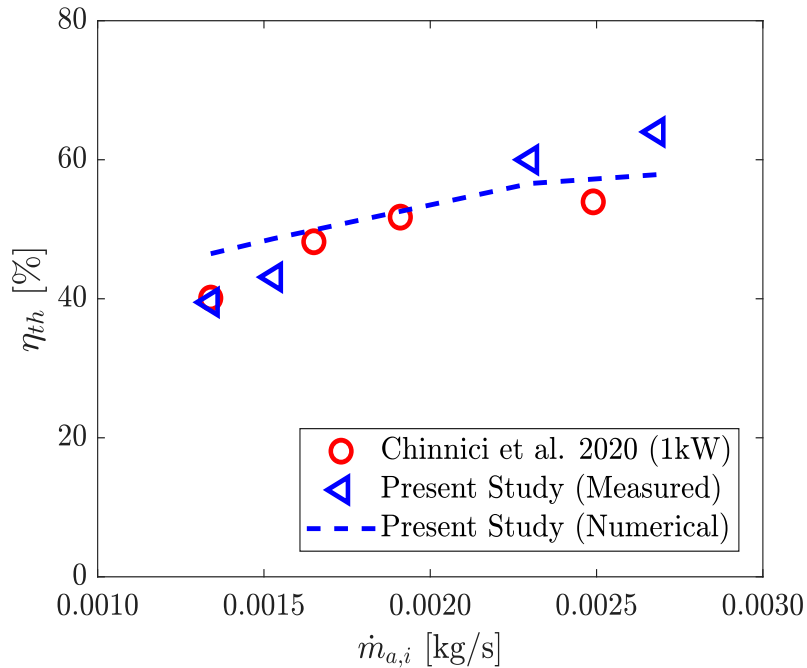


Figure 18. Thermal Efficiency of the SEVR as a function of the inlet mass flowrate under single-phase conditions with comparison between previous and present experimental studies [75].

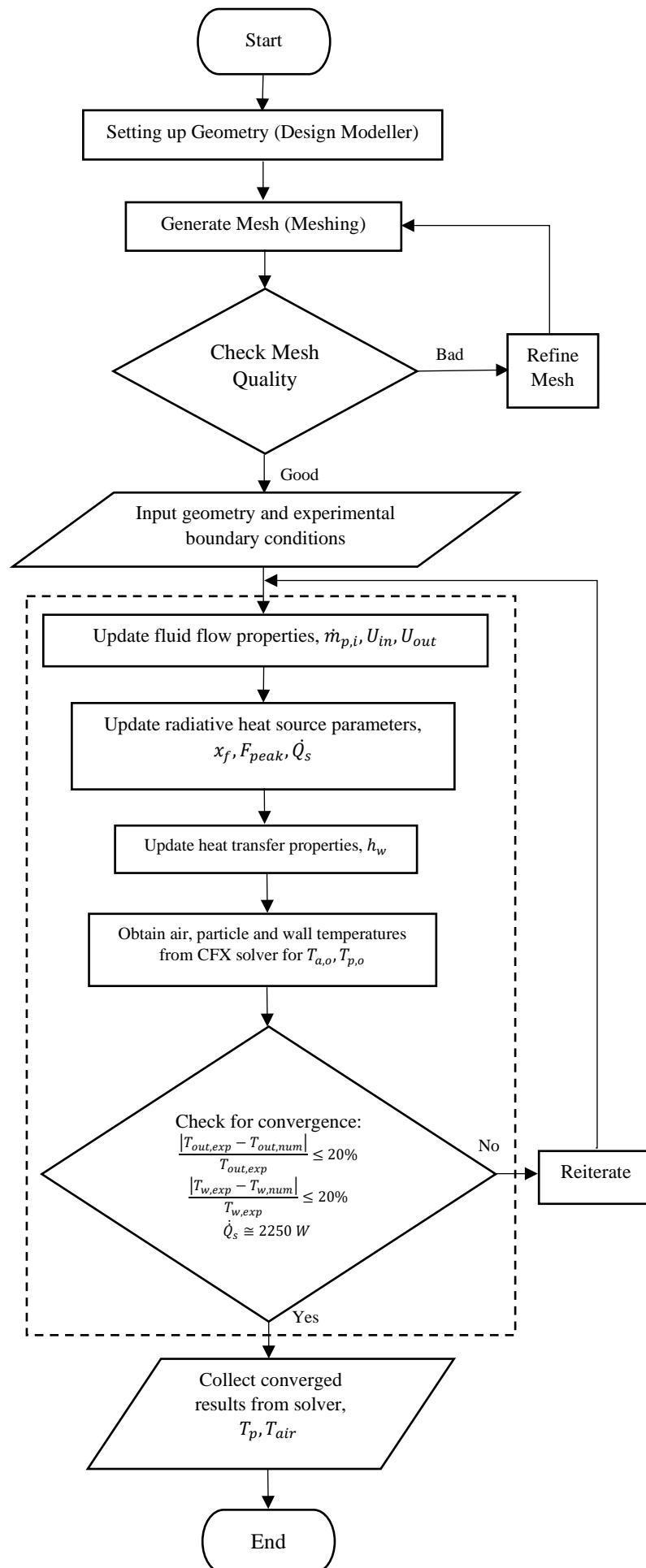


Figure 19. Flowchart of the numerical simulation framework.



### 3.6 Thermal Performance Analysis

The energy rate balance equation was applied to assess the influence of Froude and Stokes numbers as well as particle loading on the thermal performance of the lab-scale SEVR. The overall energy rate balance equation is as listed:

$$\dot{Q}_s = \dot{Q}_{abs} + \dot{Q}_{cond} + \dot{Q}_{loss,ap,rad} + \dot{Q}_{loss,ap,conv}, \quad (3.7)$$

where  $\dot{Q}_{abs}$  is the rate of energy absorbed by the mixture of gas and particle phase at the outlet of the SEVR, which can be defined as follows,

$$\dot{Q}_{abs} = \dot{m}_{a,o} c_{p,a}(T_{a,o} - T_{in}) + \dot{m}_{p,o} c_{p,p}(T_{p,o} - T_{in}), \quad (3.8)$$

where  $\dot{m}_{a,o}$  and  $T_{a,o}$  were the measured values of temperature and air mass flow rate of the gas phase at the outlet section.

The conduction heat term is estimated based on the mean external surface temperature of the insulation, termed as  $\bar{T}_{w,ext}$ , and the mean inner wall temperature,  $\bar{T}_w$ , thermal conductivity ( $k$ ),  $A_{SEVR}$  is the internal surface area of the SEVR and thickness of the ceramic insulation ( $L_{ins}$ ).

$$\dot{Q}_{cond} = \frac{kA_{SEVR}(\bar{T}_w - \bar{T}_{w,ext})}{L_{ins}}, \quad (3.9)$$

A term  $\dot{Q}_{loss,ap,rad}$  is defined as the radiative heat loss through the aperture, which is described with the following equation:

$$\dot{Q}_{loss,ap,rad} = \varepsilon_{eff} \pi r_{ap}^2 \sigma (\bar{T}_w^4 - T_{\infty}^4), \quad (3.10)$$

where  $\varepsilon_{eff}$  is the emissivity of the cavity receiver, and  $\sigma$  ( $5.67 \times 10^{-8} \text{ W m}^{-2} \text{ K}^{-4}$ ) is the Stefan-Boltzmann constant.

The convective heat loss term ( $\dot{Q}_{loss,ap,conv}$ ) through the aperture is determined as follows:

$$\dot{Q}_{loss,ap,conv} = \dot{m}_{ex} c_{p,a}(T_{a,o} - T_{\infty}), \quad (3.11)$$

where  $\dot{m}_{ex}$  is the amount of air exchanged through the aperture (ambient air entrained into or hot air leaving the device through the aperture); this is obtained by finding the difference between the measured values of the total mass flow rates of air at the inlet and outlet sections of the device ( $\dot{m}_{ex} = \dot{m}_{a,o} - \dot{m}_{a,i}$ ). The conductive heat loss term ( $\dot{Q}_{cond}$ ) for the current study is of less significance and thereby negligible as the conductive heat loss within the reactor reduces as the reactor is further scaled-up due to the increase of volume to surface area.

The overall thermal efficiency of the receiver,  $\eta_{th}$ , is defined to account for the heat absorbed by both the gas and particle phases,

$$\eta_{th} = 100 \left[ \frac{\dot{Q}_{abs}}{\dot{Q}_s} \right] = 100 \left[ \frac{\dot{m}_{a,o} c_{p,a} (T_{a,o} - T_{a,i}) + \dot{m}_{p,o} c_{p,p} (T_{p,o} - T_{p,i})}{\dot{Q}_s} \right], \quad (3.12)$$

In the numerical study, the particle and air efficiency are defined to find out how much energy is partitioned between the two phases,

$$\eta_{th,air} = 100 \left[ \frac{\dot{m}_{a,o} c_{p,a} (T_{a,o} - T_{a,i})}{\dot{Q}_s} \right], \quad (3.13)$$

$$\eta_{th,particle} = 100 \left[ \frac{\dot{m}_{p,o} c_{p,p} (T_{p,o} - T_{p,i})}{\dot{Q}_s} \right], \quad (3.14)$$

The mass flow rate of the particle at the inlet and outlet being equal with the assumption that there was no particle egressing through the aperture (i.e.,  $\dot{m}_{p,i} = \dot{m}_{p,o}$ ). It is important to note that the particle temperature was assumed equilibrium to the gas phase (i.e.,  $T_{a,o} = T_{p,o}$ ) in the experiments, the gas temperature at the outlet was used to calculate the thermal efficiency due to challenges in measuring particle temperature. To better understand heat transfer of the device and its potential configuration, the enthalpy ratio,  $\Delta H_{a-p}$ , was used to define as the enthalpy ratio of heat absorbed by the gas phase on the heat absorbed by the particle phase. The definition of the enthalpy ratio is as follows:

$$\Delta H_{a-p} = \frac{\dot{m}_{a,o} c_{p,a} (T_{a,o} - T_{a,i})}{\dot{m}_{p,o} c_{p,p} (T_{p,o} - T_{p,i})}, \quad (3.15)$$

To better characterise the efficiency, the exergy efficiency (the second law efficiency) is an effective method in analysing irreversible thermal processes as it provides an understanding that could not be obtained from the energy analysis. In solar receivers, this evaluates the portion of useful energy as well as the operational temperature extracted from the device. It also includes the energy that has been destructed into other forms. Derivation of this formula is based on several literature on exergy analysis of cavity receivers [51, 83]. The equation of the exergy efficiency,  $\eta_{ex}$ , is as listed:

$$\eta_{ex} = \frac{\dot{m}_{a,o} c_{p,a} (T_{a,o} - T_{a,i} - T_0 \ln \frac{T_{a,o}}{T_{a,i}}) + \dot{m}_{a,o} \left( \frac{Rg}{MW} \right) T_{a,i} \ln \left( \frac{P_{a,o}}{P_{a,i}} \right) + \dot{m}_p c_{p,p} T_0 (T_{p,o} - T_{p,i} - T_0 \ln \frac{T_{p,o}}{T_{p,i}})}{\omega \dot{Q}_s}, \quad (3.16)$$

$$\omega = 1 - \frac{4T_0}{T_s} + \frac{1}{3} \left( \frac{T_0}{T_s} \right)^4, \quad (3.17)$$

According to Petela's approach, equation (3.17),  $\omega$  is defined as the maximum useful work available from radiation, that is the absorbed solar radiation exergy rate from the parabolic

reflectors/reflective mirrors [84]. The source temperature ( $T_s$ ) is assumed as the average blackbody metal-halide lamp temperature and is considered to be around 5600K [85]. The dead-state temperature ( $T_0$ ) is the ambient temperature, and here it is set at 298K.  $R_g$  is the universal gas constant,  $MW$  is the molecular weight of air and  $P_{a,i}$  and  $P_{a,o}$  are the pressure of air at the inlet and outlet respectively. In addition, the exergy factor,  $\chi$ , is included as a measure of performance of the receiver, which can be defined as the fraction of exergy rate on the energy rate absorbed by the system. The equation is given as:

$$\chi = \frac{\omega \eta_{ex}}{\eta_{th}} = \omega \left[ \frac{\dot{m}_{a,o} c_{p,a} \left( T_{a,o} - T_{a,i} - T_0 \ln \frac{T_{a,o}}{T_{a,i}} \right) + \dot{m}_{a,o} \left( \frac{R_g}{MW} \right) T_{a,i} \ln \left( \frac{P_{a,o}}{P_{a,i}} \right) + \dot{m}_p c_{p,p} T_0 \left( T_{p,o} - T_{p,i} - T_0 \ln \frac{T_{p,o}}{T_{p,i}} \right)}{\dot{m}_{a,o} c_{p,a} (T_{a,o} - T_{a,i}) + \dot{m}_{p,o} c_{p,i} (T_{p,o} - T_{p,i})} \right], \quad (3.18)$$

### 3.7 Key Dimensionless Parameters

The use of non-dimensional operational parameters is essential to determine the trend of thermal performance within the device. Despite recent investigations using Froude and Stokes numbers as key metrics in assessing the particle residence time within the receiver under isothermal conditions, the coupling influence of these parameters under heated environments is currently unknown. Hence, the Stokes and Froude numbers were systematically evaluated based on the variation of operational parameters such as the inlet volumetric flowrate and particle size. The Froude-Stokes and cyclonic regimes are also highlighted here. As most gas and particle within the reactor occupy the cylindrical chamber for most of the period, the cone-cylinder intersection is taken as the reference position for the tangential velocity and characteristic length scale, similar to that in [40].

Table 5: The operational details of the Froude-Stokes and cyclonic regimes of operation, generated with four inlet tangential velocities and values of the key-dimensionless parameters based on CFD results.

Flow Regimes	Froude-Stokes		Cyclonic	
$\dot{m}_{a,i}$ [kg/s]	1.37	1.57	2.35	2.75
$U_{t,max}$ [m/s]	1.60	1.83	2.90	3.16
$Sk_c$ for $d_p = 85\mu m$	0.60	0.67	1.15	1.37
$Sk_c$ for $d_p = 120\mu m$	1.08	1.36	2.32	2.60
$Sk_c$ for $d_p = 155\mu m$	1.82	2.23	3.82	4.34
$Sk_c$ for $d_p = 185\mu m$	2.59	3.16	5.45	6.18
$Sk_c$ for $d_p = 240\mu m$	4.36	5.43	9.16	10.40
$Fr$	2.5	3.4	8.6	10.2

The Stokes number,  $Sk_c$  defined as how closely a particle follows the streamline of the gas phase at the cylindrical chamber of the receiver [86]. This can be evaluated as follows:

$$Sk_c = \frac{\rho_p U_{t,\max} d_p^2}{18\mu_f D_c}, \quad (3.19)$$

where  $U_{t,\max}$  is the maximum tangential velocity of the fluid, which is estimated based on the CFD model.

The Froude number is defined as the ratio between the inertial effect and gravitational force within a hydrodynamic system. This formula is assumed to be similar to a cyclone separator, which aims to centrifuged particles along the walls [39].

$$Fr = \frac{U_{t,\max}^2}{gR}, \quad (3.20)$$

Since the SEVR possesses a similar trait to a cyclone separator, the utilisation of tangential velocity as the key factor acting on the fluid can be accounted as the ratio of the inertial effect of the vortex flow to that of an external gravitational field.

The dimensionless particle residence time ( $\bar{\tau}_p/\tau_{nom}$ ) was evaluated based on the ratio of average particle residence time obtained the numerical study ( $\bar{\tau}_p$ ) to the nominal particle residence time ( $\bar{\tau}_{nom} = V_R/\dot{V}_{in}$ ) as evaluated by [50]. The average residence time was extracted from the numerical study, while the nominal residence time is the ratio of receiver volume to the air volumetric flowrate. Table 4 summarizes the calculated values of the dimensionless parameters for both the Froude-Stokes and cyclonic regimes, where two inlet flowrates were demonstrated for each of the regimes.

Another critical parameter is the swirl number ( $S$ ), which is defined as the ratio of tangential momentum flux to the axial momentum flux and is used to characterise the vortex intensity within a swirling flow [45].

$$S = \frac{\int_0^R \rho_f u_t u_{ax} r^2 dr}{R \int_0^R \rho_f u_t^2 r dr}, \quad (3.21)$$

where  $\rho$  is the density of the fluid,  $u_t$  and  $u_{ax}$  are the tangential and axial velocity components, respectively, and  $R$  is the radius of the cylinder.

## Chapter 4 Experimental study on the thermal performance

In this chapter, an experimental investigation is conducted to assess the influence of several key operating conditions, such as, overventilation by suction under different volumetric flowrates under single-phase flows. In addition, the effect of key dimensionless parameters such as volumetric particle loading, Froude, and Stokes number in the two-phase flows on the thermal performance of the SEVR was also reported.

### 4.1 Single-phase study: Influence of overventilation by suction

#### 4.1.1 Influence on wall temperature

Figure 20 presents the measured inner wall temperature distribution of the SEVR,  $T_w$ , under a fixed mass flowrate of air (i.e.,  $\dot{m}_{a,i} = 0.00017$  kg/s) with the variation of the net egress/ingress ( $\alpha$ ) at the outlet section through overventilation by suction. Please note that a positive ( $\alpha$ ) means a net air ingress through the aperture, while a negative ( $\alpha$ ) denotes a net egress of air through the aperture. Across all cases, it can be observed that most of the thermal energy is absorbed on the wall is highest at the conical section at  $z/L = 0.17$ , which is attributed to the angle of radiation from the solar simulator. As a result, the temperature in the front region is cooler than in the back region. It is important to note that the heat transfer via conduction is limited by the thermal conductivity of the stainless steel. Also, the front section is heated by the hot air via convection, which causes wall temperature at the near-wall region to be similar to that of the outlet temperature.

The wall temperature profiles of  $\alpha = -25\%$  to  $15\%$  are nearly identical, while upon reaching  $\alpha = 65\%$ , the wall temperature is slightly reduced. This can be attributed to the fact that air is transparent to the radiative flux from the simulator. Therefore, the primary heat transfer of the radiant heat from the simulator to the air is mainly absorbed by the reactor wall, then a certain fraction of heat absorbed by the wall is transferred to the air by both conductive and convective means, as shown in the back region ( $z/L < 0.5$ ). Hence, for cases of  $\alpha \leq 15\%$ , the flow-field and convective heat transfer in that region are not significantly affected by overventilation, while having more significant effects on the flow field and heat transfer at the aperture and outlet region. For a higher over-ventilation case of  $65\%$ , the flow-field structure is speculated to be affected by the high level of overventilation, which causes a reduction in the swirl number and nominal residence time, thereby reducing the gas temperature near the wall, resulting in a reduced wall temperature.

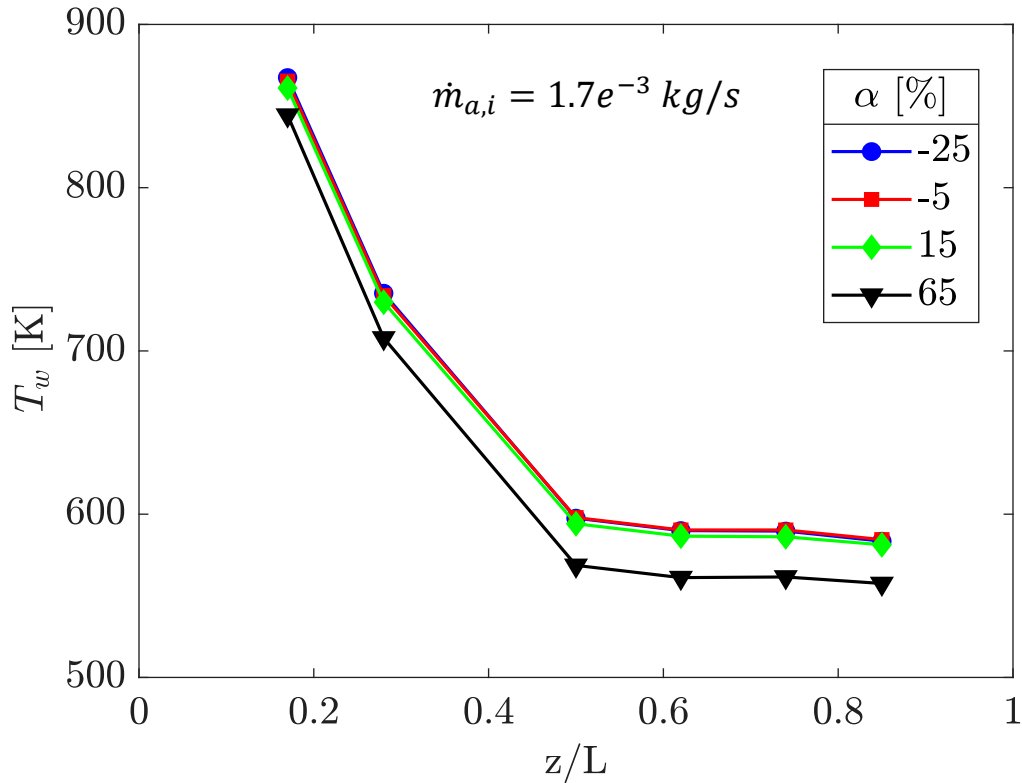


Figure 20: Axial distribution of the wall temperature of the receiver for a series of Net air ingress/egress with constant inlet mass flowrate.

#### 4.1.2 Influence on outlet temperature

Figure 21 presents the measured temperature of the SEVR at the outlet section,  $T_{a,o}$ , for different inlet mass flowrates ( $\dot{m}_{a,i}$ ) and suction levels of overventilation ( $\alpha$ ). An overall trend is identified, where, the  $T_{a,o}$  is decreased with the increase in the suction level under a fixed inlet mass flowrate. Similarly, it can be seen that under a given suction level, the increment of mass flowrate at inlets leads to a reduction in the  $T_{a,o}$ . It is as expected since the temperature increase in the SEVR is inversely proportional to the increase of the air mass flowrate, as shown in Equation 3.8. In addition, the increment of suction level contributes to the reduction of temperature rise in the flow. This can be attributed to the increased cool air ingress through the aperture, which reduces the temperature at the outlet.

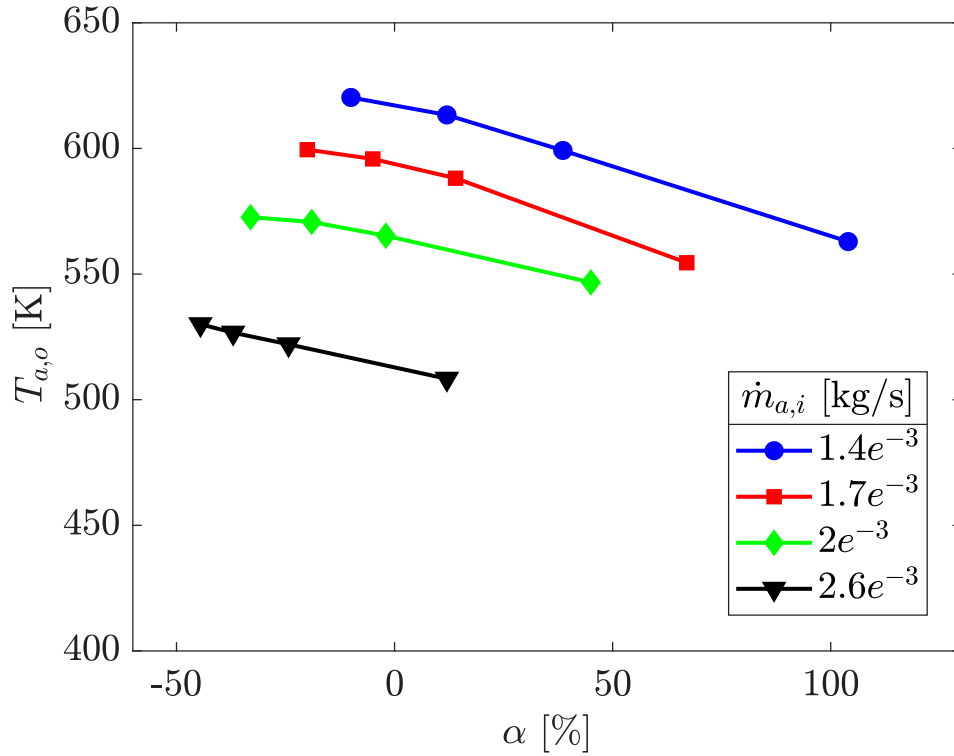


Figure 21: Measured values of gas outlet temperature as a function of suction level for various inlet mass flowrates.

### 4.1.3 Influence on Thermal efficiency and Exergy factor

As shown in Figure 22, as the suction level is increased, the thermal efficiency also increases. This can also be attributed to the greater heat transfer from the wall to the air through the increase of heat transfer coefficients, which are enhanced by the increased air velocity and increased temperature difference between air and the reactor wall. Furthermore, it is also speculated that the lower temperature in the SEVR indicates lower reradiation heat losses occurs through the aperture. These findings are consistent with the inverse trend between both energy and exergy efficiencies. It can be seen that the increment of suction level increases the thermal efficiency under a fixed inlet mass flowrate, however, leading to a reduction in exergy factor as shown in Figure 23. The reduction of exergy is due to the decrement of air temperature in the chamber and the outlet, as demonstrated in Equation 3.16 in the methodology chapter. In addition, it is expected that the mixing of ambient air and air from inlets by higher suction levels will lead to higher exergy destruction. As aforementioned, a certain level of over ventilation is required to remedy the particle egress through the aperture. Thus, the trade-off between exergy factor and particle egress through the aperture should be cautiously considered by optimizing the suction level to an acceptable level. From these trends, the lower values of thermal efficiency are currently hypothesised as of the small size of the reactor. Hence, further research on comparing the device at different scales is required to understand its efficiency.

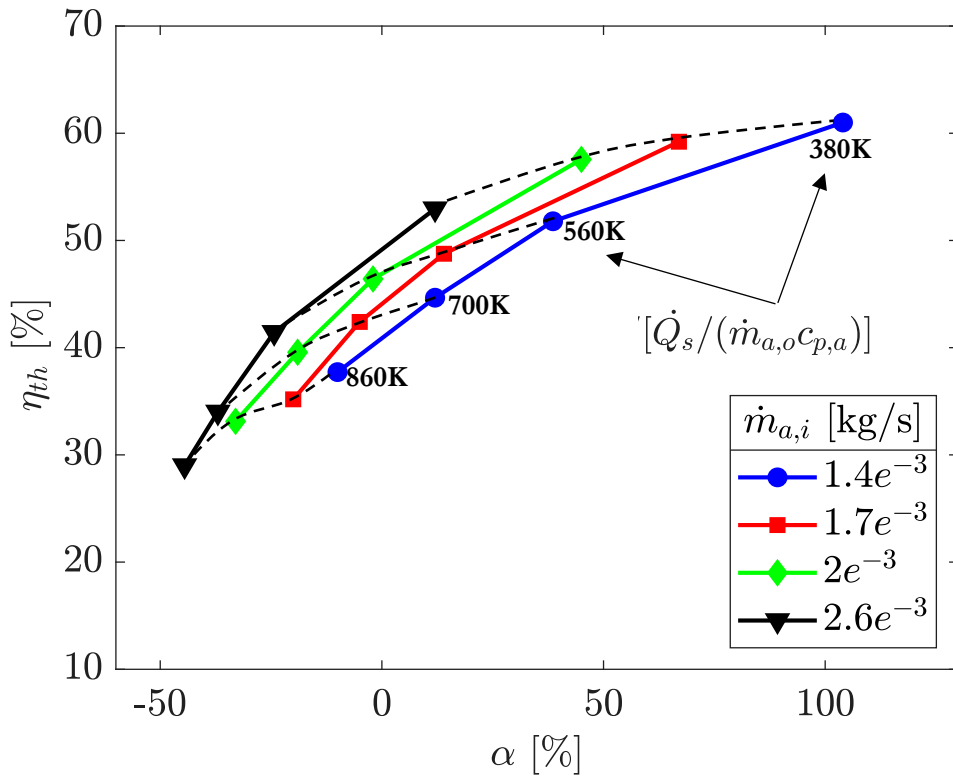


Figure 22: Measured values of Thermal Efficiency for different suction level and inlet mass flowrate.

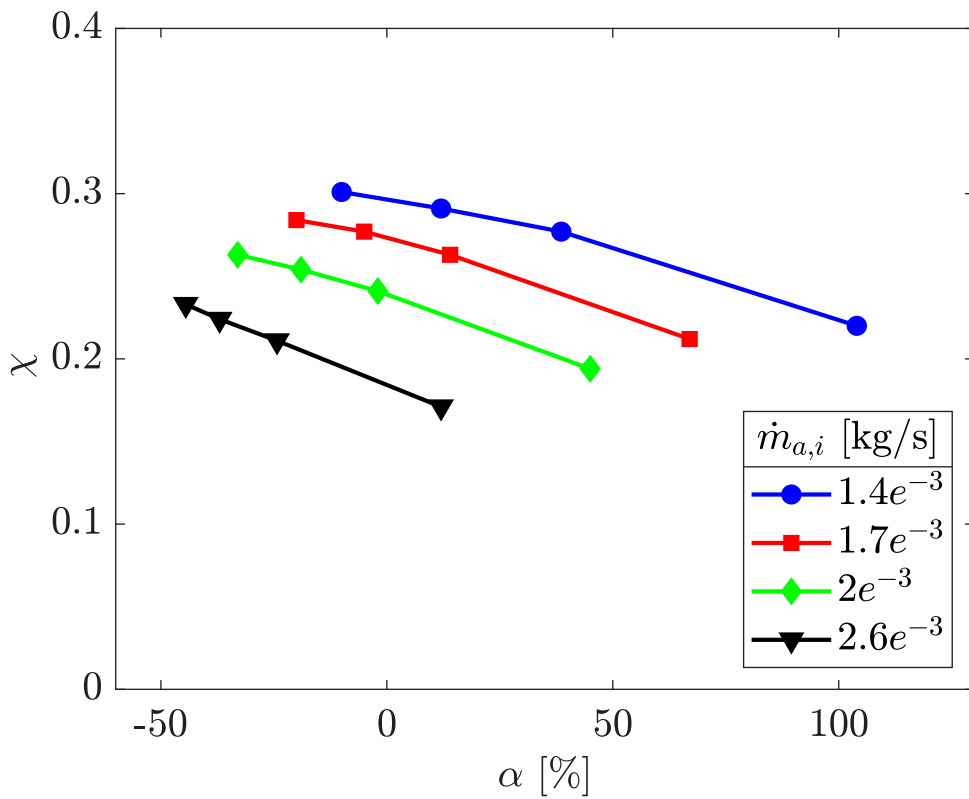


Figure 23: Measured values of Exergy Factor for different suction level and inlet mass flowrate.



## 4.2 Two-phase study: Influence of key dimensionless parameters on wall temperature

Figure 24 presents both the actual and normalised axial wall temperature distribution across the inner wall of the reactor from the experimental study concerning its influence by the key operational parameters, namely, the Froude number, particle volumetric loading and size. For most of the cases, an overall trend is spotted, that is, most of the solar energy is absorbed in the conical section ( $0 < z/L < 0.4$ ). This is as expected, as the solar beams are directed towards the cone from the aperture. The maximum normalised wall temperature obtained occurs at  $z/L = 0.17$ , which is attributed to the angle of radiation from the three-lamp solar simulator. As a result, the temperature in the front region is much cooler than in the back region, as discussed in section 4.1.1.

From Figure 24a & 24b, it can be seen that for both the Froude-Stokes regime ( $Fr < 4$ ) and cyclonic regime ( $Fr > 4$ ), the measured temperature of the wall decreases with an increase of air mass flowrate at the inlet. This is consistent with the measurements in the single-phase cases, and the reduced wall temperature can be attributed to the increased convective heat transfer due to the increased airflow rates at the inlet, i.e. the increased heat transfer coefficients and the increased temperature difference between the wall and the air. The difference between the wall and ambient air temperature is normalised by  $\frac{\dot{Q}_s}{(\dot{m}_{a,o}c_{p,a} + \dot{m}_{p,o}c_{p,p})}$ , that is an ideal approximation of temperature increase (without any heat losses to the ambient air) in the SEVR for a given  $\dot{Q}_s$ . The normalised wall temperature indicates how close the heat transfer in the SEVR is to the ideal scenario, i.e., no heat losses to the ambient environment. As shown in Figure 24b, the normalised temperature increases with the increase of air mass flow rates, which is opposite to the trend shown in Figure 24a. This confirms that the increase of the mass flow rates at the inlets enhances the heat transferred from the radiation input at the aperture to the air and particle phases in the SEVR. As shown in the trend of Figures 24c & 24d, as the wall temperature decreases, while the normalised temperature increases with the particle loading, this indicates that the flow of suspended particles within the reactor has an improved ability to absorb the radiant energy from the flow. In addition, the increment of particle loading also increases the heat capacity terms of the gas and particle phases. Therefore, the normalised wall temperature increases with the increment of particle volumetric loading. In other words, the increase of particle loading enhances the heat transfer performance in the chamber.

As shown in Figures 24e & 24f, it is seen that decreasing the particle size leads to a slight increment of normalised wall temperature. The particle size reduction leads to an increment of the number of particles in the flow for a fixed particle mass flowrate in the inlets. It was found that the ratio of change of total particle surface area for different sizes such as 185 microns to 155 microns is 0.7, while the ratio of total particle surface area of 155 microns to 120 microns is 0.59; thus, the increment of particle surface area leads to a slightly enhanced heat transfer in the chamber. Similarly, slightly greater attenuation of the solar flux by smaller particles results in a higher wall temperature at the conical section, which was also observed in the 1-D mathematical model in [9]. Although the difference between the particle sizes is minimal (i.e., less than 6%), it can be claimed that decreasing the particle sizes can slightly enhance the heat transfer, as normalised wall temperature increases for the 120-micron particle. It is also important to note that the Froude number is dependent on the tangential velocity under a fixed geometry and orientation. Hence, the variation in tangential velocity would result in a different Froude number. The use of Froude number is beneficial in estimating the trend of thermal performance in a device at scale, where the characteristic length is varied. The current study aims to understand and obtain the trend of the thermal performance dataset, which is significant in outlining the thermal performance of the receiver at different scales.

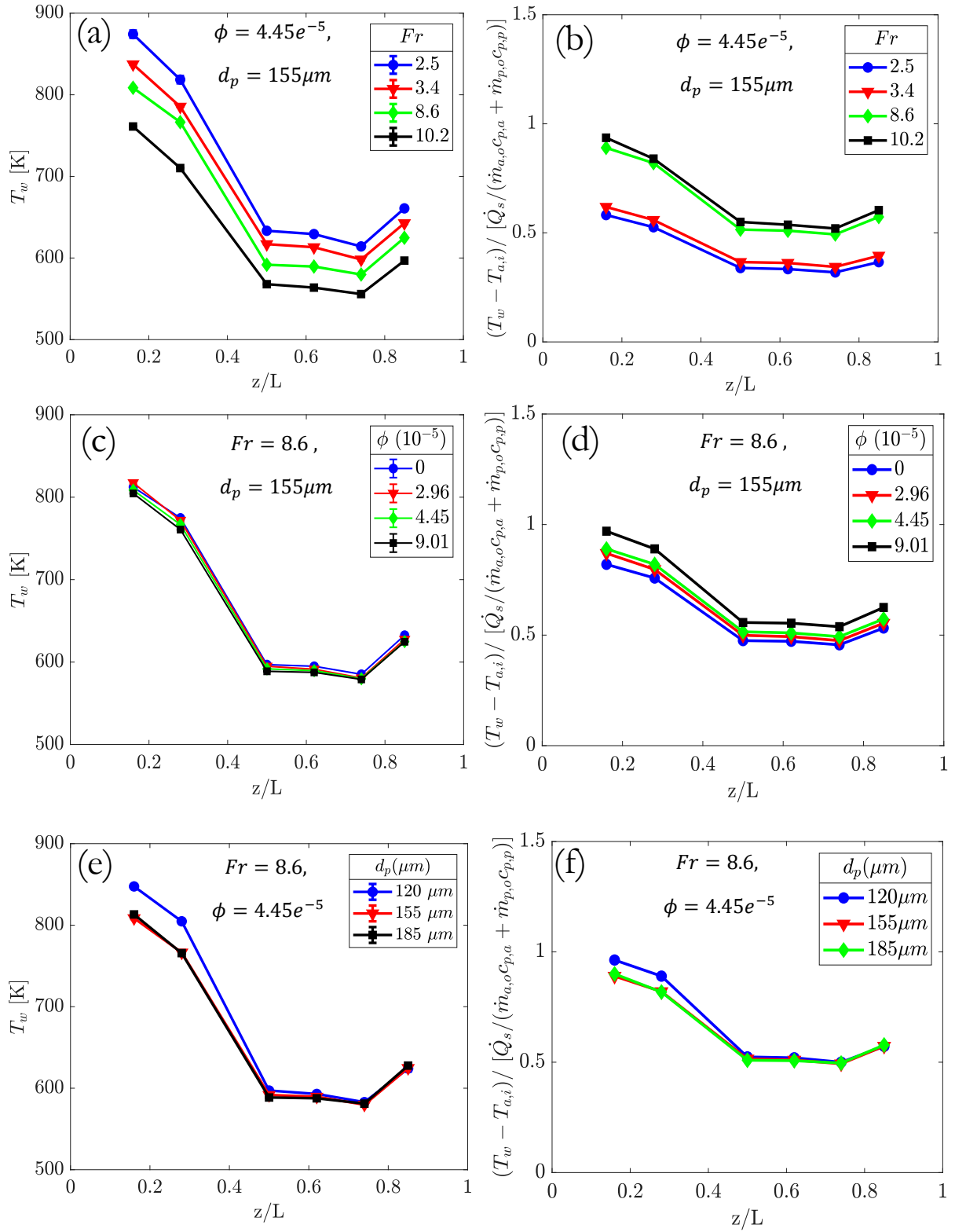


Figure 24: Measured values of wall Temperature and normalised wall temperature as a function of (a, b) Froude number (c, d) particle volumetric loading (d, e) particle size.

### 4.3 Two-phase study: Influence of key dimensionless parameters on outlet temperature

#### 4.3.1 Effects of Froude number

Figure 25 demonstrates the effects of the key dimensionless parameters ( $Fr$ ,  $\phi$ ,  $Sk_c$ ) for both measured air temperature and normalised air temperature at the outlet obtained from the experimental campaign. From the results shown in Figures 25a & 25b, it can be seen that the outlet temperature is influenced by the inlet tangential flow velocity of the Froude number, as previously mentioned in Section 4.2. It is shown that the increment of the Froude number in the gas phase at a constant energy input decreases the temperature rise of the two-phase flow. This is as expected since the increase of inlet volumetric flowrate reduces the temperature rise, as shown in Equation 3.8. It is also observed that as the Stokes number is increased (by increasing particle diameter  $d_p$ ), the temperature at the outlet decrease for  $Fr = 2.5, 3.4, 8.6$  but not for ( $Fr = 10.2$ ); this is due to the greater surface area of the particles, which allows for absorbing more radiant heat. The addition of particles increased the total heat capacity of the two-phase flow to absorb heat. With the increase of Stokes number (i.e., particle size), the total surface area of particles decreases; thus, particles absorb less radiant heat, leading to a slight decrement of the temperature increase. It is unclear what causes the outlet temperature to decrease at the outlet when particle size increases from 155  $\mu\text{m}$  to 185  $\mu\text{m}$  for  $Fr=10.2$ . This may be attributed to the measurement error. An agreement was also found in Figure 25b, which shows that as the heat capacity term normalises the outlet temperature, more energy is absorbed by the two-phase flow when the Froude number increases, as seen in Figure 25a. As the Froude number increases, it is expected that the rate of air exchanged at the aperture also increases. This causes flow recirculation to occur in allowing more hot air from within the cavity to egress through the aperture, while cold ambient air ingresses the device through back mixing from the recirculating flow.

Figures 26a & 26b presents both the outlet and normalised outlet temperature of the SEVR for fixed particle size and by varying values of particle loading and Froude number. It is observed that the outlet temperature is influenced by both Froude number and particle loading. The increment of the Froude number increases the temperature drop while providing a rise in the energy balance. This is consistent with trends observed in single-phase study because increasing mass flowrate of both gas and particle is expected to decrease the temperature rise by an energy balance in the two-phase flow. The increased outlet temperature can be attributed to the increased convective heat transfer due to the increased airflow rates at the inlet.

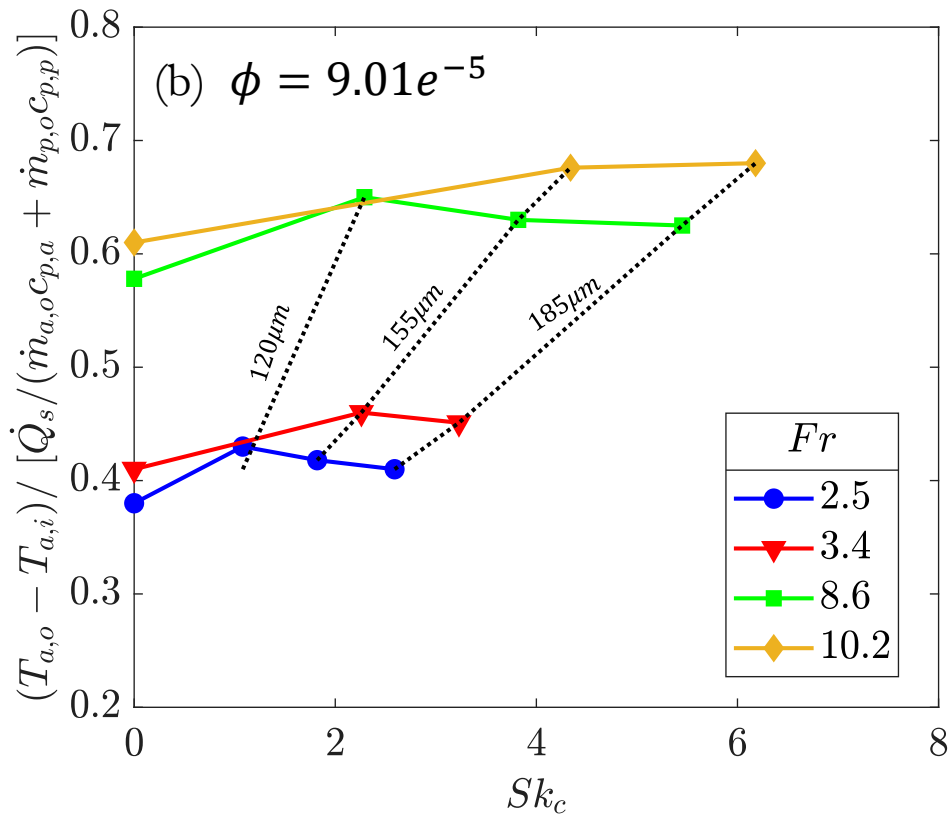
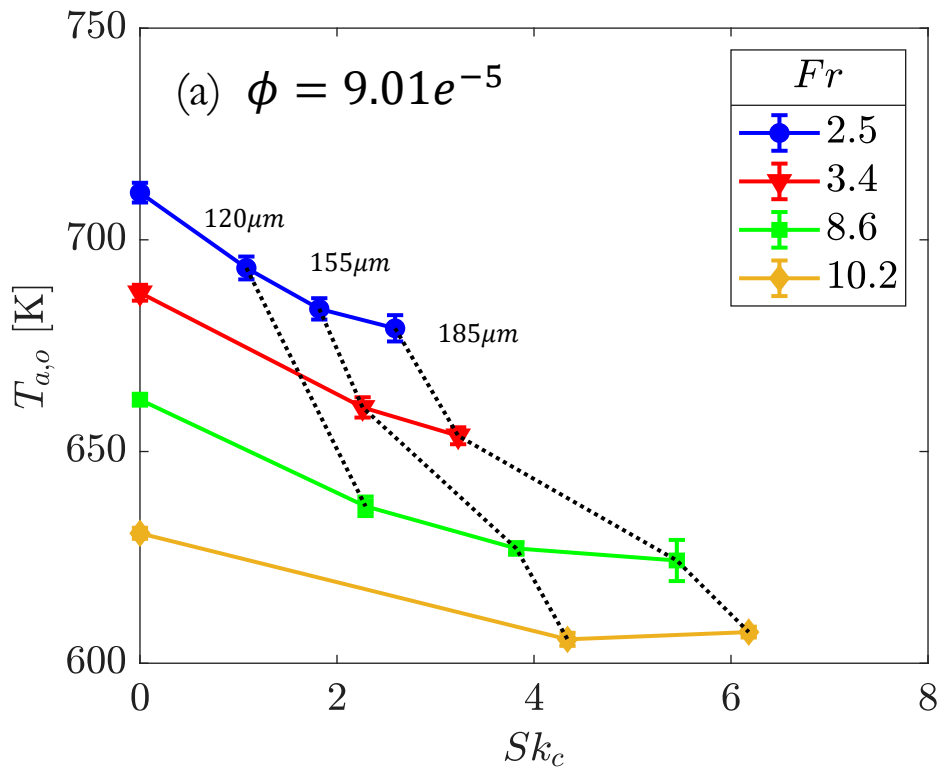


Figure 25: Measured values of (a) outlet air temperature at a constant particle loading for different values of Froude number. (b) Normalised outlet air temperature at a constant particle loading for different values of Froude number.

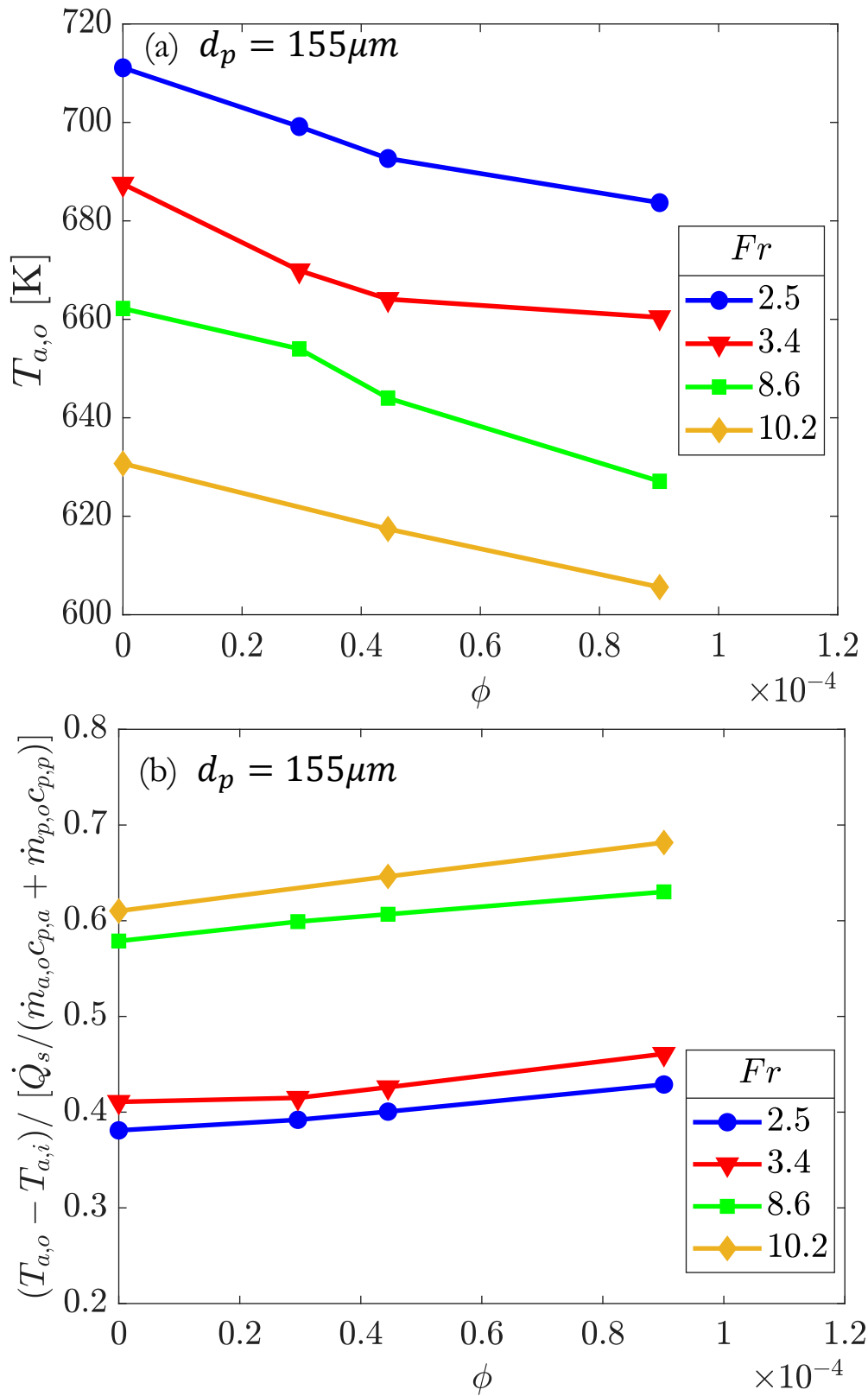


Figure 26: Measured values of (a) Outlet air temperature at a constant particle size for different values of Froude number. (b) Normalised outlet air temperature at a constant particle size for different values of Froude number.

### 4.3.2 Effects of particle loading and Stokes number

The result of Figure 27a shows that as the particle loading is increased, the temperature at the outlet gradually increases. A general trend clearly shows that the increment of Stokes number (by increment of particle sizes) leads to a decrease in outlet temperature, indicating deteriorated overall heat transfer from the radiation input to the gas and particle phases in the SEVR. The particle loading positively affects the overall heat transfer in the chamber, evidenced by the increasing normalised outlet temperature shown in Figure 27b, while a negative effect on the measured outlet temperature is shown in Figure 27a. As expected, increasing particle loading will have increased particle surface area and increased heat capacity. The increased particle surface will enhance the heat transfer from the radiative source to the particles and air around the particles.

Moreover, the increased overall heat capacity will reduce the absolute temperature measured at the outlet. It is worth noting that for low particle loading ( $\phi = 2.96 \times 10^{-5}$  and  $4.45 \times 10^{-5}$ ), the effects of Stokes number on the temperature at the outlet and the overall heat transfer are minor while for a high particle loading ( $\phi = 9.01 \times 10^{-5}$ ), the effects can be more significant. This is because the increment of particle size (i.e., Stokes number) weakens the heat transfer in the chamber due to the reduced total surface area of particles; however, this effect is not apparent for low particle mass loadings. With the increment of particle mass loading, it is expected that the effect will be more pronounced.

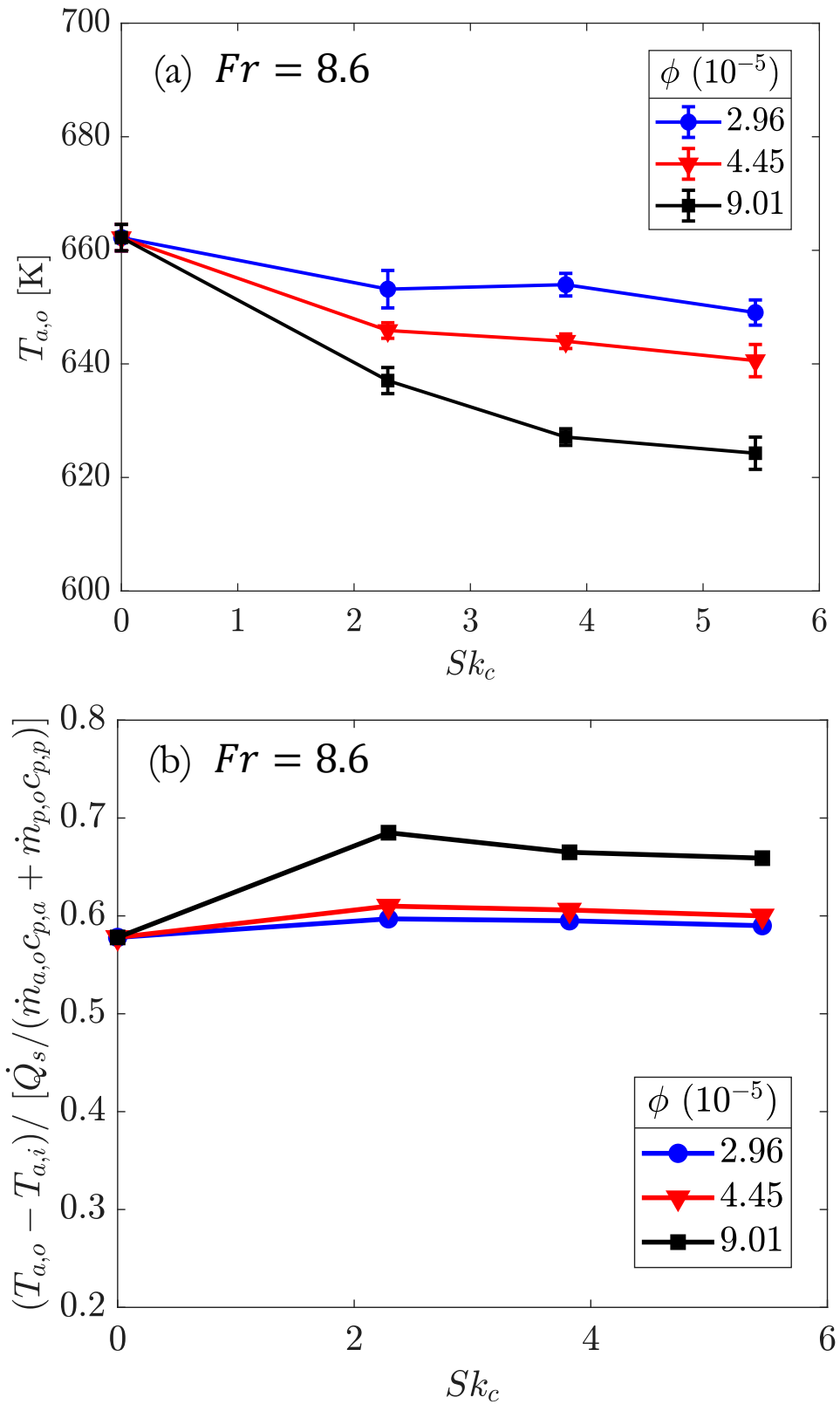
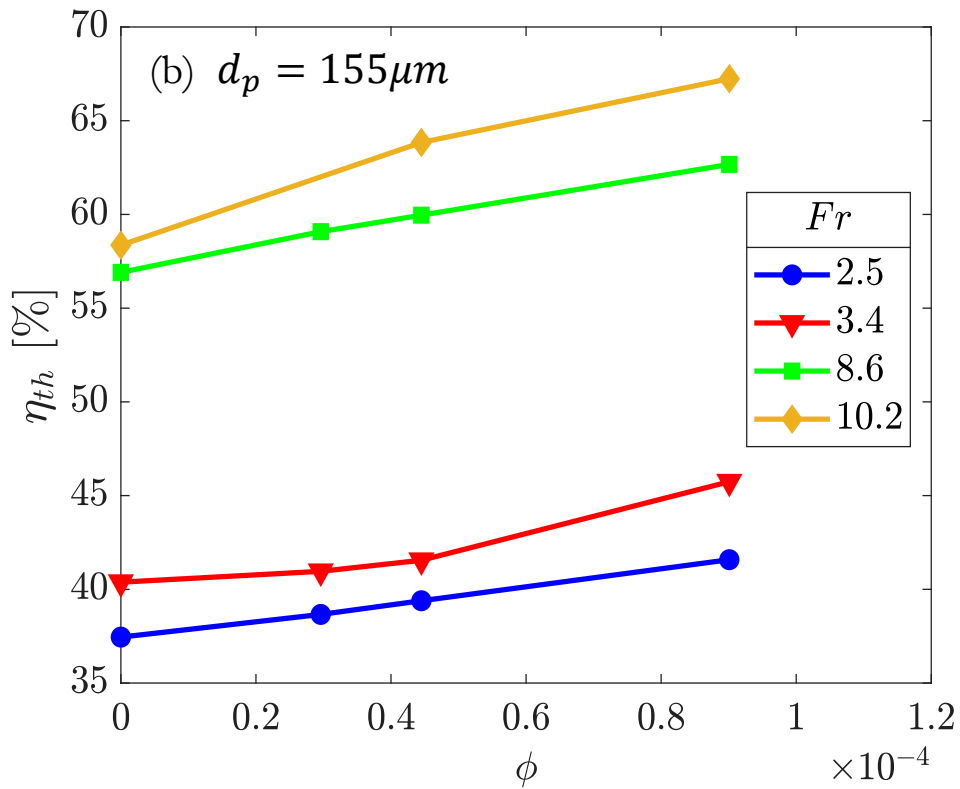
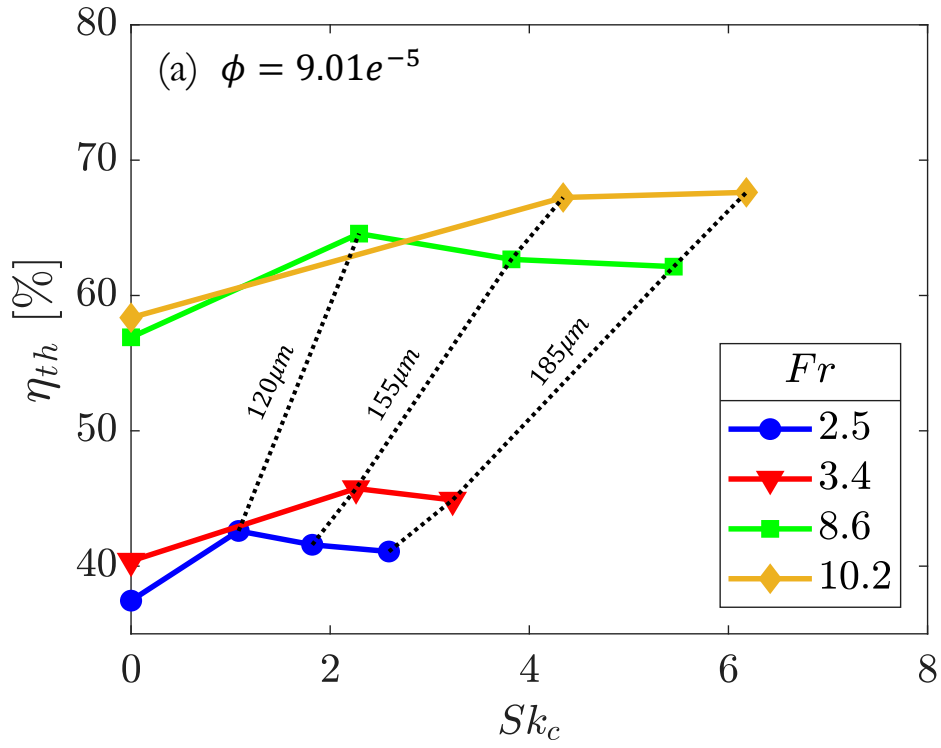


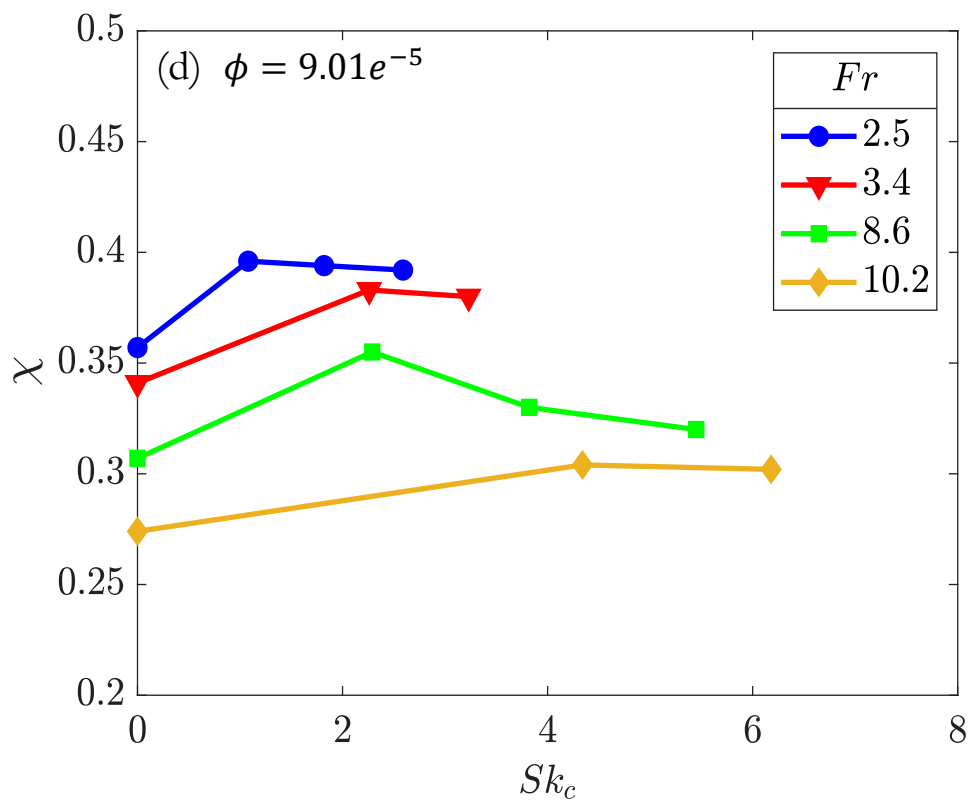
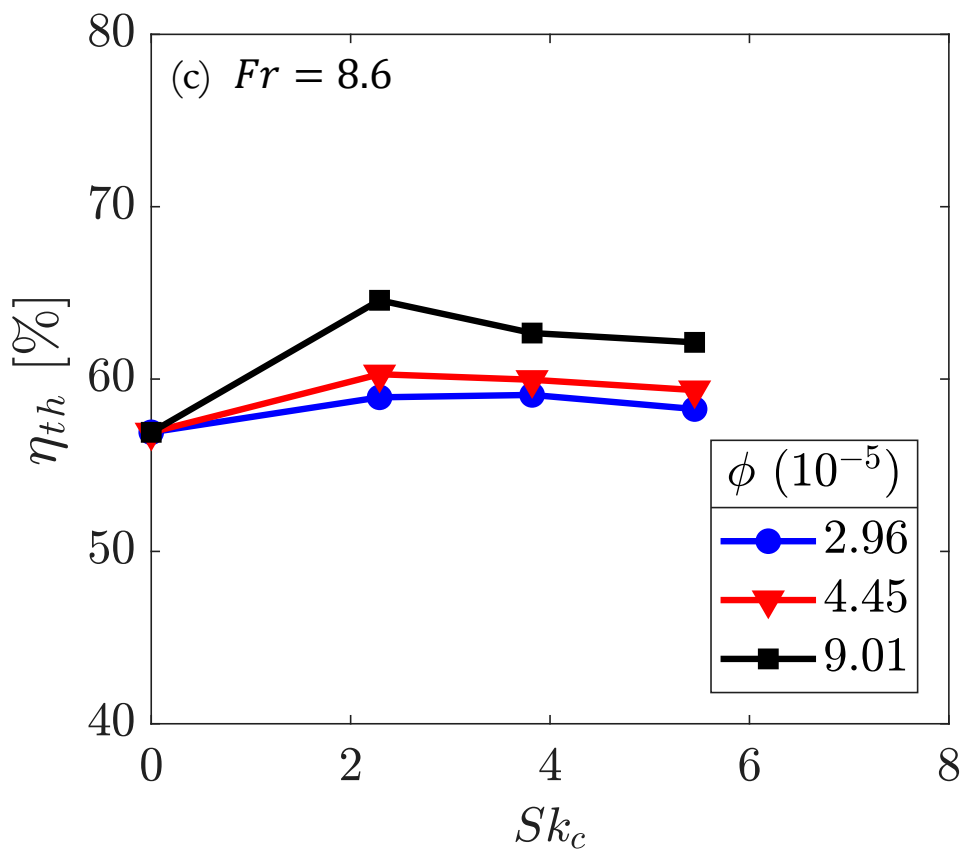
Figure 27. Measured values of (a) Outlet air temperature at a constant Froude number for different values of particle loading. (b) Normalised outlet air temperature at a constant Froude number for different values of particle loading.



#### **4.4 Two-phase study: Influence of key dimensionless parameters on thermal efficiency and exergy factor**

Figure 28 presents the influence of Stokes number on the thermal efficiency of the SEVR. The efficiency of the experiment is evaluated based on Equation 3.12. It is important to note that the particle temperature at the outlet is assumed equilibrium to that of the local gas phase in the experiments due to difficulty in measuring particle temperature. As shown in Figure 28a, when the inlet flow velocity increases, the Froude number increases, resulting in increased overall thermal efficiency due to increased heat capacity and enhanced heat transfer. Figures 28b & 28c shows the dependence of thermal efficiency on particle loading; as the particle loading increases, the energy absorbed by the particle phase is increased due to the increment of heat capacity of the two-phase flows and improved heat transfer mainly due to the increased radiation absorption by particles. It can also be seen in Figure 28d, for a fixed particle loading, the increment of the Froude number leads to a reduction in exergy factor caused by the reduced temperature at the outlet. In addition, the exergy factor increases as the particle loading are increased mainly due to the increased temperature at the outlet, as shown in Figures 28e & 28f. This shows that the particle loading needs to be increased to increase the system's thermal and exergetic efficiency. However, the increased particle loading may lead to deteriorating the particle egress through the aperture. Nevertheless, particle egress is not within the scope of this project. Future investigation is needed to optimise the design of the aperture size for the SEVR to obtain optical operation conditions in terms of high particle loading with minimal particle loading egress.





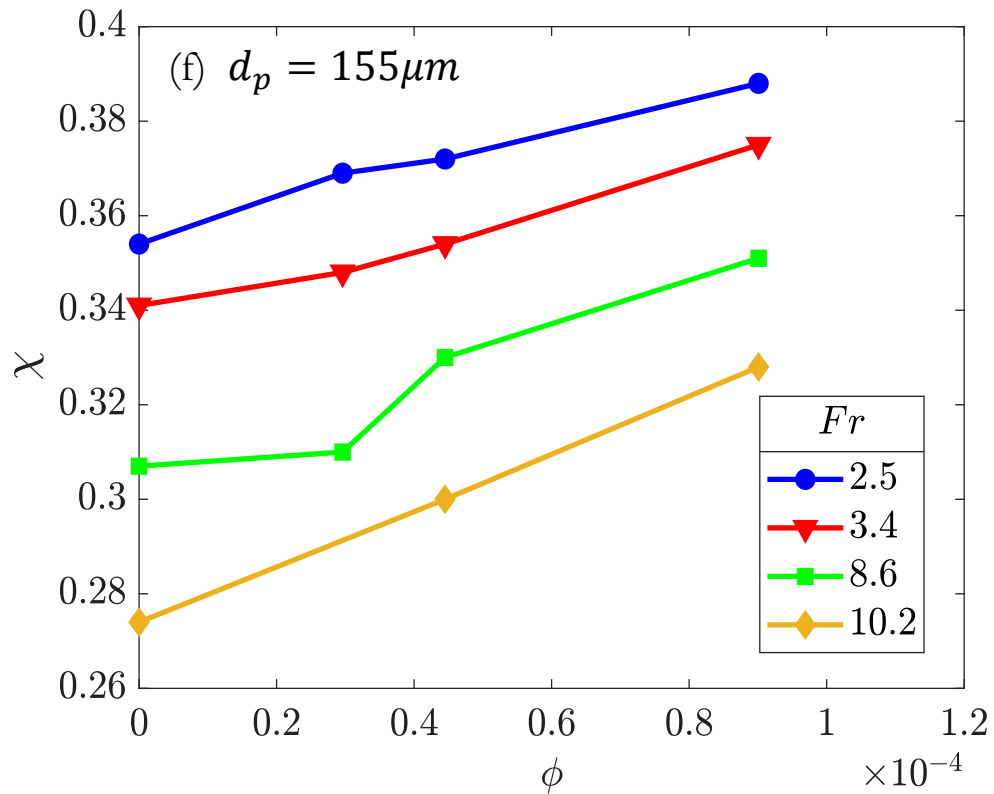
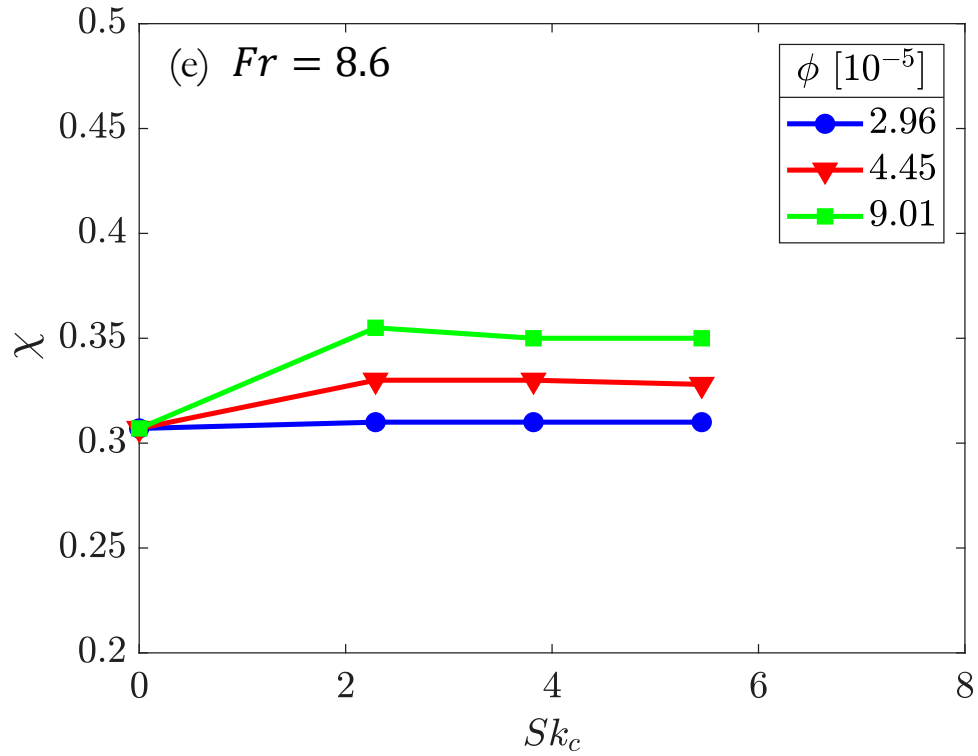


Figure 28. Measured thermal efficiency within the SEVR as a function of (a) Stokes number with different Froude number at a constant particle loading (b) particle loading with different Froude number at a constant particle size (c) Stokes number with different particle loading at a constant Froude number. Measured exergy factor within the SEVR as a function of (d) Stokes number with different Froude number at a constant particle loading (e) Stokes number with different particle loading at a constant Froude number (f) particle loading with different Froude number at a constant particle size.

#### **4.5 Two-phase study: Influence of key dimensionless parameters on the Fractional Convective, radiative heat losses**

Figures 29 and 30 show the fraction of radiative and convective heat losses through the aperture and the variation of Froude number ( $Fr$ ) and particle loading ( $\phi$ ) based on the experimental measurements. The dependency of Stokes number was not included as it does not present any significant difference for both radiative and convective heat loss terms. Similarly, the variation of operating parameters has very little influence on the conduction heat loss mechanism for this lab scale SEVR. This can be explained as the reactor has been well insulated, resulting in nearly consistent conduction losses across all cases. Moreover, the fraction of the conductive heat loss in the current laboratory-scale SEVR is expected to be relatively higher than an industrial scale SEVR because of the greater volume to surface area ratio of the device (e.g., the surface area to volume ratio for the current SEVR is 23.80, for the 50 MW scaled-up receiver, the estimated surface area to volume ratio is approximately 0.625). It is expected that as the device is being scaled-up, the conductive heat loss has a minor effect as the fraction of heat loss from conduction would be significantly diminished due to the reduction of surface area to volume ratio in the reactor.

Figures 29 a-b shows the effects of Froude number on the fractions of radiative and convective heat losses through the aperture. The radiative heat loss reduces when the Froude number is increased. At a lower Froude number, it is estimated that radiation loss through the aperture is large, namely, because more particles are suspended along the centreline being exposed directly to solar irradiation. In addition, the particle temperature is higher for lower Froude number cases as more particles are exposed towards the centreline region despite a longer particle residence time, which increases the radiation loss through the aperture. Hence, these particles are expected to reradiate the heat through the aperture allowing more radiant heat to be lost.

Meanwhile, under the cyclonic regime, the particles are centrifuged closely to the receiver wall. The absence of particles on the centreline region allows greater penetration of radiation to the inner region of the device, which lessens the radiative losses through the aperture as the majority of the radiant energy has been absorbed by both the wall and two-phase flow; thereby, reducing the reradiation heat loss by particles in the centreline region. On top of that, the increase of the Froude number leads to a lower wall temperature, therefore reducing the radiative heat loss through the aperture as most of the radiative heat losses originated from the

receiver wall. The convective heat losses shown in Figure 29a through the aperture is increased due to the reduced temperature at the outlet section. It can also be seen that when the inlet velocity is increased, air exchange through the aperture also increases, the same as observed in the single-phase flow-field study [37], which results in more significant convective heat loss through the aperture as ambient cold air is being mixed with the hot air in the reactor.

Figure 30 shows the effects of particle loading on the heat transfer within the receiver. As shown in Figure 30a, the particle loading is increased, the reradiating losses through the aperture are reduced. This is because the higher loading of particles captures more radiant energy from the solar flux (i.e., The increase of particle mass flowrate increases the heat capacity of the mixture of gas and particles). Similarly, the particle temperature is lower for higher particle loading, reducing the radiative heat losses through the aperture. As shown in Figure 30b, the convective heat losses are reduced as the particles absorb the energy due to the longer particle residence time when particle loading is increased. Overall, the convective heat loss is greater than the radiative heat loss, as the current outlet temperature of the receiver is at a lower level (300 °C ~ 450 °C). However, the trend is expected to vary when temperature within the receiver is further elevated, eventually allowing radiative heat loss to dominate over convection losses. This is mainly because radiative heat losses increase non-linearly with temperature (i.e., given that temperature has a power of fourth order in radiation loss).

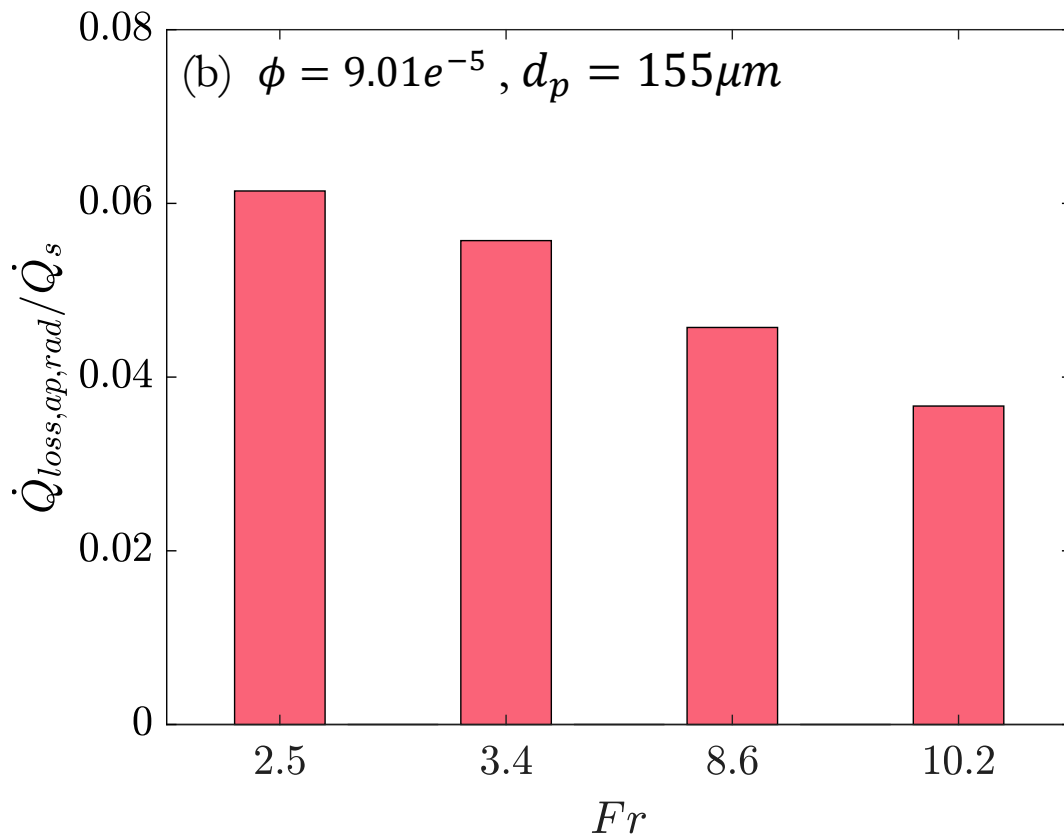
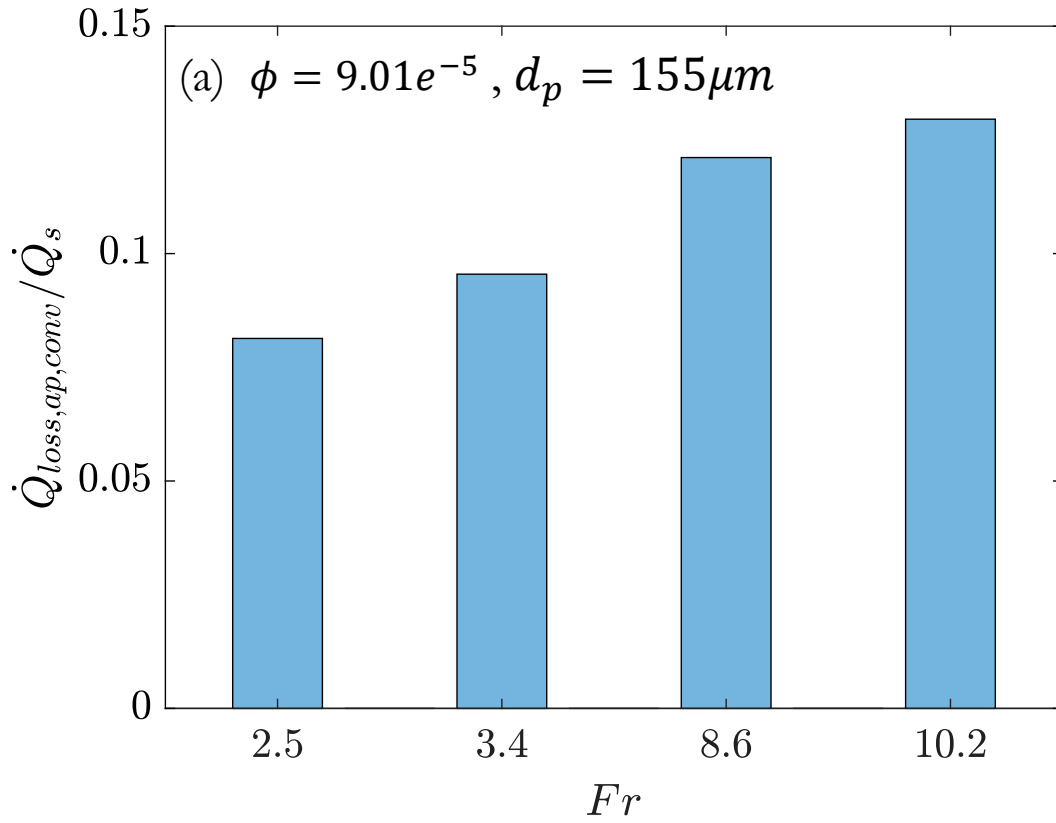


Figure 29. (a) Measured radiative heat loss through the aperture for different Froude number at a given particle loading and size. (b) Measured convective heat loss through the aperture for different Froude number at a given particle loading and size.

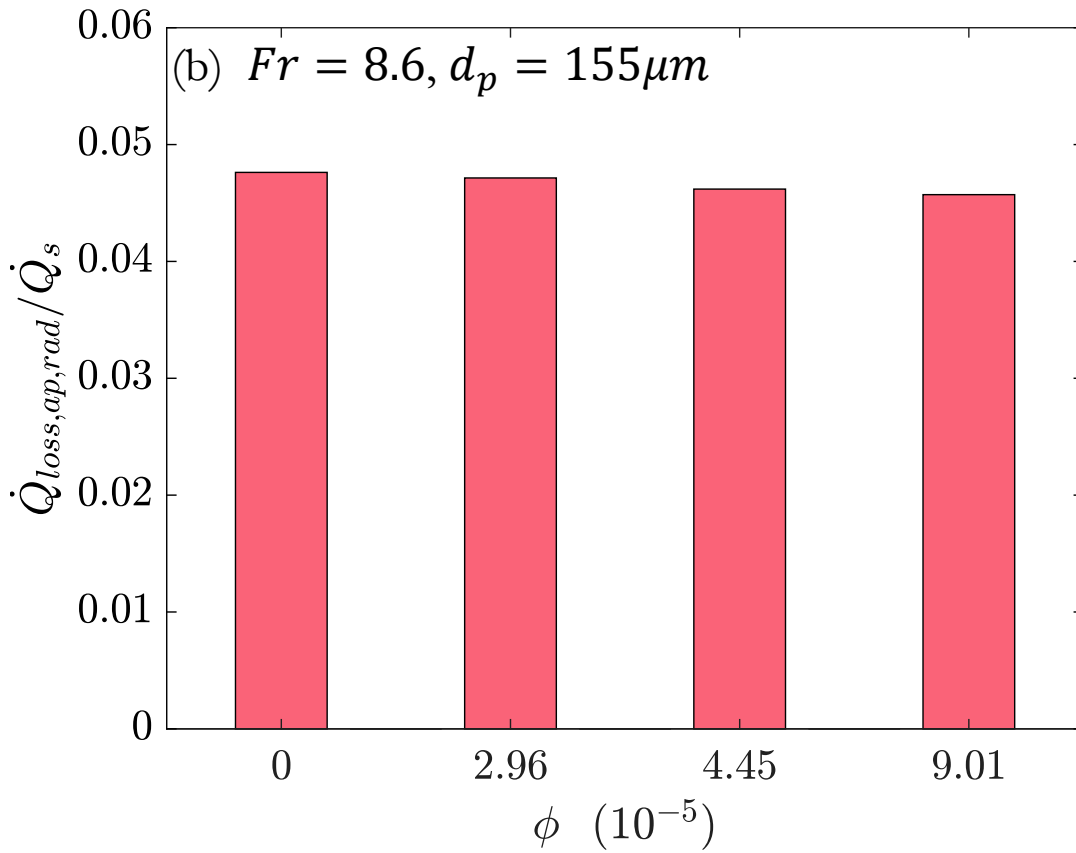
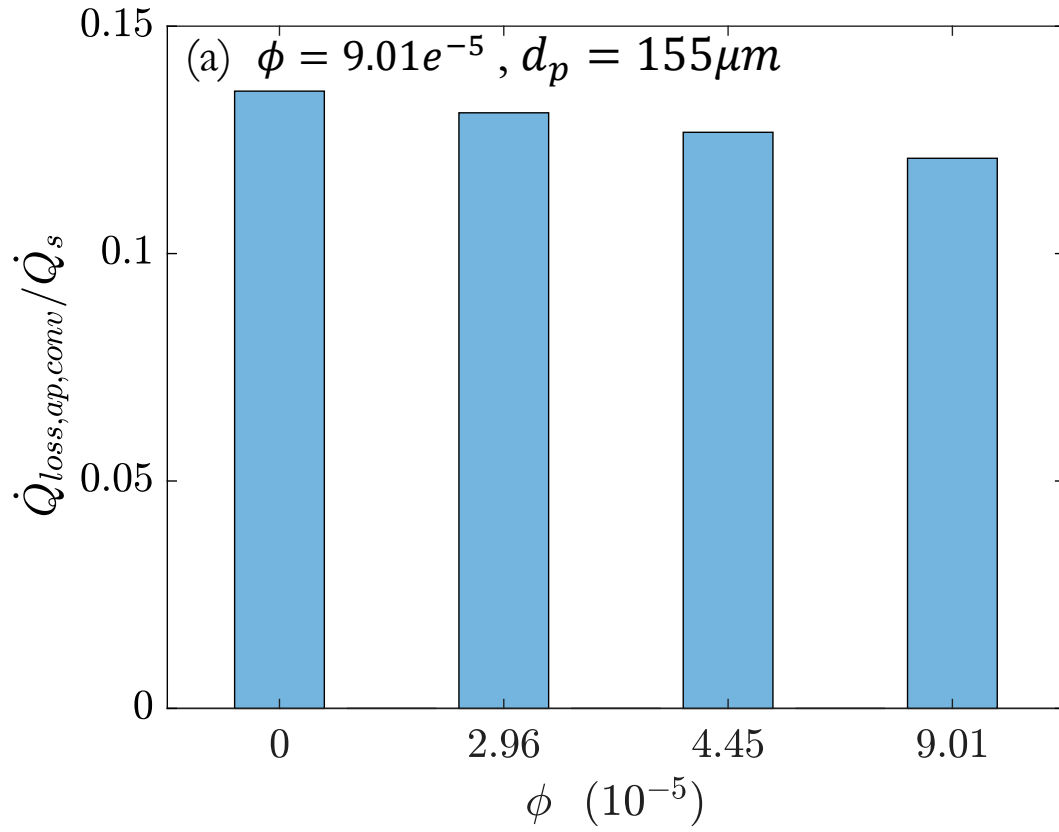


Figure 30. (a) Measured fractional radiative heat loss through the aperture different particle loading at a given particle loading and particle size. (b) Measured fractional convective heat loss through the aperture different particle loading at a given Froude number and particle size.



## 4.6 Two-phase study: Influence of key dimensionless inflow parameters on enthalpy ratio

Figure 31a presents the dependence of the ratio of the gas phase enthalpy to the particle phase enthalpy,  $\Delta H_{a-p}$ , on Stokes number for four different values of Froude number under a fixed particle loading of  $\phi = 4.45e - 05$ . The inlet Froude number is an insignificant factor for the enthalpy ratio at the outlet and is basically independent of the Stokes number. From the experimental measurements, the amount of heat absorbed by the gas phase is around 9.17 – 10.66 times of the solid phase as calculated using Equation (3.15), while the numerical result displays a similar trend with the heat absorbed of 7.43 – 9.01 times of the solid phase. This is because the particles absorb the radiant heat directly, which causes the particle temperature to rise more rapidly than the gas phase. Consecutively, part of the absorbed heat on the particle is transferred to the air via convection. This explanation can be verified by the temperature difference between the particles and the air at the outlet, discussed in Section 5.1.

Figure 31b presents the dependence of  $\Delta H_{a-p}$  on the Stokes number for three different values of particle loading under a fixed Froude number ( $Fr = 8.6$ ). It is interesting to note that  $\Delta H_{a-p}$  is heavily dominated by the particle loading under a constant solar energy input. As the particle loading increases, the enthalpy ratio between the two phases increases, and vice versa. This is because that more fraction of energy will be absorbed by the solid phase under a higher loading.

Figures 32a & 32b present the enthalpy ratio on the air-to-particle loading as a function of Stokes number, the Froude number and particle loading collapse well with the enthalpy ratio. This shows that the system's enthalpy ratio depends on the particle loading, while Stokes number has a secondary influence on the thermal performance. It is observed that most of the ratios between the normalised enthalpy of two phases have values less than and close to unity. This demonstrates that more heat is being transferred to the gas phase than to the particle phase. Eventually, increasing the particle mass under a fixed flowrate of the gas phase would result in an increased difference in this ratio, and potentially, the particle phase would potentially absorb more energy through radiation. The current configuration of this reactor is suitable for industrial application, but not limited to, reacting flow and air heating applications due to its ability to heat up air and particles consistently.

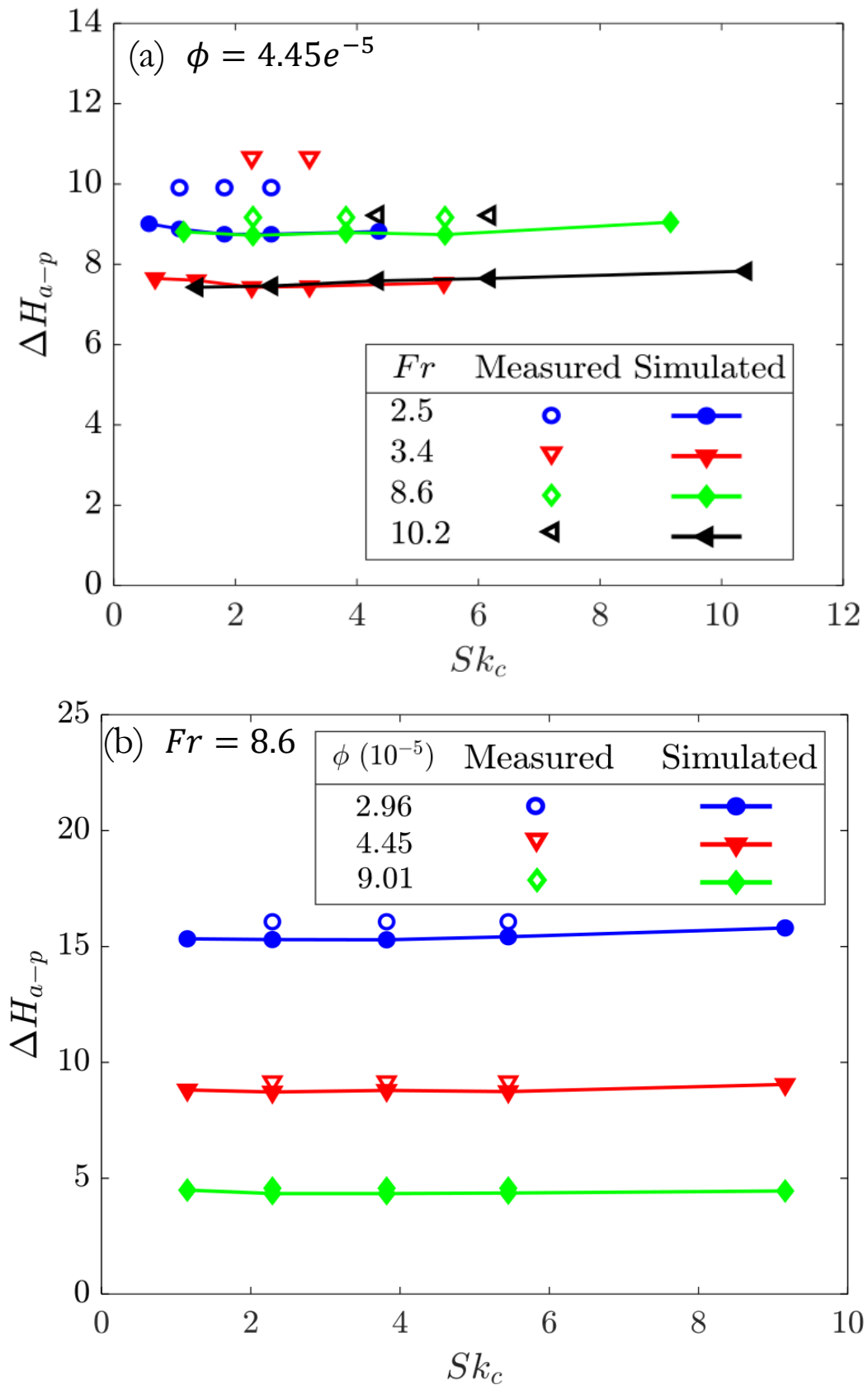


Figure 31. Calculated values from experimental and numerical study of the enthalpy ratio as a function of Stokes number with various (a) Froude number for a fixed particle loading. (b) Particle loading for a fixed Froude number.

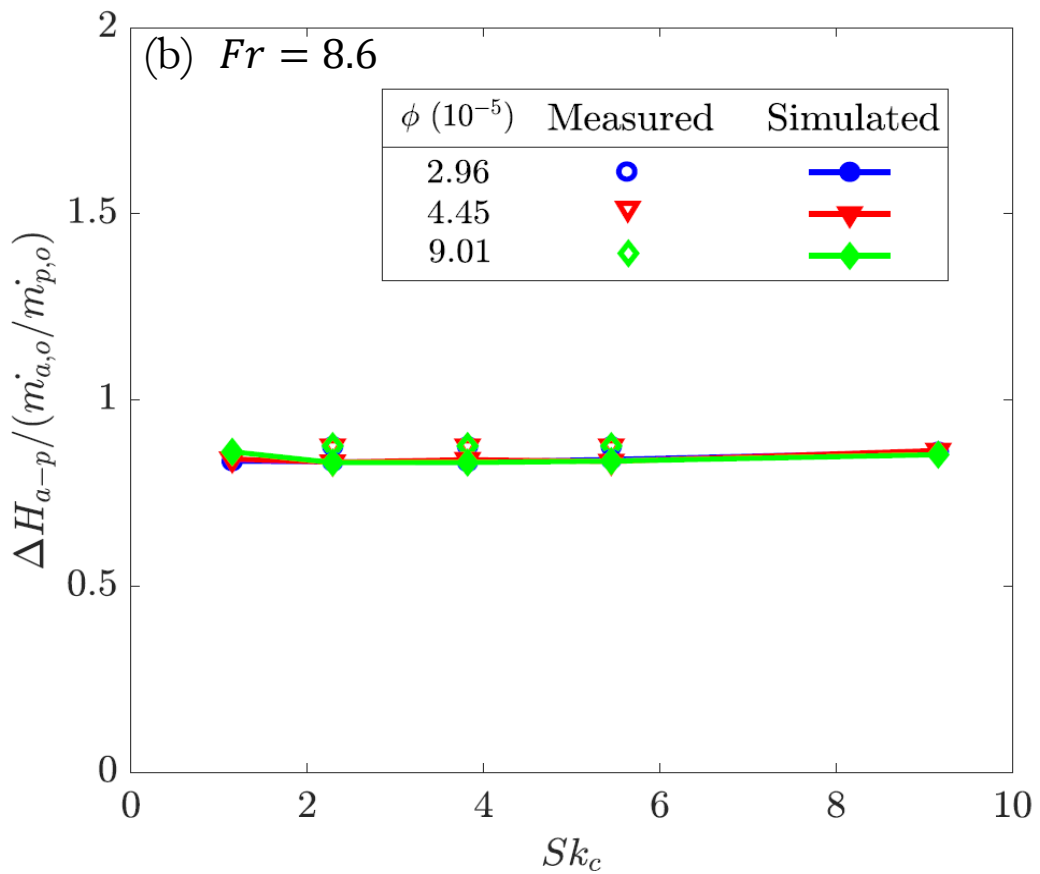
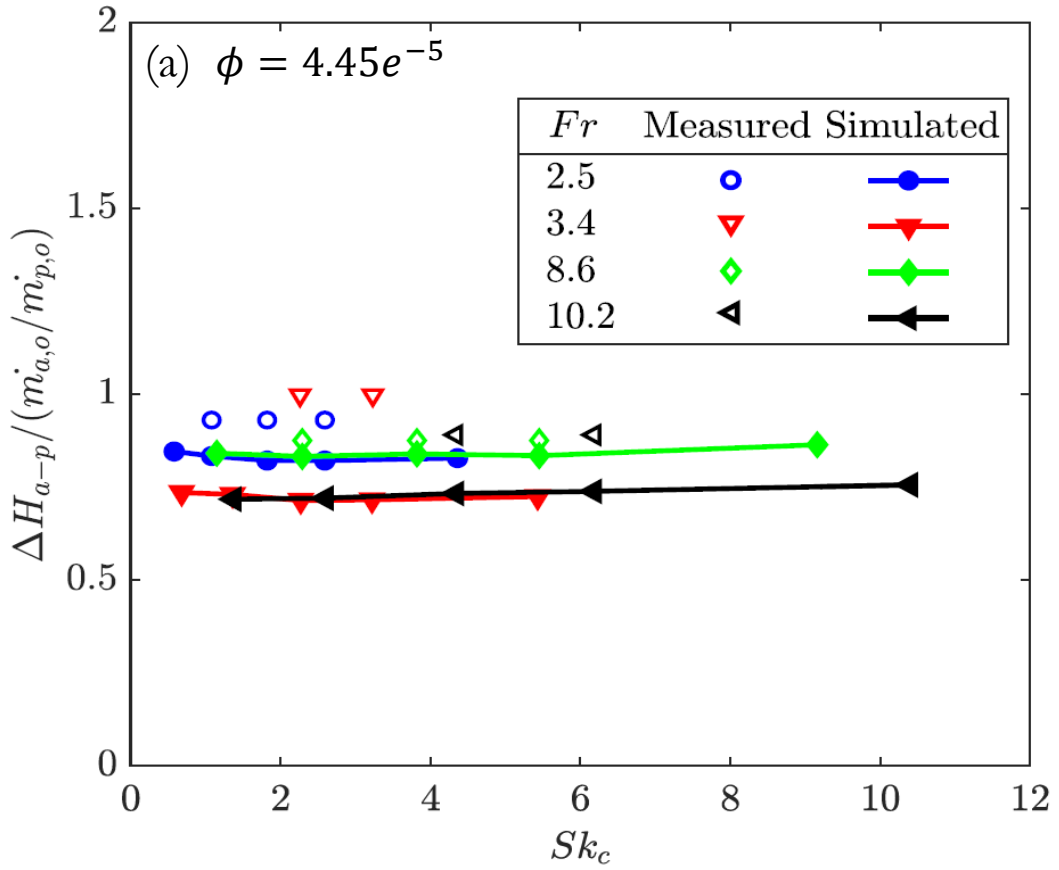


Figure 32. Calculated values from experimental and numerical study of the enthalpy ratio normalised by gas/particle mass loading ratio as a function of Stokes number with various (a) Froude number for a fixed particle loading. (b) Particle loading for a fixed Froude number.

## Chapter 5 Numerical study on the thermal performance

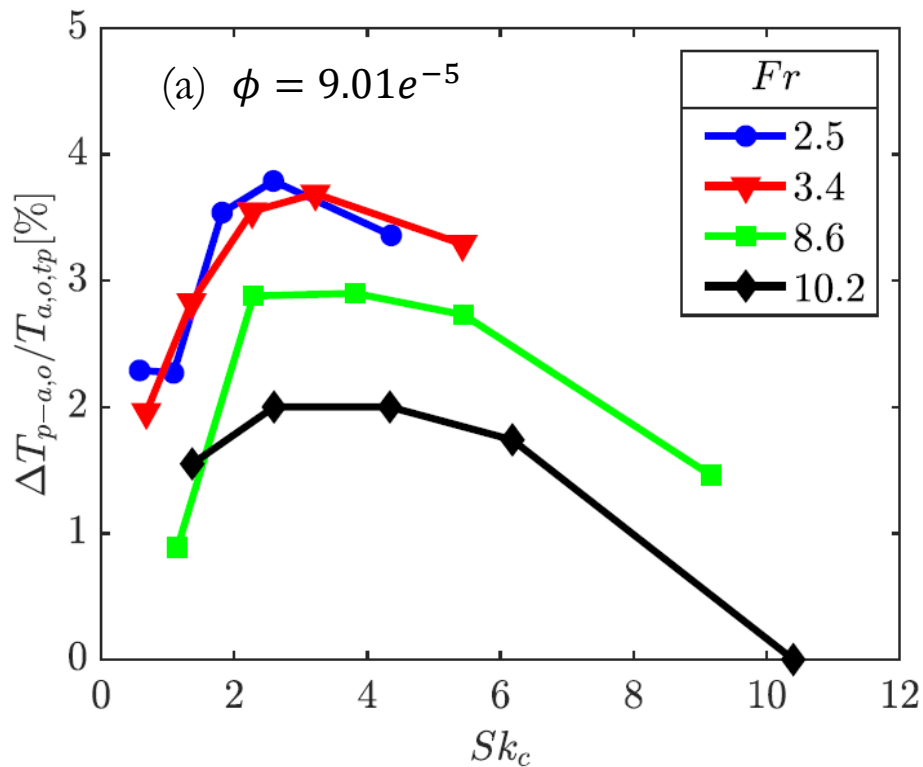
In this chapter, a numerical investigation is conducted to assess the influence of several dimensionless parameters on the thermal performance of the SEVR. This study aims to understand the fraction of thermal energy absorbed in the gas and particle phases within the reactor. In addition, the combined effects between the two distinctive flow regimes (i.e., Froude-Stokes and cyclonic regimes), particle residence time and distribution on the thermal performance of the reactor will be addressed.

### 5.1 Effects on outlet temperature

CFD has been employed to estimate the temperature difference between the two-phases particularly at the outlet. The validation of the outlet air temperature is within the acceptable range, as shown in Section 3.5. Figure 33 presents the temperature difference between two-phases with respect to Stokes number. Figure 33a shows the effects of Froude and Stokes number on  $\Delta T_{a-p,o} / \Delta T_{a,o,tp}$  that is the ratio of  $\Delta T_{a-p,o}$  (temperature difference between the particle phase and the air phase at the outlet) to  $\Delta T_{a,o,tp}$  (outlet temperature of the two-phase mixture) for a fixed particle loading,  $\phi = 9.01e - 05$ . The values of  $\Delta T_{a-p,o} / \Delta T_{a,o,tp}$  indicate the intensity of the difference between the temperature of the particle phase and the temperature of the local air around the particles. Figure 33b presents the effects of particle loading and Stokes number on  $\Delta T_{a-p,o} / \Delta T_{a,o,tp}$  for  $Fr = 8.6$ . Figures 33a and 33b show that the particle phase temperature is slightly higher than that of the gas phase, i.e.  $\Delta T_{a-p,o} / \Delta T_{a,o,tp}$  is about 0.9 ~ 4.0 %. This has confirmed that the particle and gas phase are nearly in thermal equilibrium at the outlet of this SEVR device under the investigated conditions and that the minimal difference between the two-phases was said to have minor effects on overall heating processes in most applications. Therefore, it is valid to assume that the gas and particle phases are of thermal equilibrium despite the minor differences. From Figure 33a, it can be seen that under the Froude-Stokes regime ( $Fr < 4$ ), the particle temperature difference tends to collapse closely even the Stokes number is increased, whereas, under the cyclonic regime ( $Fr > 4$ ), the temperature difference is reduced as the Froude number increases. This implies that the temperature difference is uniform under the Froude-Stokes regime showing that particles are relatively uniformly heated under this regime while being arbitrary in the cyclonic regime. It is mainly dominated by the nominal residence time of the reactor. Please recall that particle concentration distribution in the entire SEVR is more uniform in the Froude-Stokes regime than that of the cyclonic regime. As shown in Figure 33b, it can also be concluded that the temperature difference between two-

phases with various mass loading is consistent as observed with most cases ( $Sk_c > 2$ ), which shows that the particle temperature difference in the device is not significantly affected by the particle loading when the Stokes number is large. Hence, the temperature difference as a function of Stokes number is independent of the particle loading.

Figure 33c presents the temperature difference between the gas phase and the particle phase at the outlet with varying particle loading and Froude number. A clear trend can be seen for the particle loading under the Froude-Stokes regime (i.e., the temperature difference is greater with lower particle loading while lower at a higher loading). This is expected as the increased number of particles increases the radiative to be converted into convective heat for the gas phase under uniform mixing, thus, reducing the temperature difference between the two phases. As for the cyclonic regime, the particles are less exposed to the direct irradiation than in the Froude-Stokes regime due to the flow inertia, which reduced the radiant heat absorbed by the particles. Consequently, a higher particle loading allows for a greater temperature difference as the swirl intensity within the flow is further reduced. The reduction of swirl intensity allows for a greater residence time for the particles to be exposed to solar radiation. Given that the percentage difference between the particles and gas phase is minimal, it can be concluded that the effect of particle loading on the two-phase temperature difference is insignificant, which is consistent with Figure 33b.



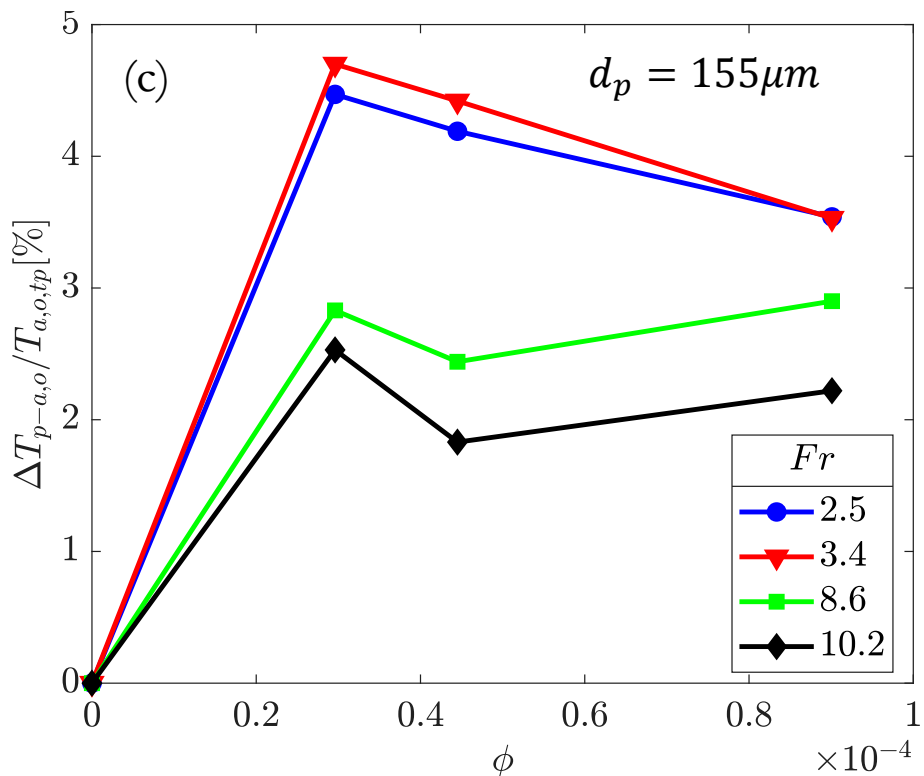
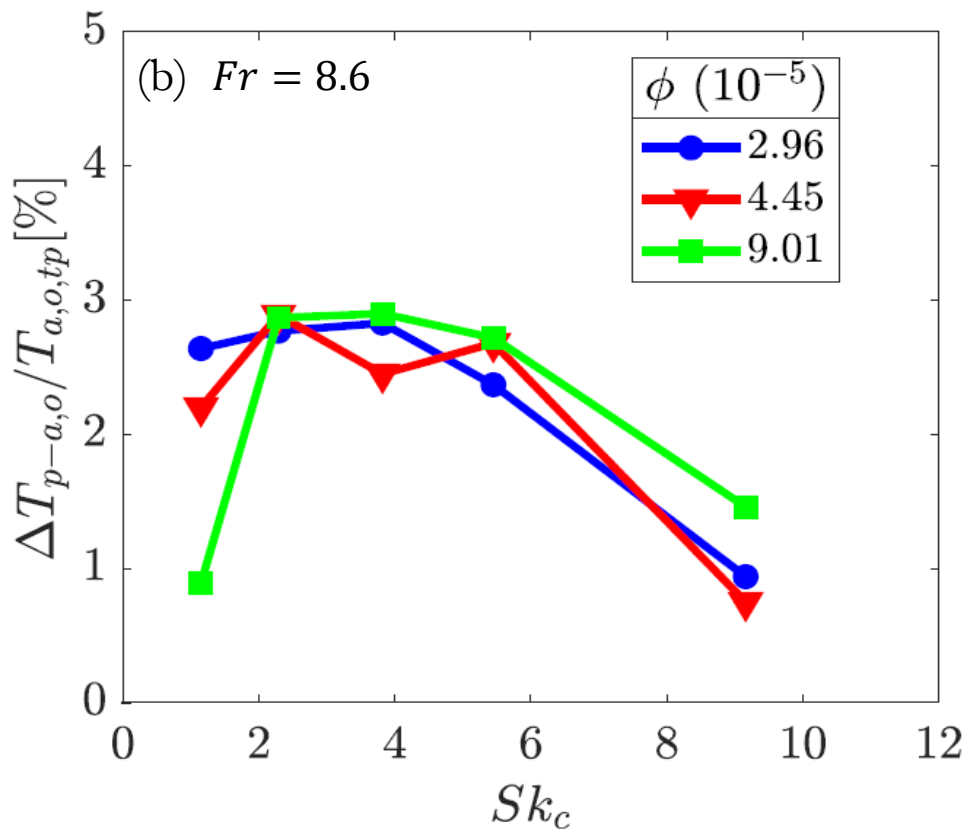
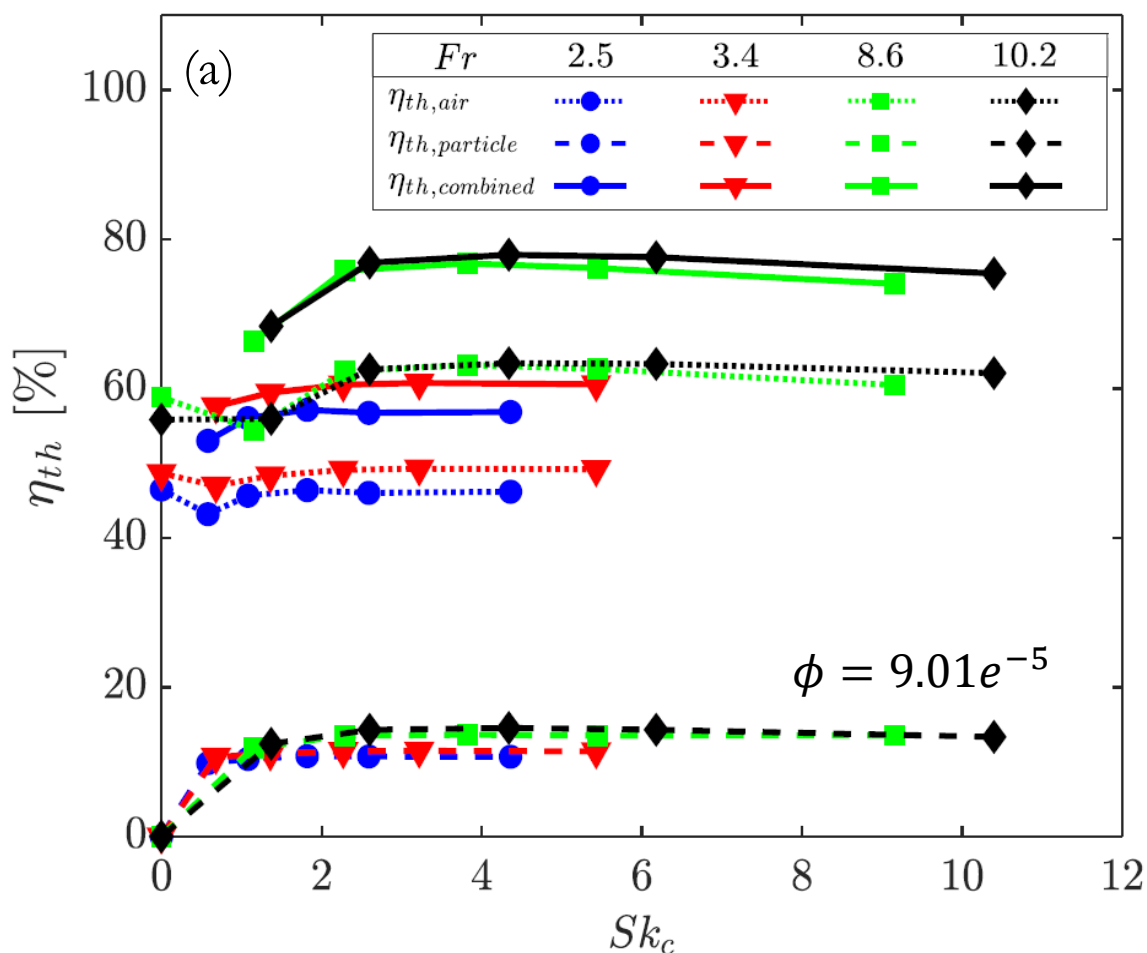


Figure 33. Calculated percentage difference between air and particle temperature on (a) Stokes number as a function of Froude number with constant particle loading. (b) Stokes number as a function of Particle loading with constant Froude number. (c) particle loading as a function of Froude number with constant particle size.

## 5.2 Effects on thermal efficiency

Figure 34a shows the overall thermal efficiency of the SEVR based on simulation results. It is important to note that this is different from the experimental results, the efficiency of the simulation result shown here is calculated using the temperature of the particle phase and the temperature of the gas phase separately as demonstrated in Equations 3.13 and 3.14, alongside with the combined thermal efficiency for the two-phases as shown in Equation 3.12. It is interesting to note that the gas phase has nearly 4-8 times greater efficiency than the particle phase. It is also observed that increasing the Stokes number would lead to a slight decrement of efficiency. Since the Stokes number has minimal effects on thermal efficiency, it can be said that the trend of thermal efficiency is not affected by the Stokes number. As shown in Figure 34b, it is also interesting to note that the gas phase efficiency is similar across all Stokes numbers, while the particle efficiency increases with the loading; this demonstrates that, under a fixed inlet velocity, the overall thermal efficiency of the device is only influenced by the particle loading. Hence, the greater significance of particle loading was found to affect the thermal efficiency of the SEVR.



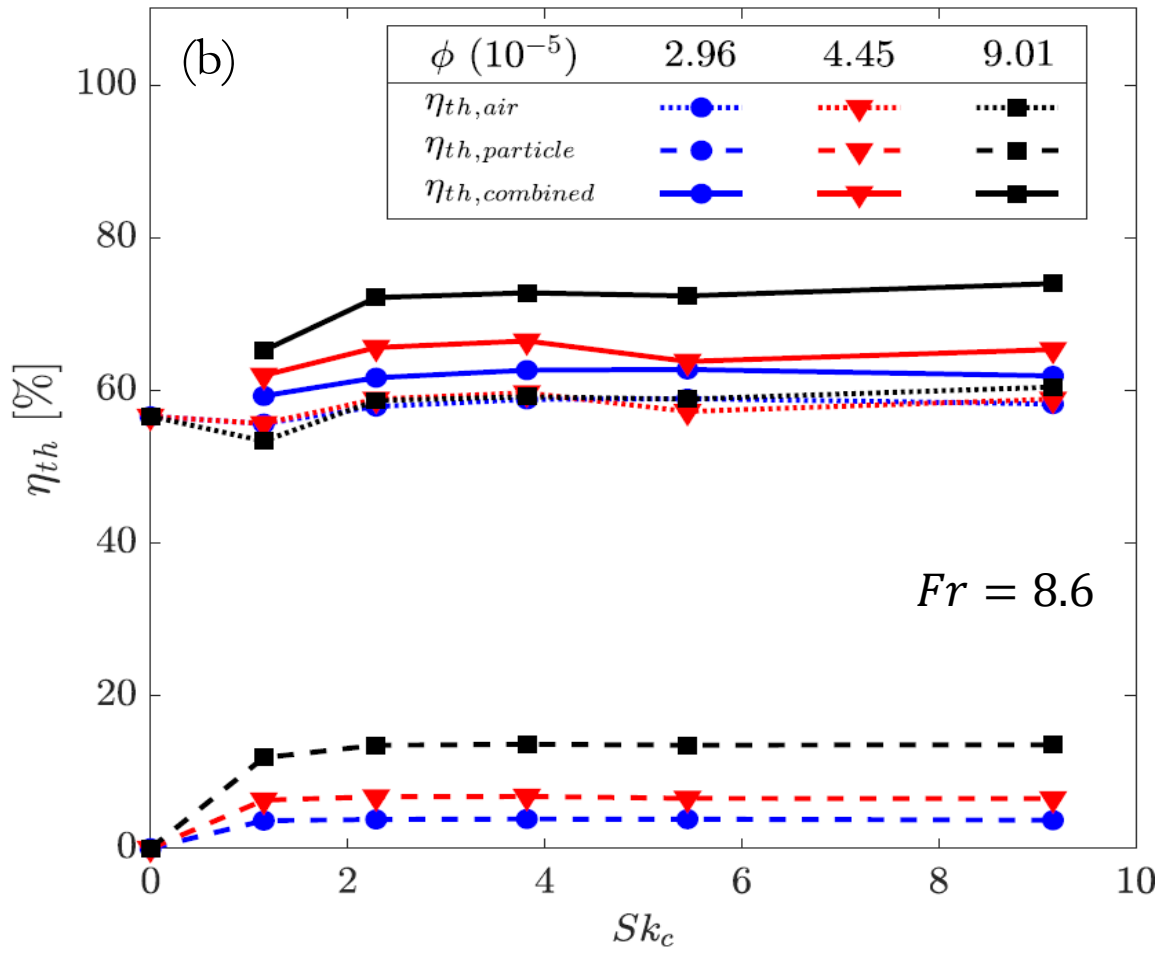


Figure 34. Simulated thermal efficiency within the SEVR as a function of Stokes number with (a) different Froude numbers at a constant particle loading (b) different particle loadings at a constant Froude number. (i.e., calculated with Equations 3.12 – 3.14)



### 5.3 Temperature and particle distribution within the SEVR

Figure 35 illustrates the simulated temperature profiles and particle volume concentration within the SEVR. Both temperatures and particle volume concentration are probed using the centreline evolution function in the CFD. Under the Froude-Stokes regime ( $Fr < 4$ ), as shown in Figure 35a, it can be seen that the temperature of the particle phase is greater than that of the gas phase in the centreline. This is because the solid absorbs more energy when they are directly exposed to the incoming radiant energy. It is important to note that fewer particles (lower particle volume concentration,  $\psi$ ) are located at the centreline region, while the air and particle temperature at the mid and near-wall regions are almost in equilibrium. It is expected that the gas phase temperature to be near uniformly distributed with other radial regions due to flow recirculation. The particle volume concentration at the mid and near-wall region ( $r/R = 0.5, 0.75$ ) is similar as the particles are uniformly distributed under the Froude-Stokes regime. Under the cyclonic regime ( $Fr > 4$ ) shown in Figure 35b, it can be seen that the temperature of particles at the centreline and mid-wall region are slightly lower than the gas phase; this may be attributed to the shorter nominal reactor residence time as well as the low particle volume concentration at these regions. Meanwhile, at the near-wall region demonstrates that the temperature between both phases is almost equilibrium, while most of the particles flow close to the wall due to the strong inertia of the vortex flow.

Figures 36 – 38 present the inlet particle volume concentration and temperature distribution within the SEVR. Cross-sectional planar cuts were performed at both radial ( $z/L = 0.25, 0.7, 0.9$ ) and axial ( $r/Dc = 0$ ) planes. With comparison to both Froude numbers in Figures 36 & 37, the lower Froude number (i.e.,  $Fr = 2.5$ ) contour plot shows that the particle concentration is more uniformly distributed across the device, whereas the particle concentration is less uniform under high Froude number (i.e.,  $Fr = 10.2$ ). This implies that the lower Froude number allows better mixing of the fluid within the SEVR. This is due to the stronger intensity of recirculation dominated by buoyancy effects along the centreline. In contrast, the higher Froude number results in the inertial force being dominant relative to the gravitational force, resulting in a higher fluid concentration at near-wall regions. As for the temperature contour shown in Figure 38, the lower Froude number case results in a more uniformly distributed temperature within the device due to flow recirculating in the centre, while a higher Froude number results in a cooler temperature at the centre region as the particles are more concentrated towards the near-wall region.

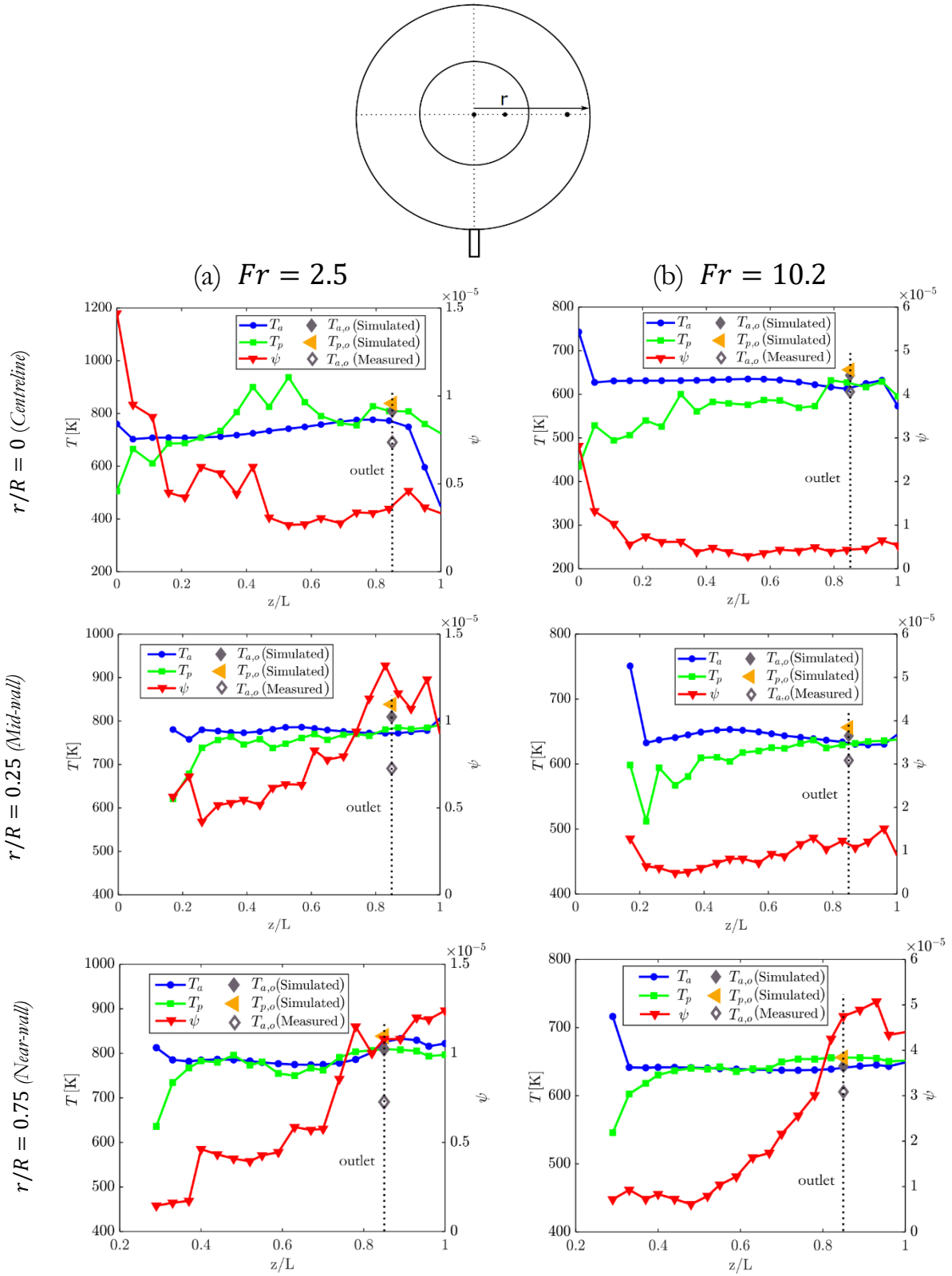


Figure 35: Calculated air and Particle Temperature along with particle concentration within the SEVR under a fixed particle size of  $155\mu\text{m}$  and particle loading, under the (a) Froude-Stokes and (b) cyclonic regime.

$$Fr = 2.5, d_p = 155 \mu\text{m}$$

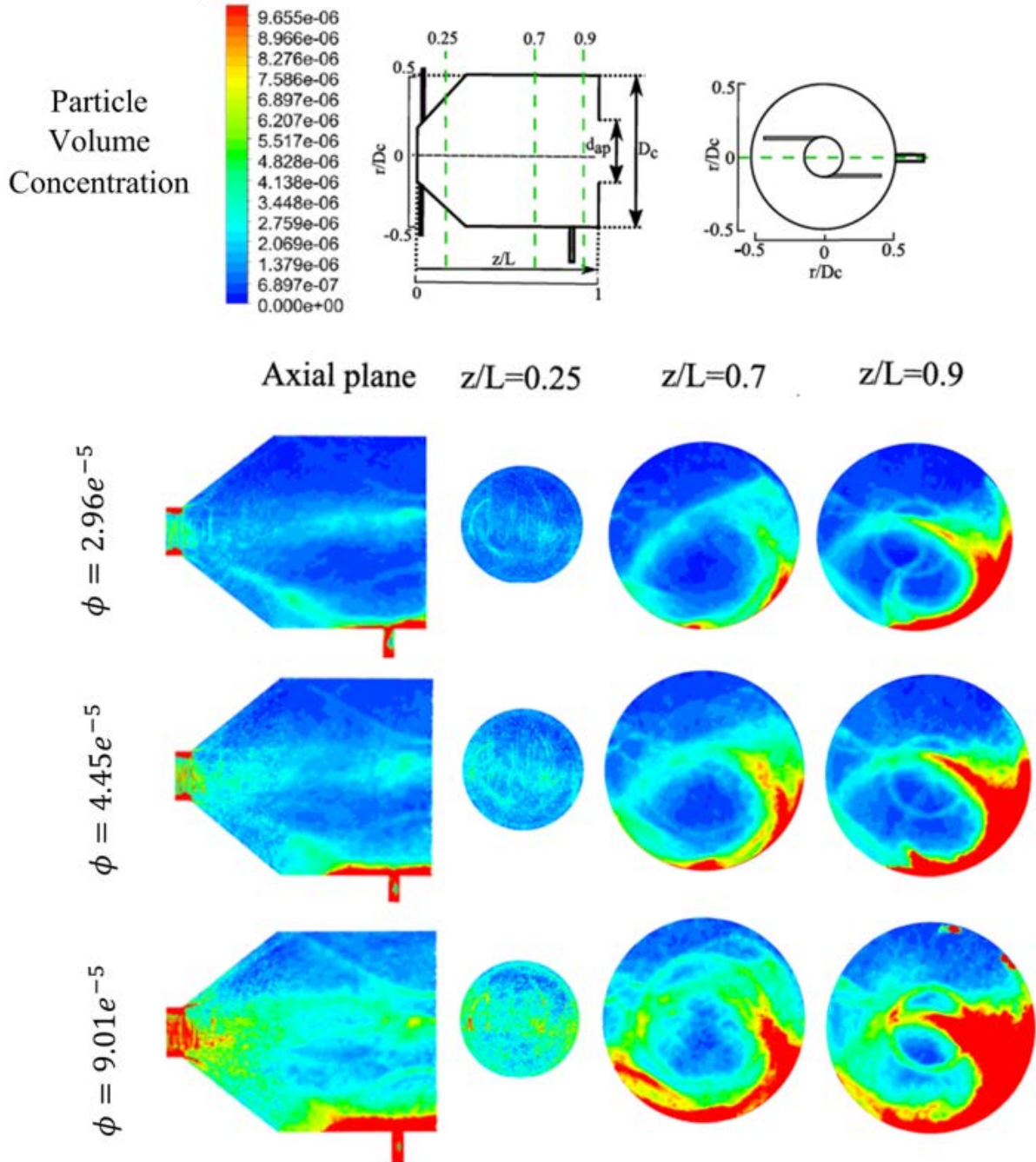


Figure 36. Representative maps estimated for the particle volume concentration across different radial and axial planes within the SEVR under the Froude-Stokes regime ( $Fr < 4$ ) with a constant particle size.

$$Fr = 10.2, d_p = 155 \mu m$$

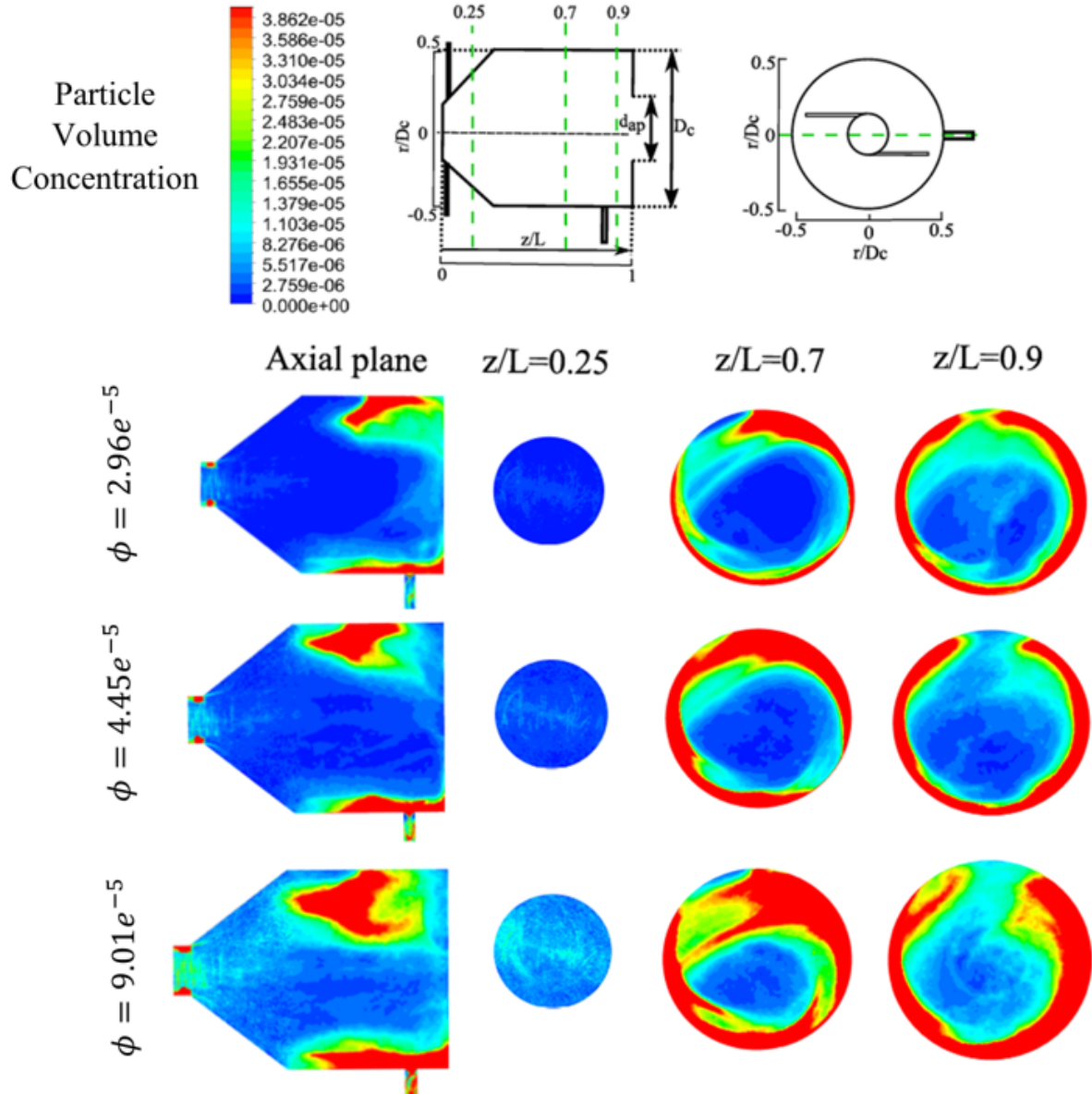
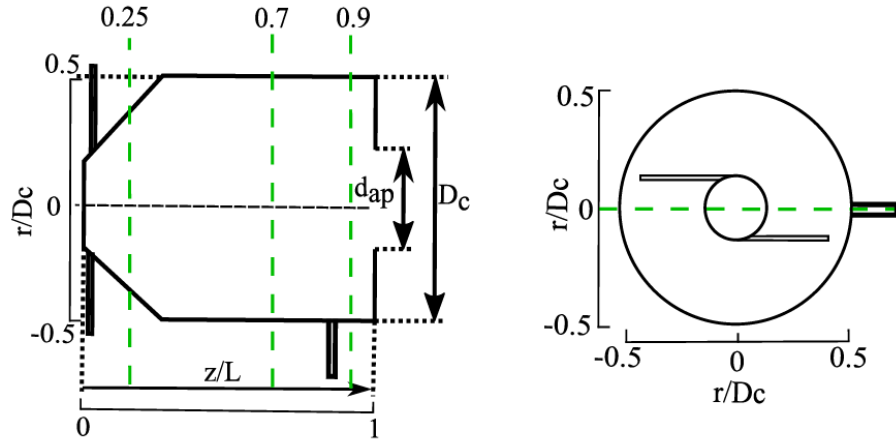
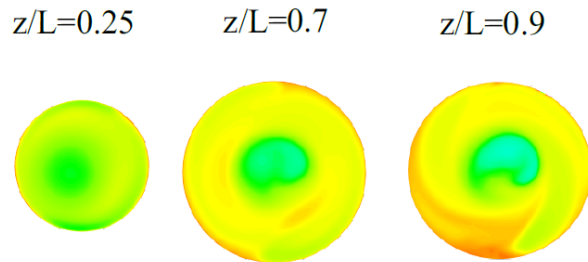
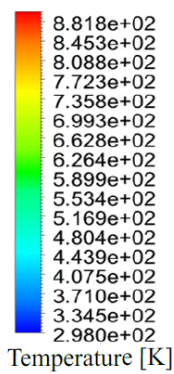


Figure 37. Representative maps estimated for the particle volume concentration across different radial and axial planes within the SEVR under the cyclonic regime ( $Fr > 4$ ) with a constant particle size.

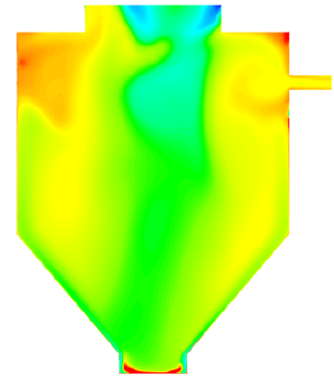
$$\phi = 9.01e^{-5}, d_p = 155 \mu m$$



(a)  $Fr = 2.5$



Axial Plane



(b)  $Fr = 10.2$

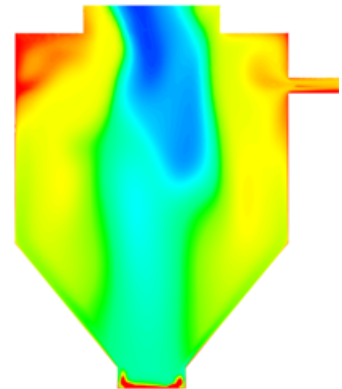
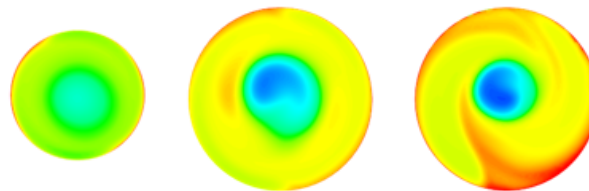
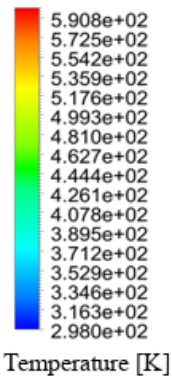


Figure 38. Representative maps estimated for the temperature distributions across different radial and axial planes within the SEVR under the (a) Froude-Stokes regime ( $Fr < 4$ ) and, (b) cyclonic regime ( $Fr > 4$ ) with a constant particle size.

## 5.4 Swirl number analysis

Figure 39 presents the effects of particle loading and Stokes number (i.e., particle size) on the swirl number within the SEVR. CFD has been employed to determine the swirl intensity of the flow within the receiver, which aims to provide additional data to understand the particle residence time distribution as well as to demonstrate the influence of Stokes number on the distribution of particles within the device. The overall trend of both Figure 39a & 39b shows us that the swirl intensity is only distinguishable at the conical section for different particle mass loading and different particle sizes. This implies that the impact of swirl intensity occurs at the conical region, where the flow undergoes momentum reduction due to the expansion of the geometry.

Data obtained from the numerical study, as shown in Figure 39a, shows that particle loading significantly influences the tangential momentum within the receiver. This has shown that an increase in particle loading will result in the reduction of swirl intensity, mainly due to the reduction of tangential velocity at the conical region. Hence, this implies that the particle residence time is lengthened, which is expected to reduce the temperature difference between the gas and particle phases.

As shown in Figure 39b, as the Stokes number increases, the swirl number also increases. This may be due to the different distribution of particles under different Stokes numbers (i.e., with different particle sizes). For small particle sizes ( $Sk_c = 0.5, 1.2$ ), the swirl intensity tends to be weakened at the conical region while large particles ( $Sk_c = 2.0, 2.7$ ) tends to have stronger swirl intensity as the mass of the larger particles is capable of maintaining the tangential momentum to the swirl intensity. Moreover, large particles will concentrate on the near-wall region, which will not affect the tangential velocity in the central region, while small particles are more uniformly distributed and, therefore, will reduce the high tangential velocity in the centre region.

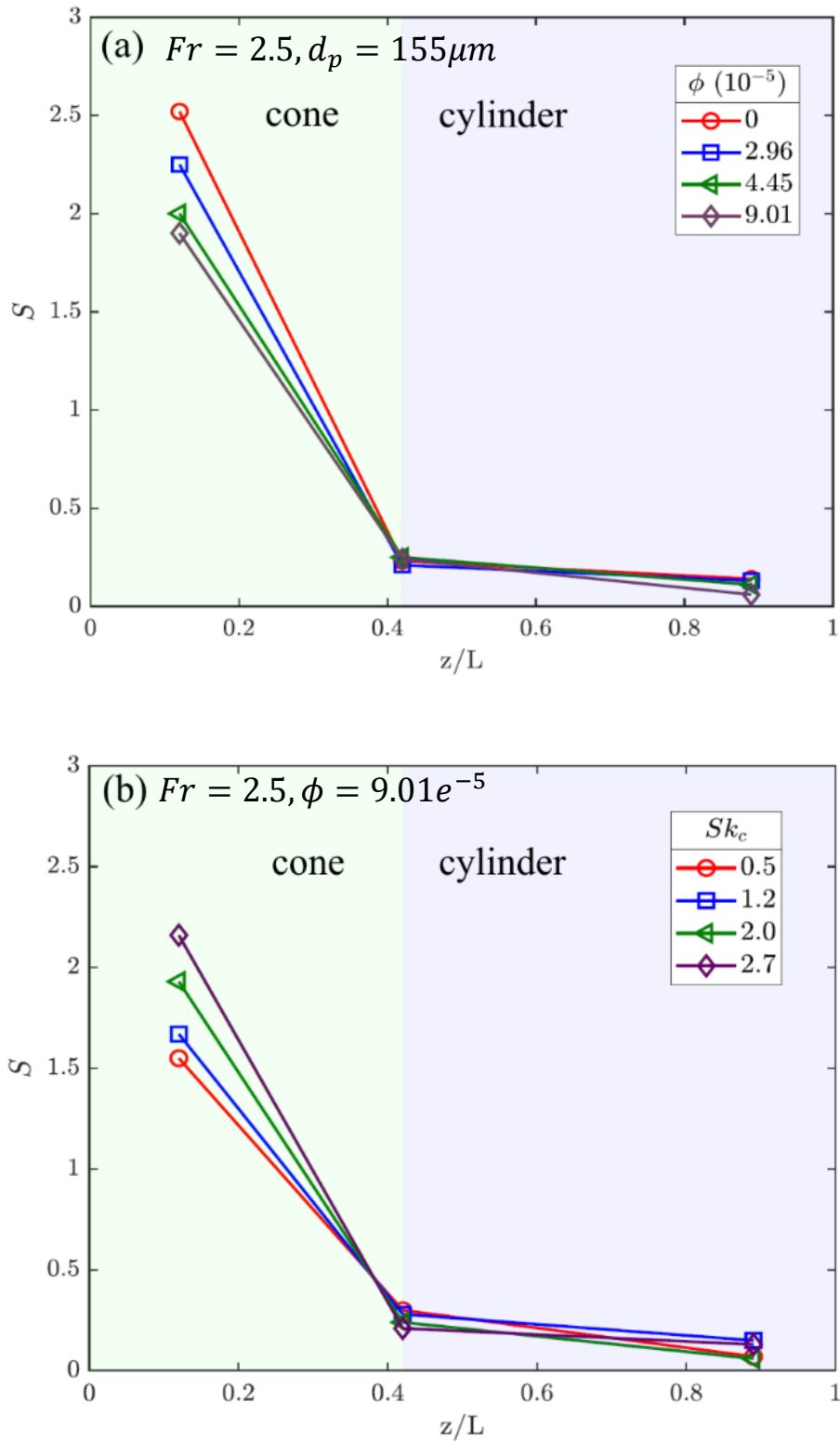


Figure 39. Simulated values of swirl number at positions ( $z/L = 0.18, 0.42, 0.89$ ) (a) particle loading with constant Froude number and particle size, (b) Stokes number (particle size) with constant particle loading and Froude number.

## 5.5 Normalised particle residence time

As shown in Figure 40a, at no tilt angle, the dimensionless residence time ( $\tau_p/\tau_{nom}$ ) increases because of increment of tangential velocity component in the flow, which can be attributed with the increase of particle inertia as Stokes number is increased. Under the Froude-Stokes regime ( $Fr < 4$ ), the particles generally take a shorter residence time than being under the cyclonic regime in the SEVR. This is because large particles exit the receiver faster than small particles as they are less likely to be recirculated, as shown in Figure 8a of Chapter 2. While in the cyclonic regime ( $Fr > 4$ ), the particles generally have a longer residence time than as particles under higher speed have a higher probability of hitting the inner wall of the SEVR and lose more momentum. The trend of effects of the Froude number on the normalised particle residence time is similar to the trend of the effects of Froude number on particle residence time in the isothermal case, as demonstrated in a previous study [40]. As shown in Figure 40b, when particle loading increases, the dimensionless residence time also increases. This is because the tangential velocity is reduced as more particles are introduced into the flow, as shown in the swirl intensity in Figure 40a, which shows a significantly reduced inertia to propel within the two-phase flow.



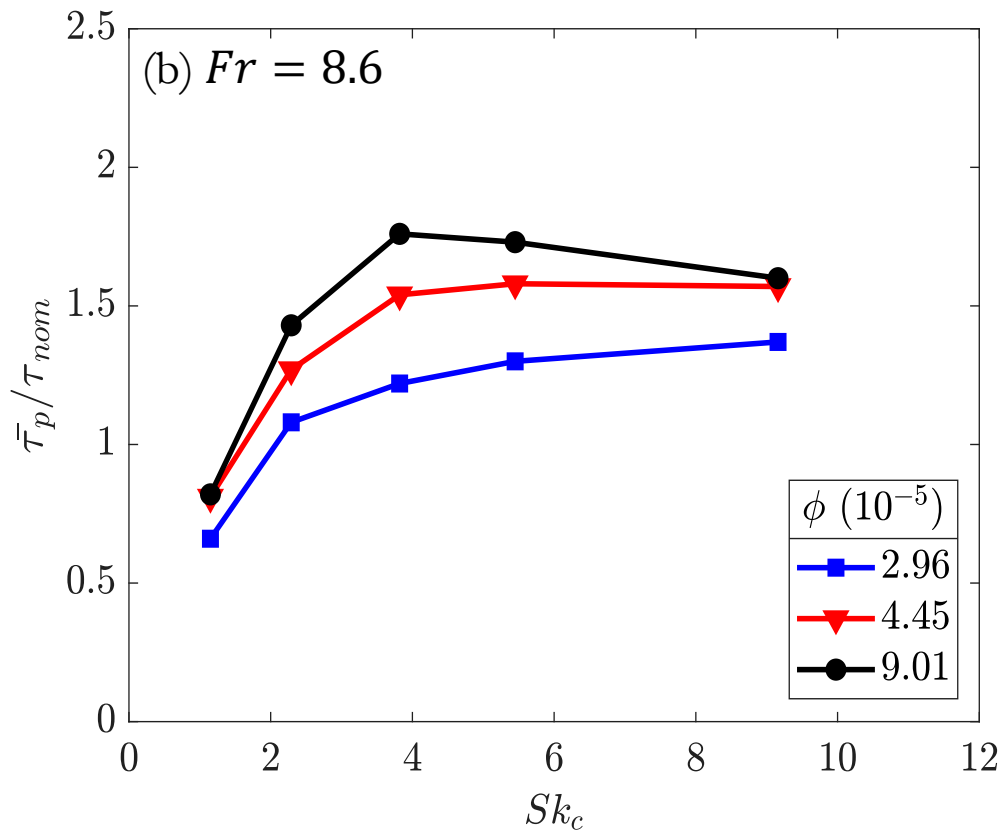
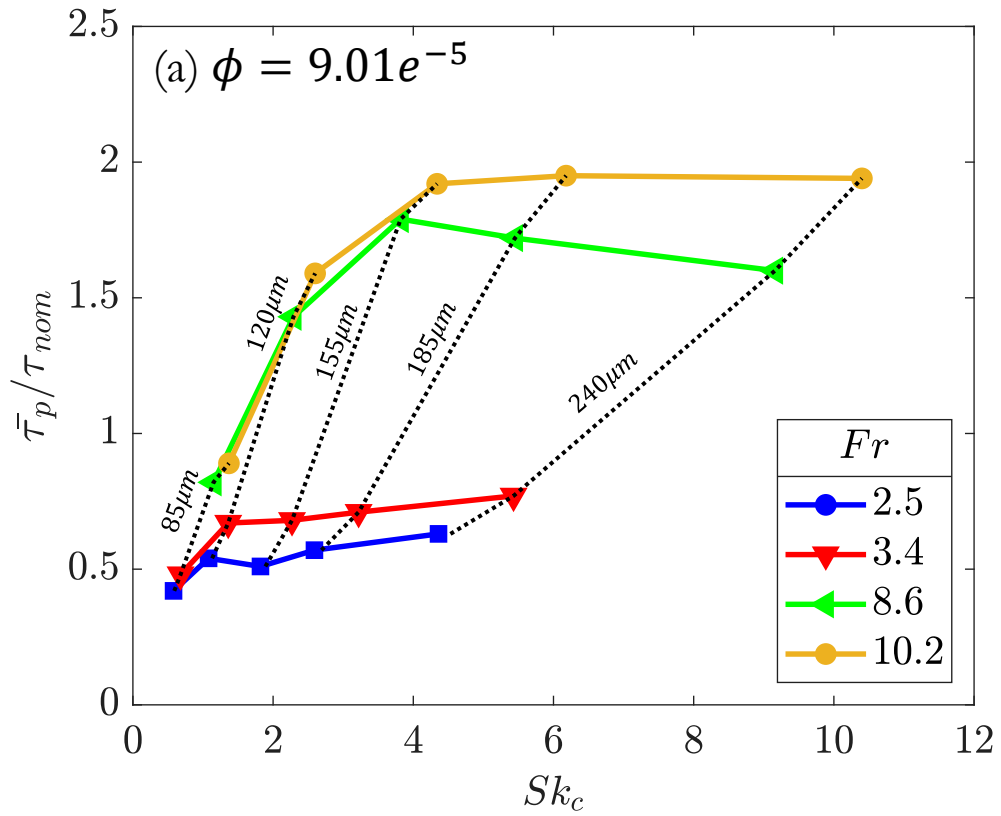


Figure 40. Simulated dimensionless particle residence time as a function of Stokes number within the SEVR as a function of (a) Froude number under a constant particle loading, (b) particle loading under a constant Froude number.

## Chapter 6 Conclusion and Future work

### 6.1 Conclusion

The key outcomes of the current study are as follows:

1. The ratio of total energy input to total heat capacity and intensity of overventilation has a significant influence on the thermal performance of the SEVR for both single- and two-phase flows. The amount of net air ingress should be reduced to a minimum of 15% to avoid exergy loss and decrement in thermal output while preventing particle egress effectively.
2. It is crucial to identify the trade-off between both energy and exergy efficiencies, which is required to allow the SEVR to operate at peak thermal efficiency to prevent useful energy (exergy) from being wasted.
3. The presence of particles was found to improve the thermal efficiency (i.e., with an increment on a range between 4% – 15%) and heat absorbed by the flow, which is beneficial in providing sufficient thermal energy for downstream processes such as gasification and calcination of raw minerals under suitable operation criteria.
4. The particle loading has a strong influence on the particle residence time and thermal efficiency of the SEVR. This is because the higher particle loading reduces the swirl intensity within the two-phase flow, which allow particles to dwell in the SEVR for more extended periods. In addition, the increment of particle loading leads to an increase in particle mass by energy balance, thus, increasing the overall thermal efficiency of the receiver.
5. Under the Froude-Stokes regime, the high concentration of particles at the centreline region coupled with the direct absorption of incoming radiation through the aperture and flow recirculation allows convective heat transfer in the reactor wall and particles to be more uniformly distributed. This is evident as the temperature distribution of the gas phase within the reactor is near equilibrium between the two-phases along the radial distance ( $r/R$ ). The flow recirculation contributes to the better mixing of particles and gas within the device. However, radiation losses are expected to be much higher than the cyclonic regime due to heat reradiated by the particles through the aperture.
6. In the cyclonic regime, the particles are centrifuged closely to the receiver wall, and the absence of particles on the centreline region allows better penetration of radiation to the back end of the SEVR as the flux profile is Gaussian distributed. This results in a lowered particle temperature at the centreline and mid-wall region because of the lower

particle concentration. In contrast, near-wall regions demonstrate that the temperature between the two-phases are almost of equilibrium since most particles are closer to the wall due to the strong inertia generated by the vortex flow.

7. The ratio of the normalised enthalpy between the two phases shows that more convective heat is being transferred from the particle to the gas phase. The mixing of two-phases shows that this is a benefit for an industrial reactor but not limited to potential applications in air heating and reacting flows. Even with the current scale, the two-phases are predicted to be near thermal equilibrium before exiting the SEVR. Hence, a preliminary hypothesis predicts that the SEVR can potentially operate as a particle heater.
8. The Froude number (i.e., flow velocity) significantly influences the convective heat loss through the SEVR aperture. As the Froude number increases, the rate of air exchanged at the aperture also increases. This is as expected because the flow recirculation that is increased with increased Froude number allows more hot air from within the cavity to egress through the aperture, while cold ambient air ingresses the device through back mixing from the recirculating flow, which increases the convective heat loss at the aperture plane.
9. The CFD results of the current lab-scale SEVR have predicted that the temperature difference between the two phases is small. However, it is expected that the temperature difference between the two phases would be more significant in a scaled-up device. This is mainly due to the increased reactor volume allows greater radiant heat absorption and residence time for the particle phase, while the gas phase can capture the convective heat transfer from the particle and reactor wall. Hence, further modelling is required to understand the heat transfer between the two-phase in a scaled-up device.

## 6.2 Future work

The future work of the current study are as follows:

1. Although the present study highlights the influence of particle loading, Froude and Stokes number on the thermal performance of the device under the horizontal position, it is also crucial to identify the impact of receiver orientation on the thermal performance of the SEVR.
2. A flow mitigation technique is necessary to reduce convective heat loss through the aperture to reduce hot air egress while preventing cold air ingress through the aperture by active or passive means.
3. Although the current study shows that temperature between the two-phases has little difference, further extension of CFD modelling is needed to understand the heat transfer and thermal performance of the two-phase flow within a potentially scaled-up device as the variation of reactor volume of the receiver is expected to influence the overall heat transfer, which can be complex to evaluate, especially for radiation losses due to their non-linear relationships as temperature rises.
4. Short- and long-term studies on the thermal cycling of particle properties are required to understand the suitable operating conditions for different downstream processes. Potential gaps to this would result in whether the device can be potentially operated for other applications but are not limited to applications such as thermal comminution of granular materials.
5. Further experimental and numerical study on the aerodynamics and thermal performance is required to be conducted under a higher regime of particle loading (i.e., four-way coupling regime) to understand both flow-field and thermal stability within the vortex flow, that is, to determine whether the device has a potential to operate as a particle reactor.

## Reference

1. McGlade, C. and P. Ekins, *The geographical distribution of fossil fuels unused when limiting global warming to 2 C*. Nature, 2015. **517**(7533): p. 187-190.
2. Pedraza, J., et al., *On the road to net zero-emission cement: Integrated assessment of mineral carbonation of cement kiln dust*. Chemical Engineering Journal, 2021. **408**: p. 127346.
3. Eglinton, T., et al., *Potential Applications of Concentrated Solar Thermal Technologies in the Australian Minerals Processing and Extractive Metallurgical Industry*. Journal of the Minerals Metals & Materials Society, 2013. **65**(12): p. 1710-1720.
4. Wang, P., et al., *Efficiency stagnation in global steel production urges joint supply- and demand-side mitigation efforts*. Nature Communications, 2021. **12**(1): p. 2066.
5. IEA (2020), W.E.O., IEA, Paris <https://www.iea.org/reports/world-energy-outlook-2020>, accessed on 27 April 2021.
6. Ellabban, O., H. Abu-Rub, and F. Blaabjerg, *Renewable energy resources: Current status, future prospects and their enabling technology*. Renewable and Sustainable Energy Reviews, 2014. **39**: p. 748-764.
7. Szargut, J.T., *Anthropogenic and natural exergy losses (exergy balance of the Earth's surface and atmosphere)*. Energy, 2003. **28**(11): p. 1047-1054.
8. Kodama, T., et al., *Flux measurement of a new beam-down solar concentrating system in Miyazaki for demonstration of thermochemical water splitting reactors*. Energy Procedia, 2014. **49**: p. 1990-1998.
9. Davis, D., et al., *Thermal performance of vortex-based solar particle receivers for sensible heating*. Solar Energy, 2019. **177**: p. 163-177.
10. Nathan, G.J., et al., *Solar thermal hybrids for combustion power plant: A growing opportunity*. Progress in Energy and Combustion Science, 2018. **64**: p. 4-28.
11. Z'Graggen, A., et al., *Hydrogen production by steam-gasification of petroleum coke using concentrated solar power—II Reactor design, testing, and modeling*. International Journal of Hydrogen Energy, 2006. **31**(6): p. 797-811.
12. Ho, C.K., *A review of high-temperature particle receivers for concentrating solar power*. Applied Thermal Engineering, 2016. **109**: p. 958-969.
13. Wang, W., et al., *Thermal performance analysis of free-falling solar particle receiver and heat transfer modelling of multiple particles*. Applied Thermal Engineering, 2021. **187**: p. 116567.
14. Ho, C.K. and B.D. Iverson, *Review of high-temperature central receiver designs for concentrating solar power*. Renewable and Sustainable Energy Reviews, 2014. **29**: p. 835-846.
15. Ebert, M., et al. *Upscaling, manufacturing and test of a centrifugal particle receiver*. in *Energy Sustainability*. 2016. American Society of Mechanical Engineers.
16. Ho, C.K., et al. *On-sun testing of an advanced falling particle receiver system*. in *AIP Conference Proceedings*. 2016. AIP Publishing LLC.
17. Tregambi, C., et al., *Fluidized Beds for Concentrated Solar Thermal Technologies—A Review*. Frontiers in Energy Research, 2021. **9**: p. 13.
18. Hirsch, D. and A. Steinfeld, *Solar hydrogen production by thermal decomposition of natural gas using a vortex-flow reactor*. International Journal of Hydrogen Energy, 2004. **29**(1): p. 47-55.
19. Kodama, T., et al., *Particle reactors for solar thermochemical processes*. Solar Energy, 2017. **156**: p. 113-132.

20. Z'Graggen, A. and A. Steinfeld, *Hydrogen production by steam-gasification of carbonaceous materials using concentrated solar energy—V. Reactor modeling, optimization, and scale-up*. International Journal of Hydrogen Energy, 2008. **33**(20): p. 5484-5492.
21. Davis, D., et al., *Solar-driven alumina calcination for CO<sub>2</sub> mitigation and improved product quality*. Green Chemistry, 2017. **19**(13): p. 2992-3005.
22. Chinnici, A., et al., *A novel solar expanding-vortex particle reactor: experimental and numerical investigation of the iso-thermal flow field and particle deposition*. Solar Energy, 2016. **133**: p. 451-464.
23. Arjomandi, M., et al., *Solar receiver*. 2018, U.S. Patent Application 15/750,297.
24. Saw, W.L., et al. *Technical feasibility of integrating concentrating solar thermal energy in the Bayer alumina process*. in *AIP Conference Proceedings*. 2020. AIP Publishing LLC.
25. Ho, C.K., et al. *High-temperature receiver designs for supercritical CO<sub>2</sub> closed-loop Brayton cycles*. in *ASME 2014 8th International Conference on Energy Sustainability collocated with the ASME 2014 12th International Conference on Fuel Cell Science, Engineering and Technology*. 2014. American Society of Mechanical Engineers Digital Collection.
26. Gregg, D., et al., *Solar gasification of coal, activated carbon, coke and coal and biomass mixtures*. Solar Energy, 1980. **25**(4): p. 353-364.
27. Murray, J.P. and E.A. Fletcher, *Reaction of steam with cellulose in a fluidized bed using concentrated sunlight*. Energy, 1994. **19**(10): p. 1083-1098.
28. Taylor, R., R. Berjoan, and J. Coutures, *Solar gasification of carbonaceous materials*. Solar Energy, 1983. **30**(6): p. 513-525.
29. Piatkowski, N., C. Wieckert, and A. Steinfeld, *Experimental investigation of a packed-bed solar reactor for the steam-gasification of carbonaceous feedstocks*. Fuel Processing Technology, 2009. **90**(3): p. 360-366.
30. Kodama, T., et al., *Fluidized bed coal gasification with CO<sub>2</sub> under direct irradiation with concentrated visible light*. Energy and Fuels, 2002. **16**(5): p. 1264-1270.
31. Falahati, H. and A. Tremblay, *The effect of flux and residence time in the production of biodiesel from various feedstocks using a membrane reactor*. Fuel, 2012. **91**(1): p. 126-133.
32. Z'Graggen, A., et al., *Hydrogen production by steam-gasification of petroleum coke using concentrated solar power—III. Reactor experimentation with slurry feeding*. International Journal of Hydrogen Energy, 2007. **32**(8): p. 992-996.
33. Chinnici, A., et al., *A novel solar expanding-vortex particle reactor: influence of vortex structure on particle residence times and trajectories*. Solar Energy, 2015. **122**: p. 58-75.
34. Hreiz, R., C. Gentric, and N. Midoux, *Numerical investigation of swirling flow in cylindrical cyclones*. Chemical Engineering Research and Design, 2011. **89**(12): p. 2521-2539.
35. Syred, N. and J. Beer, *Combustion in swirling flows: a review*. Combustion and Flame, 1974. **23**(2): p. 143-201.
36. Chinnici, A., et al., *Experimental and numerical investigation of the flow characteristics within a Solar Expanding-Vortex Particle Receiver-Reactor*. Solar Energy, 2017. **141**: p. 25-37.
37. Long, S., et al., *The flow-field within a vortex-based solar cavity receiver with an open aperture*. Experimental Thermal and Fluid Science, 2021. **123**: p. 110314.
38. Jenkins, B. and C. Bertrand, *Improvements in the design and operation of Alumina flash calciners*. IFRF Combustion Journal. 2001. Is, 2001. **10**: p. 2-18.

39. Cortes, C. and A. Gil, *Modeling the gas and particle flow inside cyclone separators*. Progress in Energy and Combustion Science, 2007. **33**(5): p. 409-452.
40. Davis, D., et al., *Particle residence time distributions in a vortex-based solar particle receiver-reactor: An experimental, numerical and theoretical study*. Chemical Engineering Science, 2020. **214**: p. 115421.
41. Davis, D., et al., *Particle residence time distributions in a vortex-based solar particle receiver-reactor: The influence of receiver tilt angle*. Solar Energy, 2019. **190**: p. 126-138.
42. Crowe, C., J. Chung, and T. Troutt, *Particle mixing in free shear flows*. Progress in Energy and Combustion Science, 1988. **14**(3): p. 171-194.
43. Dring, R. and M. Suo, *Particle trajectories in swirling flows (coal combustion gas turbine technology)*. Journal of Energy, 1978. **2**(4): p. 232-237.
44. Elghobashi, S., *On predicting particle-laden turbulent flows*. Applied Scientific Research, 1994. **52**(4): p. 309-329.
45. Gupta, A.K., D.G. Lilley, and N. Syred, *Swirl flows*. Tunbridge Wells, 1984.
46. Beér, J.M., *Combustion aerodynamics*, in *Combustion Technology*. 1974, Elsevier. p. 61-89.
47. Danckwerts, P., *Continuous flow systems. Distribution of residence times*. Chemical Engineering Science, 1995. **50**(24): p. 3857-3866.
48. Fogler, H.S. and L. Brown, *Distributions of residence times for chemical reactors*. Elements of Chemical Reaction Engineering, 2006. **4**.
49. Lede, J., et al., *Measurement of solid particle residence time in a cyclone reactor: a comparison of four methods*. Chemical Engineering and Processing: Process Intensification, 1987. **22**(4): p. 215-222.
50. Shilapuram, V., D.J. Krishna, and N. Ozalp, *Residence time distribution and flow field study of aero-shielded solar cyclone reactor for emission-free generation of hydrogen*. International Journal of Hydrogen Energy, 2011. **36**(21): p. 13488-13500.
51. Zhu, J., et al., *Experimental investigation on the energy and exergy performance of a coiled tube solar receiver*. Applied Energy, 2015. **156**: p. 519-527.
52. Wang, K., et al., *Experimental study on a coiled tube solar receiver under variable solar radiation condition*. Solar Energy, 2015. **122**: p. 1080-1090.
53. Tu, N., J. Wei, and J. Fang, *Numerical study on thermal performance of a solar cavity receiver with different depths*. Applied Thermal Engineering, 2014. **72**(1): p. 20-28.
54. Zhang, Q., et al., *An experimental study: Thermal performance of molten salt cavity receivers*. Applied Thermal Engineering, 2013. **50**(1): p. 334-341.
55. Zou, C., et al., *Design and optimization of a high-temperature cavity receiver for a solar energy cascade utilization system*. Renewable Energy, 2017. **103**: p. 478-489.
56. Karimi, R., T.T. Gheinani, and V.M. Avargani, *A detailed mathematical model for thermal performance analysis of a cylindrical cavity receiver in a solar parabolic dish collector system*. Renewable Energy, 2018. **125**: p. 768-782.
57. Hottel, H. and E. Cohen, *Radiant heat exchange in a gas-filled enclosure: Allowance for nonuniformity of gas temperature*. AIChE Journal, 1958. **4**(1): p. 3-14.
58. Hottel, H., et al., *Radiative transfer in anisotropically scattering media: allowance for Fresnel reflection at the boundaries*. Journal of Heat Transfer, 1968. **90**(1): p. 56-62.
59. Patankar, S., *Numerical heat transfer and fluid flow*. 1980: CRC press.
60. Zamansky, R., et al., *Radiation induces turbulence in particle-laden fluids*. Physics of Fluids, 2014. **26**(7): p. 071701.
61. Pouransari, H. and A. Mani, *Particle-to-fluid heat transfer in particle-laden turbulence*. Physical Review Fluids, 2018. **3**(7): p. 074304.

62. Pouransari, H. and A. Mani, *Effects of preferential concentration on heat transfer in particle-based solar receivers*. Journal of Solar Energy Engineering, 2017. **139**(2).
63. Frankel, A., et al., *Settling of heated particles in homogeneous turbulence*. Journal of Fluid Mechanics, 2016. **792**: p. 869-893.
64. Monchaux, R., M. Bourgoïn, and A. Cartellier, *Analyzing preferential concentration and clustering of inertial particles in turbulence*. International Journal of Multiphase Flow, 2012. **40**: p. 1-18.
65. Frankel, A., et al., *Optical depth in particle-laden turbulent flows*. Journal of Quantitative Spectroscopy Radiative Transfer, 2017. **201**: p. 10-16.
66. Farbar, E., I.D. Boyd, and M. Esmaily-Moghadam, *Monte Carlo modeling of radiative heat transfer in particle-laden flow*. Journal of Quantitative Spectroscopy Radiative Transfer, 2016. **184**: p. 146-160.
67. Rahmani, M., et al., *Effects of particle polydispersity on radiative heat transfer in particle-laden turbulent flows*. International Journal of Multiphase Flow, 2018. **104**: p. 42-59.
68. Petrasch, J., et al., *A novel 50kW 11,000 suns high-flux solar simulator based on an array of xenon arc lamps*. Journal of Solar Energy Engineering, 2007: p. 405-411.
69. Dong, X., et al., *Time-resolved spectra of solar simulators employing metal halide and xenon arc lamps*. Solar Energy, 2015. **115**: p. 613-620.
70. Li, J., J. Gonzalez-Aguilar, and M. Romero, *Line-concentrating flux analysis of 42kWe high-flux solar simulator*. Energy Procedia, 2015. **69**: p. 132-137.
71. Krueger, K.R., *Design and characterization of a concentrating solar simulator*. 2012, The University of Minnesota.
72. Kitzmiller, K.W., *Design, construction, and initial testing of a solar simulator and lab-scale small particle solar receiver*. 2012, San Diego State University.
73. Moumin, G., et al., *Solar treatment of cohesive particles in a directly irradiated rotary kiln*. Solar Energy, 2019. **182**: p. 480-490.
74. Tescari, S., et al. *Solar rotary kiln for continuous treatment of particle material: Chemical experiments from micro to milli meter particle size*. in *AIP Conference Proceedings*. 2020. AIP Publishing LLC.
75. Chinnici, A., et al. *First-of-a-kind investigation on performance of a directly-irradiated windowless vortex-based particle receiver*. in *AIP Conference Proceedings*. 2020. AIP Publishing LLC.
76. Craig, R.A., *Investigating the use of concentrated solar energy to thermally decompose limestone*. 2010, The University of Adelaide.
77. Steinfeld, A. and M. Schubnell, *Optimum aperture size and operating temperature of a solar cavity-receiver*. Solar Energy, 1993. **50**(1): p. 19-25.
78. Craig, K., et al., *Finite-volume ray tracing using Computational Fluid Dynamics in linear focus CSP applications*. Applied energy, 2016. **183**: p. 241-256.
79. Chinnici, A., et al., *Comparison of system performance in a hybrid solar receiver combustor operating with MILD and conventional combustion. Part II: Effect of the combustion mode*. Solar Energy, 2017. **147**: p. 479-488.
80. Tian, Z.F., G.J. Nathan, and Y. Cao, *Numerical modelling of flows in a solar-enhanced vortex gasifier: Part 1, comparison of turbulence models*. Progress in Computational Fluid Dynamics, 2015. **15**(2): p. 114-122.
81. ANSYS Inc. *ANSYS CFX Users Guide 19.3*. 2019.
82. Marchioli, C., M. Picciotto, and A. Soldati, *Particle dispersion and wall-dependent turbulent flow scales: implications for local equilibrium models*. Journal of Turbulence, 2006(7): p. N60.




83. Madadi, V., T. Tavakoli, and A. Rahimi, *Estimation of heat loss from a cylindrical cavity receiver based on simultaneous energy and exergy analyses*. Journal of Non-Equilibrium Thermodynamics, 2015. **40**(1): p. 49-61.
84. Petela, R., *Exergy of undiluted thermal radiation*. Solar energy, 2003. **74**(6): p. 469-488.
85. Hilpert, K. and U. Niemann, *High temperature chemistry in metal halide lamps*. Thermochemica Acta, 1997. **299**(1-2): p. 49-57.
86. Lau, T.C. and G.J. Nathan, *Influence of Stokes number on the velocity and concentration distributions in particle-laden jets*. Journal of Fluid Mechanics, 2014. **757**: p. 432-457.

# **Appendix A – Journal Submitted to Renewable Energy Journal**

# Statement of Authorship

Title of Paper	Influence of particle loading, Froude and Stokes number on the global thermal performance of a vortex-based solar particle receiver
Publication Status	<input type="checkbox"/> Published <input type="checkbox"/> Accepted for Publication <input checked="" type="checkbox"/> Submitted for Publication <input type="checkbox"/> Unpublished and Unsubmitted work written in manuscript style
Publication Details	Ang D, Chinnici A, Tian ZF, Saw WL, Nathan GJ. Influence of particle loading, Froude, and Stokes number on the global thermal performance of a vortex-based solar particle receiver. Renewable Energy; submitted, currently under review.

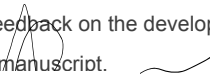

## Principal Author

Name of Principal Author (Candidate)	Daniel Ang
Contribution to the Paper	Conducted literature review on the vortex-based solar particle receiver, and its previous experiments and modelling work on thermal performance of this technology. Identified the key dimensionless parameters affecting the thermal performance of the device. Setup the experimental rigs and collected all experimental data. Developed a well-validated CFD model based on the collected experimental data. Interpreted the results from the experimental and numerical study. Wrote and edited the paper including all figures and tables.
Overall percentage (%)	70%
Certification:	This paper reports on original research I conducted during the period of my Higher Degree by Research candidature and is not subject to any obligations or contractual agreements with a third party that would constrain its inclusion in this thesis. I am the primary author of this paper.
Signature	 Date 21/07/2021

## Co-Author Contributions

By signing the Statement of Authorship, each author certifies that:

- the candidate's stated contribution to the publication is accurate (as detailed above);
- permission is granted for the candidate to include the publication in the thesis; and
- the sum of all co-author contributions is equal to 100% less the candidate's stated contribution.

Name of Co-Author	Alfonso Chinnici
Contribution to the Paper	Supervised the experiment design, including the setup of the experiment rigs. Helped to interpret the experimental data and provided detailed explanation from the data. Provided feedback on the development of the paper. Edited the manuscript. 
Signature	 Date 26/07/2021

Name of Co-Author	Zhao Feng Tian		
Contribution to the Paper	Supervised on the development of the CFD model. Assisted with the optimisation of the CFD model. Helped with the interpretation of results in the CFD model. Provided feedback on the manuscript. Edited the manuscript.		
Signature		Date	26/07/2021

Name of Co-Author	Woei Saw		
Contribution to the Paper	Supervised the development of the work. Advice given for the writing of the manuscript. Helped with the setup of the solar simulator lab facility. Edited the manuscript.		
Signature		Date	26/07/2021

Name of Co-Author	Graham 'Gus' Nathan		
Contribution to the Paper	Supervised the development of the work, including the suggestion on investigation with dimensionless parameters. Helped to analyse the data obtained from both the experimental and numerical study. Helped to structure the paper and provided significant feedback on its development. Edited the writing and manuscript.		
Signature		Date	26/7/2021

Please cut and paste additional co-author panels here &

# Influence of particle loading, Froude and Stokes number on the global thermal performance of a vortex-based solar particle receiver

## Authors

Daniel Ang <sup>1,\*</sup>, Alfonso Chinnici <sup>1</sup>, Zhao F. Tian <sup>1</sup>, Woei L. Saw <sup>1,2</sup>, Graham J. Nathan <sup>1</sup>

<sup>1</sup> Centre for Energy Technology, School of Mechanical Engineering, The University of Adelaide, SA 5005, Australia

<sup>2</sup> School of Chemical Engineering and Advanced Materials, The University of Adelaide, SA 5005, Australia

\* Corresponding author: danieljintung.ang@adelaide.edu.au (D. Ang)

## Abstract

We report a joint experimental and numerical study on the global thermal performance of a novel windowless vortex-based cavity receiver for potential thermal processing of suspended particles. This systematic study assesses the coupled influence of particle loading, Froude and Stokes number through variation of the inlet mass flowrate, particle size and loading on the global performance of the Solar Expanding Vortex Receiver-Reactor (SEVR) under steady-state conditions. The experiments employ polydispersed CARBO CP ceramic particles that are heated with an 18-kW<sub>el</sub> Metal Halide three-lamp solar simulator. A numerical study was also performed using computational fluid dynamics (CFD) software ANSYS/CFX 2019 R1. It was found that the particle volumetric loading and Froude number have primary controlling influence, while the Stokes number has a secondary influence on the global performance for these conditions. An overall thermal efficiency of 67% was obtained under high particle loading and Froude numbers.

**Keywords:** CST; Particle receiver technology; CFD; Vortex flow; Particle size; Heat transfer

## 1 Introduction

The transition to net-zero carbon emissions by 2050 poses a significant challenge for both industrial and energy sectors as current statistics reveals that the amount of CO<sub>2</sub> needs to be reduced by 45% over the coming decade to achieve the common goal [1, 2]. The production of high-value products is vital to the global economy, such as aluminium, steel and cement, are also energy intensive, difficult to abate and responsible for some 15% of global CO<sub>2</sub> emissions [3-5]. One of the technology options with potential to contribute to this challenge is concentrated solar thermal energy (CST) technologies. One category of the CST technology with potential to achieve high temperatures of 800 – 1200 °C is the particle-based solar

receivers, which is receiving growing interest due the stability of selected particles at those temperatures, their efficiency absorption of radiant energy and high specific heat capacity of particles [6, 7]. A wide range of particle receivers has been tested, such as the fluidised bed receiver, falling particle receiver, vortex-flow particle receiver and centrifugal receivers [8-11]. Of these, the vortex-flow solar receiver is particularly well suited to heating reacting particles through radiation since it heats the particles in suspension within a gaseous flow [12]. To date, there is currently limited understanding on the mechanisms affecting the thermal performance of vortex flow receiver technology. Therefore, the overall objective of the present investigation aims to increase understanding on the thermal performance on this class of solar thermal technology.

The vortex-based solar receiver features a cavity configuration, which mitigates both radiative and convective heat losses effectively [13-16]. It also features an aperture for direct irradiation of particles through the penetration of concentrated solar radiation (CSR) into the cylindrical chamber, which is transported along the chamber by the vortical flow [17-19]. The interaction of the semi-diluted two-way coupling regime between the gas and particle phase allows for consistent heating and transportation within the device [20, 21]. This makes it well suited to applications for high processing heat, but not limited to reacting flows. The solar vortex receiver (SVR) was demonstrated for gasification at ETH/PSI [22] and is currently being further developed by the University of Adelaide [18]. Previous successful demonstration of the device includes laboratory scale testing on methane reformation, metal oxide reduction, solar gasification and mineral processing [23-27]. However, these studies have been directed at demonstrating effectiveness for a chemical reaction, reporting measurements such as chemical conversion and efficiency. There is currently limited understanding on the use of such device for sensible heating through injection of inert particles and gas. Furthermore, little information is presently available on the heat transfer between the two-phases, heat losses as well as particle and temperature distribution within the device based on evaluating the key role of dimensionless parameters within vortex particle receivers. Hence, the paper aims to meet these needs.

An alternative configuration of the SVR, termed as the Solar Expanding Vortex Receiver (SEVR), features a back-entry flow configuration to reduce the transport of particles and heat through the aperture [18]. Recent global thermal performance study on a windowless configuration of this device has been commissioned with aerodynamic suction applied at the outlet, which reduces particle egress and heat losses through the aperture for the windowless

configuration [28]. Whilst the device is particularly well suited to applications for reacting flows, the heat transfer in such devices is difficult to evaluate due to the complex and non-linear relationships between enthalpy and temperature rise within the system. In contrast, an investigation of non-reacting two-phase flows reduces the complexity to allow increased understanding on the underlying mechanisms affecting the thermal performance within the device. Despite the development of a 1-D mathematical model [29], limited measured and numerical data are currently available to assess the coupled effects of operational parameters under realistic boundary conditions with solar irradiation. In addition, no previous work has been demonstrated to examine the fraction of thermal energy absorbed between the two phases within the SEVR. Hence, another objective of the present investigation is therefore to enhance understanding on the energy partition between the two-phases through systematic study on the combined effects of particle size and loading as well as inflow conditions of the SEVR.

Previous experimental and analytical studies on particle residence time have highlighted that the particle behaviour within the SEVR is dominated by two different flow regimes, which is the Froude Stokes and cyclonic regime [30]. Under the Froude Stokes ( $Fr < 4$ ) regime, it was observed the particle trajectories are dominated by gravity when Stokes number is sufficiently high, which increases their residence time due to recirculation through the central recirculating zone (CRZ) [30]. In contrast, the particle trajectories in the cyclonic regime ( $Fr > 4$ ) are independent to Stokes number as inertial force dominates over gravitational forces, causing particles to preferentially distribute close to the wall and resulting in a shorter residence time. In addition, another study is conducted based on the influence of receiver tilt angle on particle residence time within the SEVR, which shows that the Froude number is less dependent on the particle residence time as the tilt angle is increased. This is mainly due to the weaker response of particles to the vortex flow as Stokes number increases, which allows particles of higher Stokes number to be recirculated [31]. Although the study of particle size and inflow conditions has been investigated systematically under isothermal conditions previously, little information is currently available on the effects of particle loading on the residence time. Hence, an additional objective of this paper is to understand the coupling effects of the particle residence time on the thermal performance under the two distinctive flow regimes.

To address the aforementioned needs, the current investigation aims to provide a new understanding on the global thermal performance of the windowless vortex-based solar receiver. The tasks and objectives of this paper are:

- (a) To characterise the key influencing dimensionless parameters (particle loading, Froude and Stokes number) on the thermal efficiency and heat transfer within the reactor.
- (b) To study the combined effects between the two distinctive flow regimes, particle residence time and distribution on the thermal performance of the reactor.
- (c) To understand the fraction of thermal energy partitioned between the gas and particle phases within the reactor.
- (d) To develop a robust computational fluid dynamics (CFD) model validated experimental data for assisting the fundamental understanding of key controlling parameters affecting the global thermal performance within the SEVR.

## 2 Methodology

### 2.1 Experimental Arrangements

Table 1: (a) Geometrical dimensions and (b) Thermal properties of the SEVR, insulation and particles. Please refer to Figure 1 for the schematic of the SEVR and geometric symbols.

(a) Geometric properties		
	Parameter	Value
<b>Receiver length</b>	$L$ , (mm)	238
<b>Receiver diameter</b>	$D_c$ , (mm)	190
<b>Cone angle</b>	$\theta$ , ( $^\circ$ )	40
<b>Aperture diameter</b>	$d_{ap}$ , (mm)	100
<b>Inlet jet diameter (each)</b>	$d_{in}$ , (mm)	6
<b>Outlet jet diameter</b>	$d_{out}$ , (mm)	11
<b>Particle Sphericity</b>	$P_{sp}$ , (-)	0.9
<b>Particle Density</b>	$\rho_p$ (kg/m <sup>3</sup> )	3270
(b) Thermal properties		
<b>Insulation thickness</b>	$L_{ins}$ , (mm)	60
<b>Insulation Thermal conductivity</b>	$k$ , (W/mK)	0.14
<b>Particle specific heat capacity</b>	$c_{p,p}$ , (KJ/kg)	1.15
<b>Emissivity of particles</b>	$\varepsilon_p$ , (-)	0.95
<b>Emissivity of reactor wall</b>	$\varepsilon_{eff}$ , (-)	0.85

Laboratory-scale measurements were performed using a three-lamp solar simulator (OSRAM HMI 6000W/SE, 6 kW<sub>el</sub> each) to heat particles within a windowless SEVR. Calibration of the lamp was conducted based on previous literature [32, 33]. From the calibration, the total input solar energy introduced to the receiver aperture was measured to be approximately **2.10 kW**



and features a Gaussian shape flux profile. Specific details of the calibration methods can be found in the supplementary material.

A schematic diagram of the device, showing key terminology and dimensions, is presented in Figure 1a and 1b, while the experimental rig setup is shown in Figure 1c. The SEVR features a stainless-steel cavity insulated with ceramic thermal insulation fibre mats. It also features a radial outlet located at the axial position to expel the heated air and particles, along with two tangential inlets for the injection of compressed air and particles. The particles selected for the investigation were made of CARBO CP ceramic, due to their good stability in high temperature, high specific heat capacity and consistent near-spherical shape. The geometrical dimensions and thermal properties of the receiver and particles are presented in Table 1.

Two electronic mass flow controllers were applied to supply compressed air for both tangential inlets, while a mass flow reader was used to measure the flow rate at the radial outlet. A particle screw feeding system was applied to control the particle-feeding rate into the system, while the solar source was introduced at the aperture plane of the device. For measurements of the global thermal performance of the receiver, an array of 16 Type-K thermocouples was installed throughout the device to obtain temperature measurements at the inlet, outlet ( $T_{a,o}$ ), internal and external wall ( $T_w$ ) sections. The outlet was connected to a water jacket heat exchanger to cool down the heated air and particles before being carried away by the induced draft fan. Overventilated conditions were employed at the outlet to control the particle and air egressing through the open aperture, as proven effective in previous studies [34, 35]. The experiment is conducted under hot conditions with no wind at horizontal orientation. The temperatures were taken continuously, with the time-averaged results were reported under steady-state conditions. During each test, particles were only introduced when steady-state conditions were reached. The steady-state assumption was taken when all measured temperatures were within a fluctuation range of  $\pm 0.8$  °C/min. The warm-up time of the receiver to reach steady-state from cold conditions prior to particle injection was around 80 – 90 minutes, with gaps of 5 – 10

minutes required for each particle-laden test to reach steady state, while an additional 10 minutes was required for the system to return its original state prior to the subsequent tests.

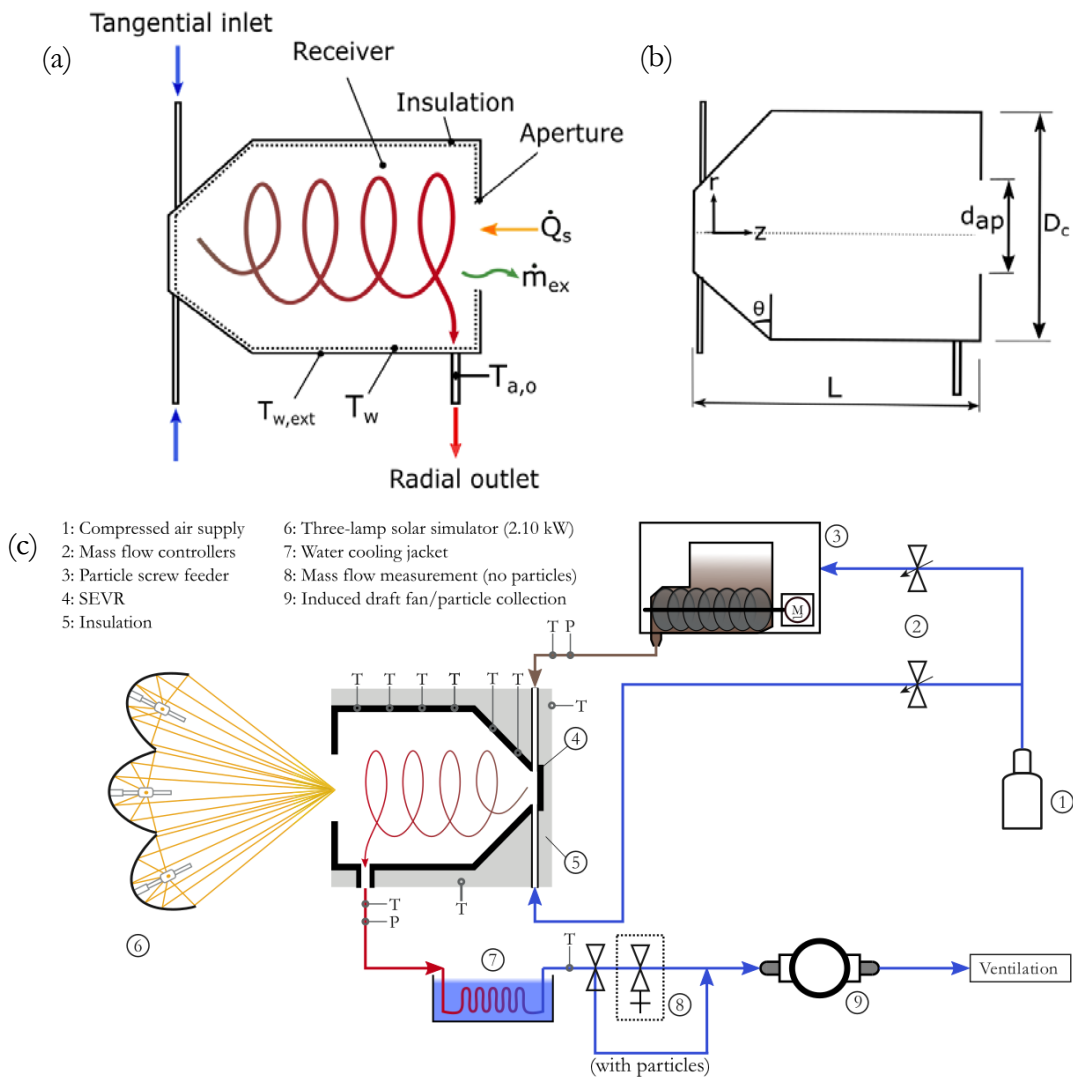


Figure 1: (a) Schematic Diagram of the SEVR (b) Geometrical details of the SEVR (c) arrangement of the SEVR experimental rig for the global thermal performance study (Modified from earlier work of [28]).

## 2.2 Operational Conditions

Table 2: A summary of the experimental and numerical conditions chosen for this study.

Parameters	Experimental		Numerical	
	Single-phase	Two-phase	Single-phase	Two-phase
Inlet mass flow rate, $\dot{m}_{a,i}$ [g/s]	1.37, 1.57, 2.35, 2.75		1.37, 1.57, 2.35, 2.75	
Inlet flow velocity, $U_{in}$ [m/s]	20.63, 23.57, 35.36, 41.26		20.63, 23.57, 35.36, 41.26	

Outlet mass flow rate, $\dot{m}_{a,o}$ [g/s]	1.82, 2.08, 3.14, 3.65		1.82, 2.08, 3.14, 3.65	
Outlet flow velocity, $U_{out}$ , (m/s)	16.31, 18.76, 28.10, 32.80		16.31, 18.76, 28.10, 32.80	
Mean particle diameter, $d_p$ ( $\mu m$ )	-	120, 155, 185	-	85, 120, 155, 185, 240
Inlet particle volumetric loading ( $\phi$ )	-	$2.96e^{-5}$ , $4.45e^{-5}$ , $9.01e^{-5}$	-	$2.96e^{-5}$ , $4.45e^{-5}$ , $9.01e^{-5}$
Input Solar Flux (kW)	2.1	2.1	2.1	2.1
Net Air Ingress, $\alpha$ , (%)	33	33	33	33

Table 2 presents all the operating conditions used for both experimental and numerical study. For a given level of suction, the measured value of  $\dot{m}_{a,o}$  was constant and the value (%) of the net air ingress (positive), or egress (negative) from the device is calculated based on:

$$\alpha = \left[ \frac{\dot{m}_{a,o} - \dot{m}_{a,i}}{\dot{m}_{a,i}} \right] \times 100\% \quad , \quad (1)$$

where  $\dot{m}_{a,o}$  and  $\dot{m}_{a,i}$  are air mass flow rate of the gas phase at the outlet and inlet section, respectively. According to the preliminary study of Chinnici, Davis [28], it was observed that an air ingress of approximately 15% is effective in preventing particle egress through the aperture. Thus, the study implements a higher air ingress rate to prevent the occurrence of particle egress.

### 2.3 Numerical Procedure

The commercial computational fluid dynamics (CFD) software, ANSYS/CFX 2019 R1, was chosen for the numerical study to provide insight into the heat transfer and particle distribution within the SEVR. The Gaussian-shaped solar flux input at the aperture is modelled by using the expression function in ANSYS/CFX via the expressions found in Steinfeld and Schubnell [36], as shown in Section 2 of the supplementary material. The operating conditions adopted in the numerical study included those employed in the experimental campaign and covered some additional cases as reported in Table 2. The setup of the model was based on the CFD user manual and previous works [37-39]. Details of the validation process can be found in the supplementary material. A good agreement was located across the test cases as all model

standard errors are within the range of 20%, while the Gaussian flux model is within 10% accuracy (See supplementary material).

Since the temperature of air from both measured and simulated cases are complementary, the comparison of outlet temperature between the two-phases under simulated conditions are described by a percentage difference as follows:

$$\frac{\Delta T_{p-a,o}}{T_{a,o,tp}} = \left| \frac{T_{p,o,tp} - T_{a,o,tp}}{T_{a,o,tp}} \right| \times 100\%, \quad (2)$$

Equation (2) determines the temperature difference between the air and particle phases in the numerical study with an averaged area at the outlet plane. Here, the air temperature of the two-phase flow at the outlet is denoted by  $T_{a,o,tp}$ , while  $T_{p,o,tp}$  refers to the area-averaged particle temperature at the outlet.

## 2.4 Thermal Performance Analysis

The energy rate balance equation is applied to assess the influence of Froude and Stokes numbers as well as particle loading on the thermal performance of the lab-scale SEVR. The overall energy rate balance equation is:

$$\dot{Q}_s = \dot{Q}_{abs} + \dot{Q}_{cond} + \dot{Q}_{loss,ap,rad} + \dot{Q}_{loss,ap,conv} , \quad (3)$$

where  $\dot{Q}_{abs}$  is the rate of energy absorbed by the mixture of gas and particle phases at the outlet of the SEVR, which can be approximately calculated as follows,

$$\dot{Q}_{abs} = \dot{m}_{a,o} c_{p,a} (T_{a,o} - T_{in}) + \dot{m}_{p,o} c_{p,p} (T_{p,o} - T_{in}) , \quad (4)$$

where  $\dot{m}_{a,o}$  and  $T_{a,o}$  were the measured values of temperature and air mass flow rate of the gas phase at the outlet.

The conduction heat term is estimated based on the mean external surface temperature of the insulation, termed as  $\bar{T}_{w,ext}$ , and the mean inner wall temperature,  $\bar{T}_w$ , thermal conductivity ( $k$ ),  $A_{SEVR}$  is the internal surface area of the SEVR and thickness of the ceramic insulation ( $L_{ins}$ ).

$$\dot{Q}_{cond} = \frac{k A_{SEVR} (\bar{T}_w - \bar{T}_{w,ext})}{L_{ins}} , \quad (5)$$

A term  $\dot{Q}_{loss,ap,rad}$  is defined as the radiative heat loss through the aperture, which is described with the following equation:

$$\dot{Q}_{loss,ap,rad} = \varepsilon_{eff} \pi r_{ap}^2 \sigma (\bar{T}_w^4 - T_{\infty}^4), \quad (6)$$

where  $\varepsilon_{eff}$  is the emissivity of the cavity receiver and  $\sigma$  ( $5.67 \times 10^{-8} \text{ W m}^{-2} \text{ K}^{-4}$ ) is the Stefan-Boltzmann constant.

The convective heat loss term ( $\dot{Q}_{loss,ap,conv}$ ) through the aperture is determined as follows:

$$\dot{Q}_{loss,ap,conv} = \dot{m}_{ex} c_{p,a} (T_{a,o} - T_{\infty}), \quad (7)$$

where  $\dot{m}_{ex}$  is the amount of air exchanged through the aperture (ambient air entrained into or hot air leaving the device through the aperture), this is obtained by finding the difference between the measured values of the total mass flow rates of air at the inlet and outlet sections of the device ( $\dot{m}_{ex} = \dot{m}_{a,o} - \dot{m}_{a,i}$ ). The conductive heat loss term ( $\dot{Q}_{cond}$ ) for the current study is of less significance and thereby negligible as the conductive heat loss within the reactor reduces as the reactor is further scaled-up due to the increase of volume to surface area.

The overall thermal efficiency of the receiver,  $\eta_{th}$ , is defined to account for the heat absorbed by both the gas and particle phases,

$$\eta_{th} = \left[ \frac{\dot{Q}_{abs}}{\dot{Q}_s} \right] \times 100\% = \left[ \frac{\dot{m}_{a,o} c_{p,a} (T_{a,o} - T_{a,i}) + \dot{m}_{p,o} c_{p,p} (T_{p,o} - T_{p,i})}{\dot{Q}_s} \right] \times 100\%, \quad (8)$$

In the numerical study, the particle and air efficiency are defined to find out how much energy is partitioned between the two phases,

$$\eta_{th,air} = \left[ \frac{\dot{m}_{a,o} c_{p,a} (T_{a,o} - T_{a,i})}{\dot{Q}_s} \right] \times 100\%, \quad (9)$$

$$\eta_{th,particle} = \left[ \frac{\dot{m}_{p,o} c_{p,p} (T_{p,o} - T_{p,i})}{\dot{Q}_s} \right] \times 100\%, \quad (10)$$

The mass flow rates of the particle phase at the inlet and outlet being equal with the assumption that there is no particle egressing through the aperture (i.e.,  $\dot{m}_{p,i} = \dot{m}_{p,o}$ ). It is important to note that the particle temperature is assumed equilibrium to the gas phase (i.e.,  $T_{a,o} = T_{p,o}$ ) in the experiments due to challenges in measuring particle temperature. To better understand heat transfer of the device and its potential configuration, the enthalpy ratio,  $\Delta H_{a-p}$ , is used to define the ratio of heat absorbed by the gas phase on the heat absorbed by the particle phase. The definition of the enthalpy ratio is as follows:

$$\Delta H_{a-p} = \frac{\dot{m}_{a,o} c_{p,a} (T_{a,o} - T_{a,i})}{\dot{m}_{p,o} c_{p,p} (T_{p,o} - T_{p,i})}, \quad (11)$$

## 2.5 Key Dimensionless Parameters

The use of non-dimensional operational parameters is essential to determine the trend of thermal performance within the device. As majority of gas and particle within the reactor occupies the cylindrical chamber for most of the period, the cone-cylinder intersection is taken as the reference position for the tangential velocity and characteristic length scale, similar to that in Davis, Troiano [30].

Table 3: The operational details of the Froude-Stokes and cyclonic regimes of operation, generated with four inlet tangential velocities and values of the key-dimensionless parameters based on CFD results.

Flow Regimes	Froude-Stokes		Cyclonic	
$\dot{m}_{a,i}$ [g/s]	1.37	1.57	2.35	2.75
$U_{t,max}$ [m/s]	1.60	1.83	2.90	3.16
$Sk_c$ for $d_p = 85\mu\text{m}$	0.60	0.67	1.15	1.37
$Sk_c$ for $d_p = 120\mu\text{m}$	1.08	1.36	2.32	2.60
$Sk_c$ for $d_p = 155\mu\text{m}$	1.82	2.23	3.82	4.34
$Sk_c$ for $d_p = 185\mu\text{m}$	2.59	3.16	5.45	6.18
$Sk_c$ for $d_p = 240\mu\text{m}$	4.36	5.43	9.16	10.40
$Fr$	2.5	3.4	8.6	10.2

The Stokes number,  $Sk_c$  defined as how closely a particle follows the streamline of the gas phase at the cylindrical chamber of the receiver [40]. This can be evaluated as follows:

$$Sk_c = \frac{\rho_p U_{t,max} d_p^2}{18\mu_f D_c}, \quad (12)$$

where  $\rho_p$  refers to the density of particle,  $d_p$  the mean particle diameter,  $\mu_f$  the dynamic viscosity of air,  $D_c$  the characteristic length scale and  $U_{t,max}$  the maximum tangential velocity of the fluid, which is estimated based on the CFD model.

The Froude number is defined as the ratio between the inertial effect and gravitational force within a hydrodynamic system. The term of this formula is assumed to be similar to a cyclone separator, which aims to centrifuge particles along the walls [41].

$$Fr = \frac{U_{t,max}^2}{gR}, \quad (13)$$

where  $g$  is the gravitational acceleration and  $R$  being the radius of the cylindrical chamber.

The dimensionless particle residence time,  $\bar{\tau}_p/\tau_{nom}$ , is evaluated based on the ratio of average particle residence time obtained the numerical study  $\bar{\tau}_p$  to the nominal particle residence time  $\tau_{nom} = V_R/\dot{V}_{in}$  as evaluated in [42]. The average residence time is extracted from the numerical study, while the nominal residence time is the ratio of receiver volume to the air volumetric flowrate. Table 4 summarises the calculated values of the dimensionless parameters for both the Froude-Stokes and Cyclonic regimes.

Another important parameter is the swirl number ( $S$ ), which is defined as the ratio of tangential momentum flux to the axial momentum flux and is used to characterise the vortex intensity within a swirling flow [43].

$$S = \frac{\int_0^R \rho u_t u_{ax} r^2 dr}{R \int_0^R \rho u_t^2 r dr} , \quad (14)$$

where  $\rho$  is the density of the fluid, and  $u_t$  and  $u_{ax}$  are the tangential and axial velocity components, respectively.

### 3 Results and Discussion

#### 3.1 Influence of key dimensionless parameters on normalised wall temperature

Figure 2 presents the normalised wall temperature distribution across the inner wall of the reactor from the experimental study with respect to its influence by the key operational parameters, namely, the Froude number, particle volumetric loading and particle size. The difference between the wall and ambient air temperature is normalised by  $\frac{\dot{Q}_s}{(\dot{m}_{a,o}c_{p,a} + \dot{m}_{p,o}c_{p,p})}$ , that is an ideal approximation of temperature increase (without any heat losses to the ambient air) in the SEVR for a given  $\dot{Q}_s$ . The normalised wall temperature indicates how close the heat transfer in the SEVR is to the ideal scenario, i.e., no heat losses to the ambient environment. For most of the cases in Figure 2, an overall trend is spotted, that is, the dimensionless wall temperature is higher at the conical section ( $0 < z/L < 0.4$ ) than that at the cylindrical part ( $z/L > 0.4$ ), indicating higher solar energy absorbed at the conical section ( $0 < z/L < 0.4$ ). This is as expected, as in the SEVR/solar lamp setting reported in the paper, the solar beams are directed towards the cone from the aperture. Across all cases, it can be observed that the thermal energy absorbed on the wall is the highest at the conical section at  $z/L = 0.17$ , which is attributed to the angle of radiation from the solar simulator. As a result, the temperature in the front region (i.e. the conical section,  $0 < z/L < 0.4$ ) is cooler than in the back region (i.e. the cylindrical part,  $z/L > 0.4$ ).

From Figure 2a, both the Froude-Stokes ( $Fr < 4$ ) and cyclonic ( $Fr > 4$ ) regimes are independent of the rise or distribution of normalised temperature of the wall. This implies that the rise of normalised temperature is dominated solely by the increment of flow velocity in the Froude number component, which indicates that heat transfer to the wall is increased when increasing the inlet flow velocity. From the trend of Figure 2b, the normalised temperature increases with the particle loading, this indicates that the flow of suspended particles within the reactor has an improved ability to absorb the radiant energy from the flow. In addition, the increment of particle loading increases the mass of particle, thereby reducing the corresponding thermal energy absorbed in the two-phase flow. Therefore, the normalised wall temperature increases with the increment of particle volumetric loading. As shown in Figure 2c, it is seen that the decreasing the particle size leads to a slight increment of normalised wall temperature. The particle size reduction leads to an increment of the number of particles in the flow for a fixed particle mass flowrate in the inlets. It was found that the ratio of change of total particle surface area for different sizes such as 185 microns to 155 microns is 0.7, while the ratio of



total particle surface area of 155 microns to 120 microns is 0.59; thus, the increment of particle surface area leads to a slightly enhanced heat transfer in the chamber.

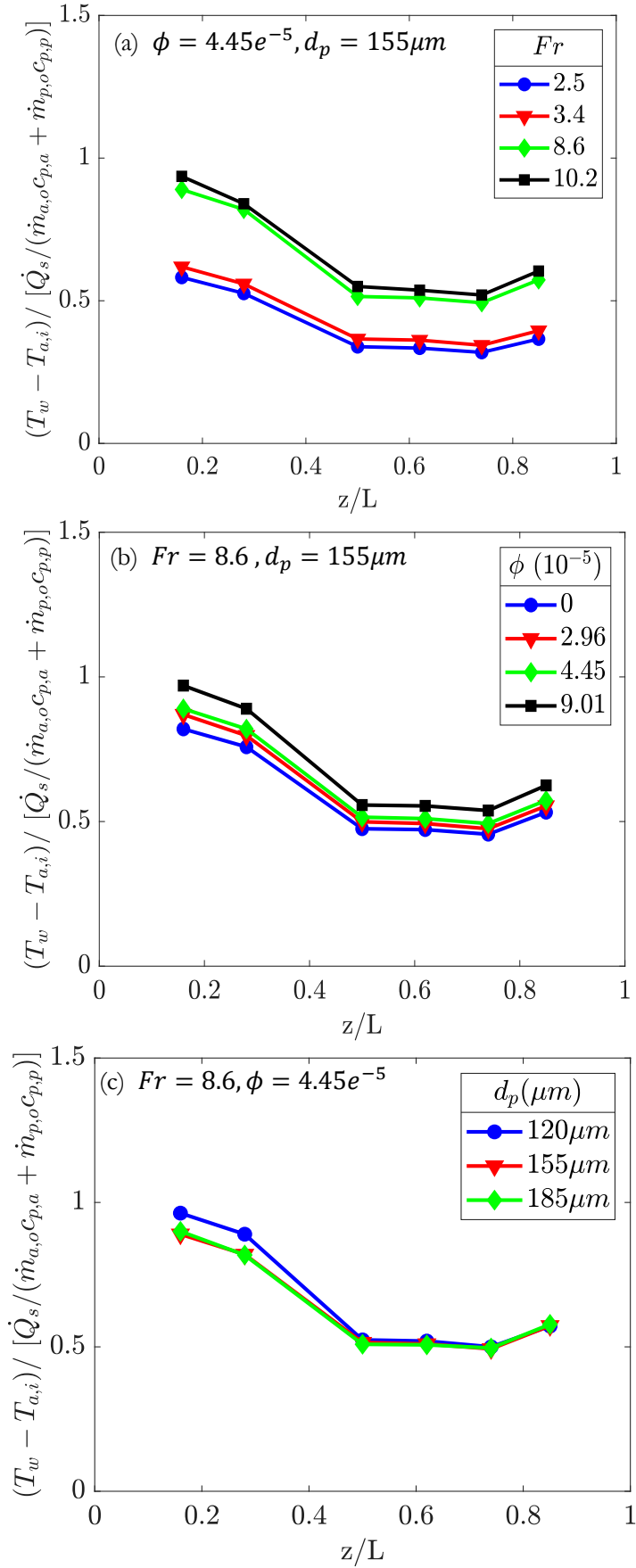


Figure 2: Axial distribution of the normalised wall temperature of the receiver for a series of (a) Froude number with a constant particle loading and size. (b) Particle loading with a constant Froude number and particle size. (c) Particle size with a constant Froude number and particle loading.

## 3.2 Influence of key dimensionless parameters on outlet temperature and particle distribution in the receiver

### 3.2.1 Effects on outlet temperature

Figure 3a-d demonstrates the effects of the key dimensionless parameters ( $Fr$ ,  $\phi$ ,  $Sk_c$ ) for both measured air temperature and normalised air temperature at the outlet obtained from the experimental campaign. From the results of Figure 3a, it can be seen that the outlet temperature is dominated by the Froude number as previously mentioned in section 3.1. It is shown that the increment of Froude number in the gas phase at a constant energy input decreases the temperature rise of the flow in the reactor. This is as expected, since the increase of inlet mass flowrate reduces the temperature rise as shown in Equation 4. It is also observed that as the Stokes number is increased (by increasing particle diameter), the temperature drop also increases for ( $Fr = 2.5, 3.4, 8.6$ ) but not for ( $Fr = 10.2$ ), this is due to the greater surface area of the particles which allows for absorbing more radiant heat. Addition of particles increased the total heat capacity of the two-phase flow to absorb heat. With the increase of Stokes number (i.e, particle size), the total surface area of particles decreases, leading to the slight decrement of the heat capacity as observed in Figure 3b. It is unclear what causes the outlet temperature to decrease at the outlet when particle size increases from  $155 \mu m$  to  $185 \mu m$  for  $Fr = 10.2$ . This may be attributed to the measurement error. An agreement was also found in Figure 3b, which shows that as the heat capacity term normalises the outlet temperature, more energy is absorbed by the two-phase flow when the Froude number increases, as seen in Figure 3a. As the Froude number increases, it is expected that the rate of air exchanged at the aperture also increases. This causes flow recirculation to occur in allowing more hot air from within the cavity to egress through the aperture, while cold ambient air ingresses the device through back mixing from the recirculating flow.

The result of Figure 3c shows that as the particle loading is increased, the temperature at the outlet gradually increases. A general trend clearly shows that the increment of Stokes number (by increment of particle sizes) leads to a decrease in outlet temperature, indicating deteriorated overall heat transfer from the radiation input to the gas and particle phases in the SEVR. The particle loading positively affects the overall heat transfer in the chamber, evidenced by the increasing normalised outlet temperature shown in Figure 3b, while a negative effect on the measured outlet temperature is shown in Figure 3a. As expected, increasing particle loading will have increased particle surface area and increased heat capacity. The increased particle

surface will enhance the heat transfer from the radiative source to the particles and air around the particles.

Moreover, the increased overall heat capacity will reduce the absolute temperature measured at the outlet. It is worth noting that for low particle loading ( $\phi = 2.96 \times 10^{-5}$  and  $4.45 \times 10^{-5}$ ), the effects of Stokes number on the temperature at the outlet and the overall heat transfer are minor while for a high particle loading ( $\phi = 9.01 \times 10^{-5}$ ), the effects can be more significant. This is because the increment of particle size (i.e., Stokes number) weakens the heat transfer in the chamber due to the reduced total surface area of particles; however, this effect is not apparent for low particle volume loadings. With the increment of particle volume loading, it is expected that the effect will be more pronounced.

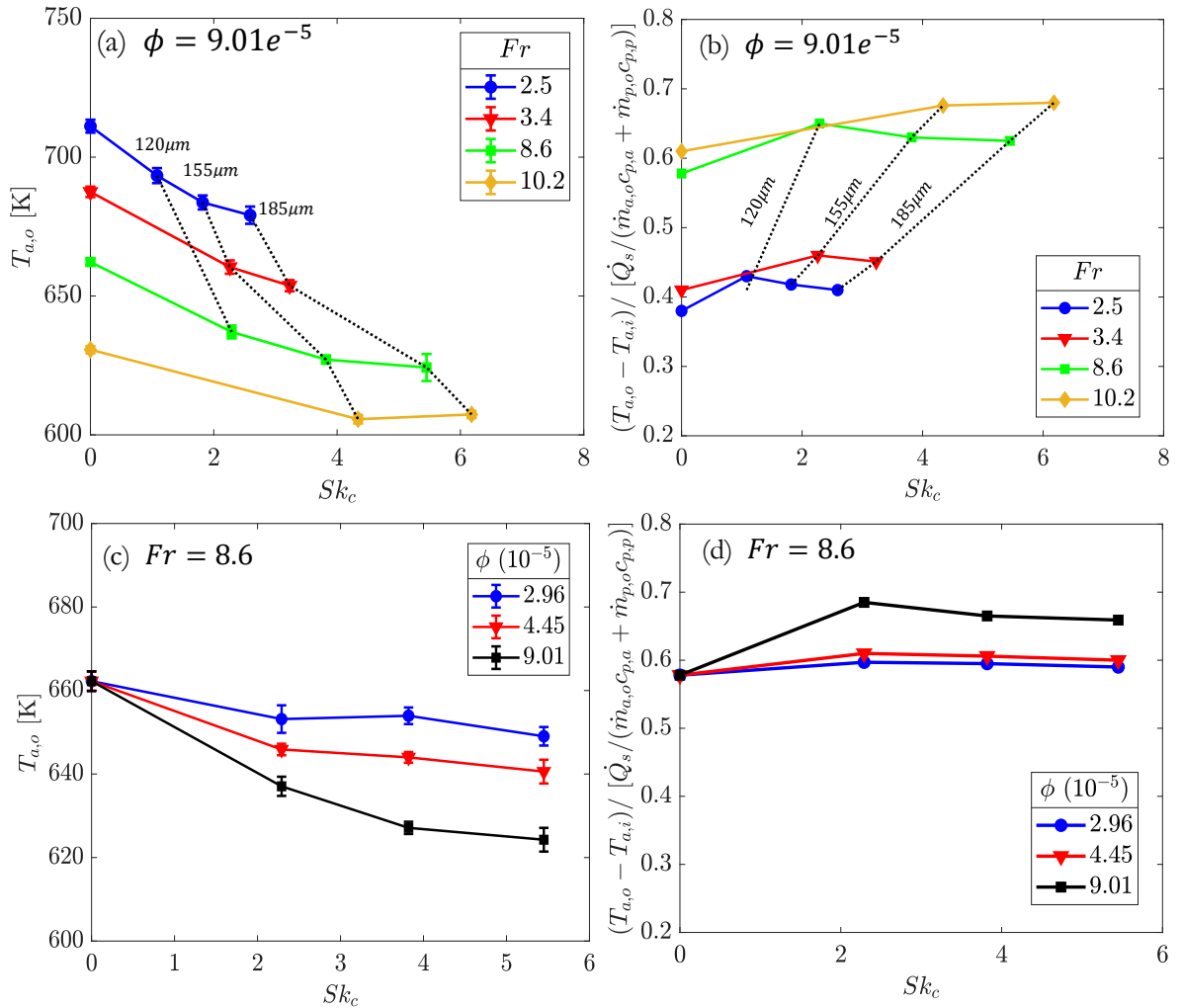


Figure 3: Measured values of

- Gas outlet temperature at a constant particle loading for different values of Froude number.
- Normalised gas outlet temperature at a constant particle loading for different values of Froude number.
- Gas outlet temperature at a constant Froude number for different values of particle loading.
- Normalised gas outlet temperature at a constant Froude number for different values of particle loading.

### 3.2.2 Effects on temperature difference between two-phases

CFD has been employed to estimate the temperature difference between the two-phases. Figure 4 presents the temperature difference between two-phases with respect to Stokes number. From both Figures 4a & 4b, it can be seen that the particle phase temperature is slightly higher than that of the gas phase, which demonstrates that the two-phases are almost in equilibrium, however, the minimal difference between the two-phases were said to have minor effects on overall heating processes for most applications. From Figure 4a, it can be seen that under the Froude-Stokes regime ( $Fr < 4$ ), the particle temperature difference tends to collapse closely as the Stokes number is increased, whereas, under the cyclonic regime ( $Fr > 4$ ), the temperature difference is reduced as the Froude number increases, this implies that the temperature difference is uniform under the Froude-Stokes regime showing that particles are more uniformly heated under this regime than in the cyclonic regime, while being arbitrary in the cyclonic regime as it is mainly dominated by the nominal residence time of the reactor. It is important to note that the Stokes number at the chamber should be within a certain threshold for operations under different Froude number, to attain the optimal particle exiting temperature. As shown in Figure 4b, it can be concluded that temperature difference between two-phases with various mass loading is consistent as observed for most of the cases ( $Sk_c > 2$ ), which shows that the temperature difference is not significantly affected by the particle loading when Stokes number is large. Lastly, it is worth noting that similar trends were observed for cases with different Froude numbers.

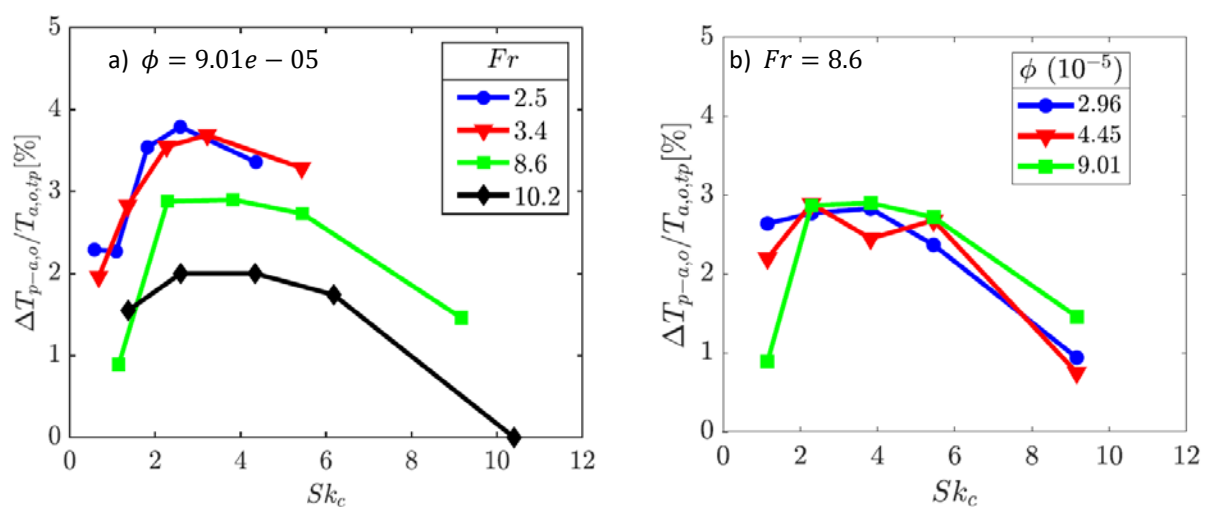


Figure 4: Calculated percentage difference between air and particle temperature on Stokes number as a function of (a) Froude number with constant particle loading. (b) Particle loading with constant Froude number.

### 3.2.3 Temperature and Particle Distribution within the Device

From the numerical study, Figure 5 illustrates the temperatures and particle volume concentration within the receiver. Both temperatures and particle volume concentration are probed using the centreline evolution function in the CFD. Under the Froude-Stokes regime ( $Fr < 4$ ) as shown in Figure 5a, it can be seen that the temperature of particle phase is greater than the gas phase in the centreline, this is because more energy is being absorbed by the particles phase as they are directly exposed to the incoming radiant energy. It is important to note that there are less particles (lower particle volume concentration,  $\psi$ ) at the centreline region than at the near-wall region. The air and particle temperature at the mid and near-wall regions are almost in equilibrium. It is expected that the gas phase temperature to be near uniformly distributed with other radial regions due to flow recirculation. The particle volume concentration at the mid and near wall region are similar as the particles are more uniformly distributed under the Froude-Stokes regime. Under the cyclonic regime ( $Fr > 4$ ) shown in Figure 5b, it can be seen that the temperature of particle at the centreline and mid wall region are slightly lower than the gas phase, this is expected because of the shorter nominal reactor residence time as well as the low particle volume concentration at these regions. Meanwhile, at the near-wall region demonstrates that the temperature between both phases is almost equilibrium, while most of the particles stick close to the wall due to the strong inertia of the vortex flow as demonstrated in the CFD contour plot found in the supplementary material.

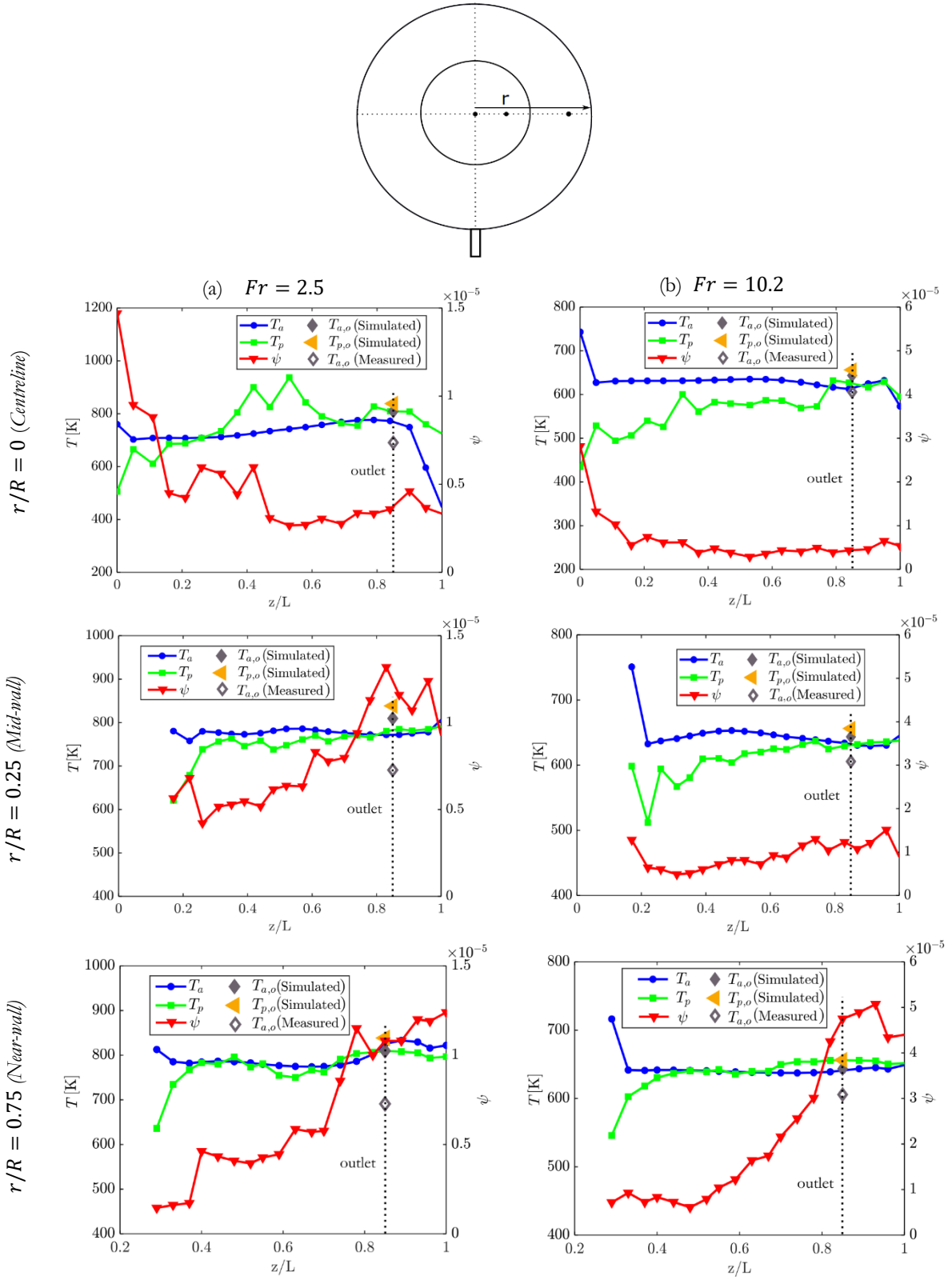


Figure 5: Simulated air and Particle Temperature along with particle volume concentration within the SEVR under a fixed particle size of  $155\mu\text{m}$  and particle loading, under the (a) Froude-Stokes and (b) cyclonic regime.

### 3.2.4 Effects on Particle Residence time

As shown in Figure 6a, at no tilt angle, it can be seen that the dimensionless residence time ( $\bar{\tau}_p/\tau_{nom}$ ) increases because of increment of tangential velocity component in the flow, this can be attributed with the increase of inertia as Stokes number is increased. Under the Froude-Stokes regime ( $Fr < 4$ ), the particles generally take a shorter residence time, this is because the particles tend to be suspended within the vortical flow before exiting. While in the cyclonic regime ( $Fr > 4$ ), the particle generally takes a longer time as particles under high speed are bounced off and flow along wall region. The trend of Froude number is similar to the trend of particle residence time in the isothermal case as demonstrated in the study of [30]. As shown in Figure 6b, as particle loading is increased, the dimensionless residence time also increases. This may be because the tangential velocity is reduced as more particles are introduced into the flow, as shown in the swirl intensity in Figure 6a, which shows a significantly reduced momentum to propel within the two-phase flow.

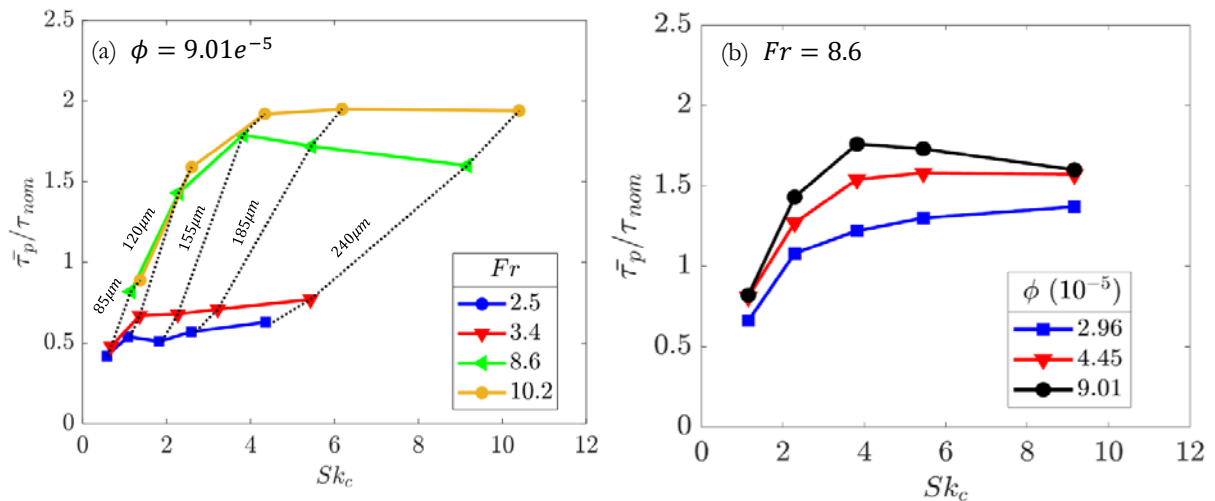


Figure 6: Simulated dimensionless particle residence time as a function of Stokes number within the SEVR as a function of (a) Froude number under a constant particle loading. (b) particle loading under a constant Froude number.



### 3.2.5 Effects on swirl intensity of the SEVR

Figure 7 presents the effects of different particle loading and Stokes number (i.e., particle size) on swirl intensity within the SEVR. CFD has been employed to determine the swirl intensity of the flow within the receiver, which aims to provide additional data to understand the particle residence time distribution as well as to demonstrate the influence of Stokes number on the distribution of particles within the device. The overall trend of both Figure 7a & 7b shows us that the swirl intensity is only distinguishable at the conical section. This implies that the impact of swirl intensity occurs at the conical region, where the flow undergoes momentum reduction due to the expansion of the geometry. Data obtained from numerical study as shown in Figure 7a shows that particle loading has an influence on the tangential momentum at  $z/L = 0.1$  within the receiver. This has shown that an increase in particle loading will result in the reduction of swirl intensity at  $z/L = 0.1$ , mainly due to the reduction of tangential velocity at the conical region, hence, this implies that the particle residence time is lengthen, which is expected to induce temperature drop between the two-phase flow. From Figure 7b, it was found that as the Stokes number increases, the swirl number also increases. This is the distribution of particles under a given Stokes number, for smaller particle sizes ( $Sk = 0.5, 1.2$ ), the swirl intensity tends to be weakened at the conical region while larger particles ( $Sk = 2.0, 2.7$ ) tends to have stronger swirl intensity as the mass of the larger particles can maintain the tangential momentum to the swirl intensity. Moreover, large particles will concentrate on the near-wall region, which will not affect the tangential velocity in the central region, while small particles are more uniformly distributed and, therefore, will reduce the high tangential velocity in the centre region.

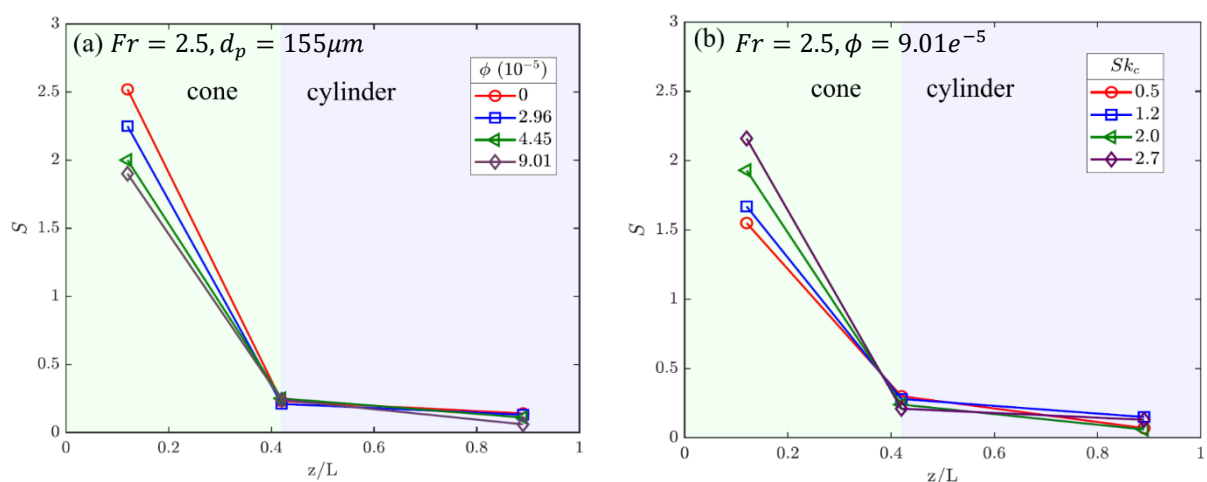
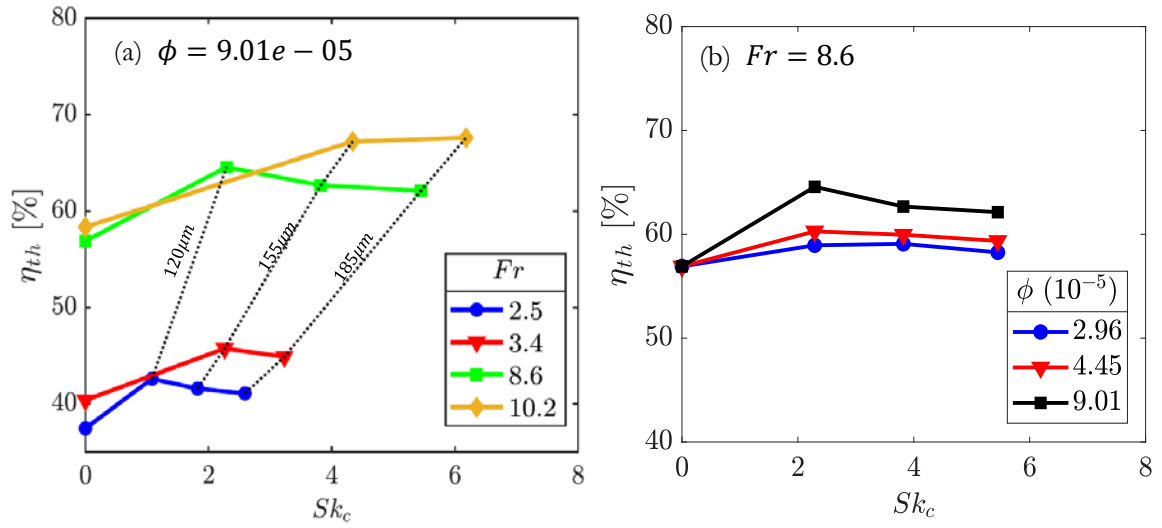


Figure 7. Simulated values of swirl number at positions ( $z/L = 0.18, 0.42, 0.89$ ) (a) particle loading with constant Froude number and particle size, (b) Stokes number (particle size) with constant particle loading and Froude number.

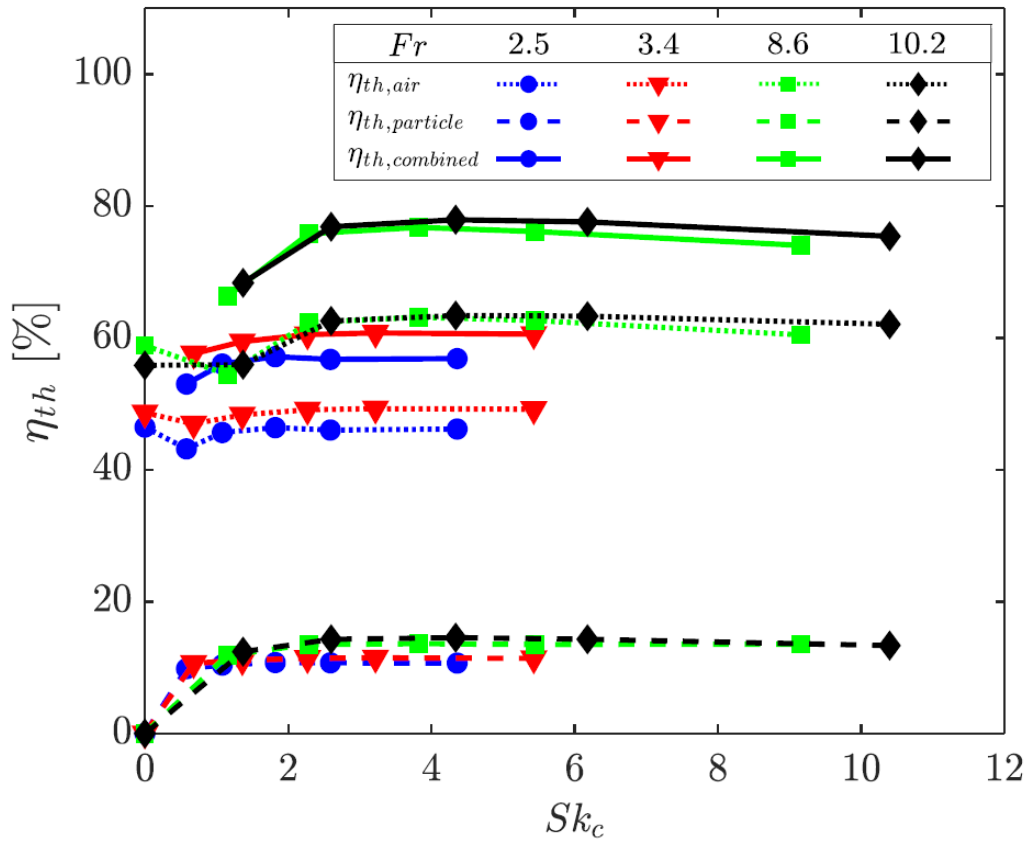
### **3.3 Thermal Performance and Heat Loss Mechanisms**

#### **3.3.1 Thermal Efficiency of the receiver**

Figure 8 presents the influence of Stokes number on the thermal efficiency of the SEVR. As shown in Figure 8a, the inlet flow velocity increases the Froude number, which results in an increased overall thermal efficiency, this is because the increase of inlet mass flowrate reduces the temperature rise. Figure 8b shows the dependence of thermal efficiency on particle loading, as the particle loading increases, the energy being absorbed by the particle phase increases due to the increment of particle mass flowrate as shown in Equation 4. Thus, this reduces the overall thermal energy being by the two-phase flow due to a reduction in temperature rise. Figure 8c shows the simulated CFD thermal efficiency, which shows the efficiency of the two-phase separately, alongside with the combined efficiency. It is interesting to note that the gas phase has nearly 4-8 times greater efficiency than the particle phase. It is also observed that by increasing the Stokes number would lead to the decrement of efficiency possibly due to particle deposition on the bottom part of the SEVR after colliding with the walls before exiting the receiver, which shows similar trend in Figure 8a. As shown in Figure 8d, it is also interesting to note that the gas phase efficiency is similar across all Stokes number, while the particle efficiency increases with the loading, this demonstrates that, under a fixed inlet velocity, the overall thermal efficiency of the device is only influenced by the particle loading.



(c)  $\phi = 9.01e^{-5}$



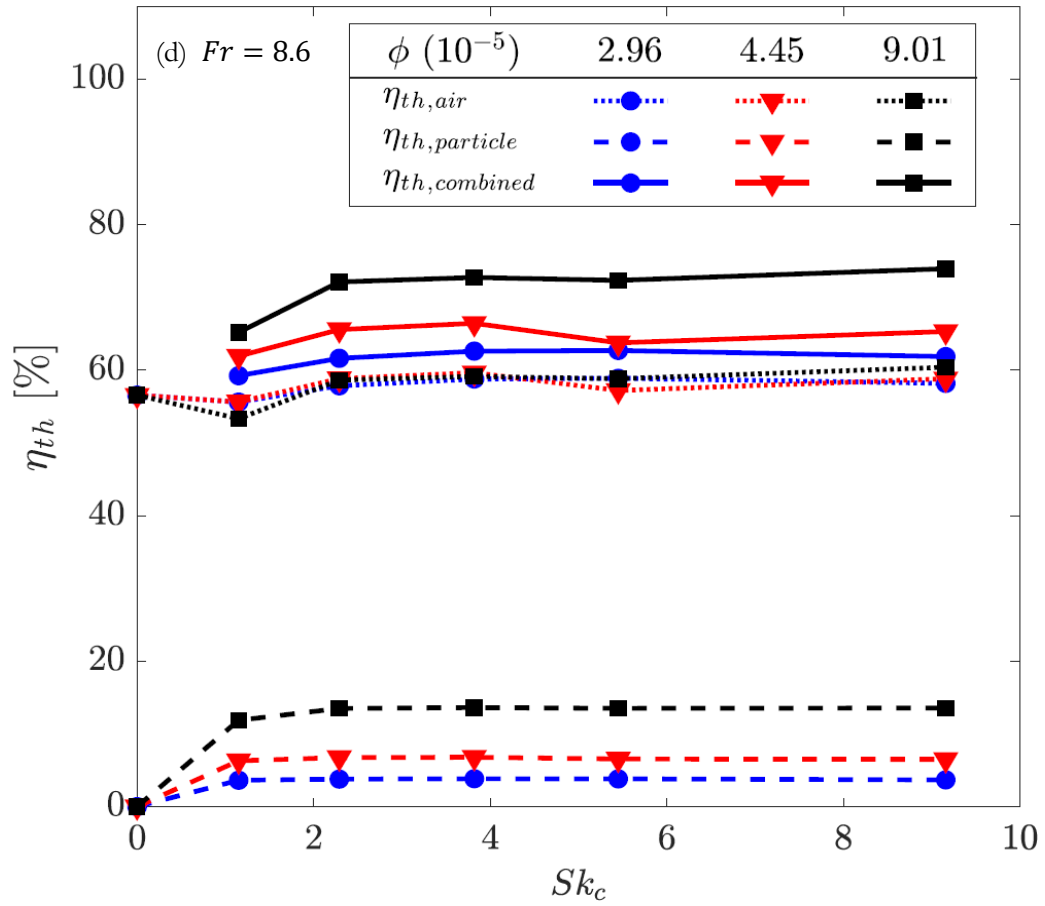


Figure 8: Thermal Efficiency within the SEVR as a function of Stokes number:  
 For experimental study: (a) Froude number for a constant particle loading (b) Particle loading for a constant Froude number.  
 For numerical study: (c) Froude number for a constant particle loading (d) Particle loading for a constant Froude number.

### 3.3.2 Normalised Enthalpy ratio of the receiver

Figure 9a & 9b shows that by normalising the enthalpy ratio on the air-to particle mass loading as a function of Stokes number, the Froude number and particle loading collapses well with the enthalpy ratio. This shows that the enthalpy ratio of the system is dependent on the particle loading, while Stokes number has a secondary influence on the enthalpy ratio. It is observed that for most of the cases reported in the figure, ratios between the normalised enthalpy of two phases have values less than unity. This demonstrates that more heat from the radiation lamps is eventually transferred to the gas phase than to the particle phase. Ultimately, increasing the particle mass under a fixed flowrate of the gas phase would increase this ratio, and potentially, the particle phase would absorb more energy through radiative means. The current configuration of this reactor is suitable for industrial application, but not limited to, reacting flow and air heating applications due to its ability to heat up air and particles consistently.

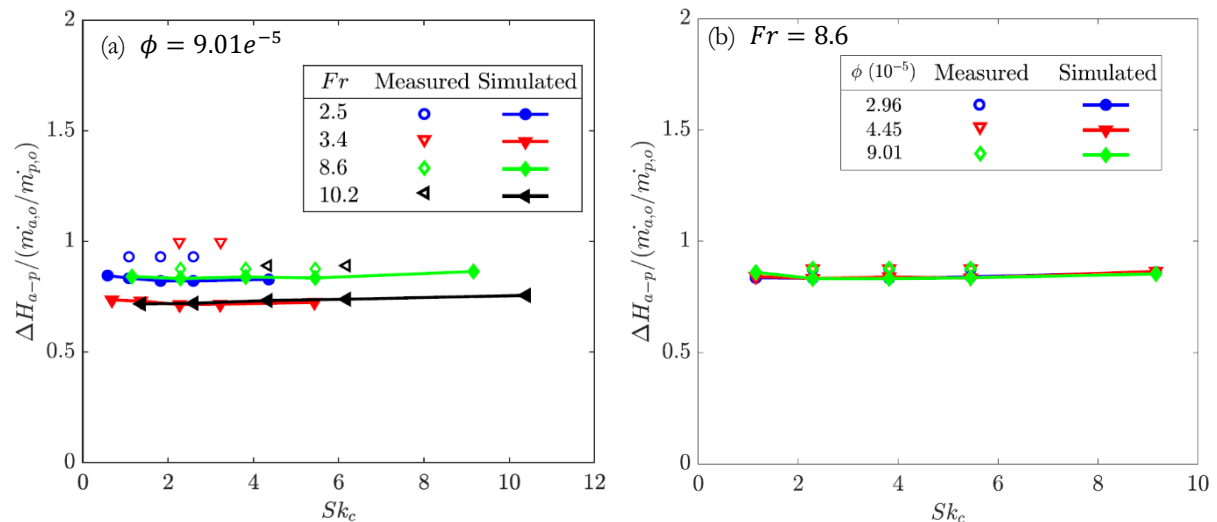


Figure 9: Derived values from experimental and numerical study of the normalized enthalpy ratio as a function of Stokes number with various (a) Froude number for a fixed particle loading. (b) Particle loading for a fixed Froude number.

### 3.3.3 Significance of the Radiative and Convective heat losses

Figure 10 shows the fraction of radiative and convective heat transfer losses through the aperture as specified in the energy balance equation with the variation of Froude number and particle loading based on experimental measurements. The dependency of Stokes number was not included as it does not present any significant difference for both radiative and convective heat loss terms. Similarly, the variation of operating parameters has very little influence on the conduction heat loss mechanism, mainly because the reactor has been well-insulated. Moreover, the conductive heat loss in the current laboratory-scale device is expected to be higher because

of the greater surface area to volume ratio of the device. It is expected that the effect of conductive heat loss would be significantly diminished as the reactor is scaled-up.

Figure 10 a-b shows the effects of Froude number on the fractions of radiative and convective heat losses as well as absorbed energy within the receiver. As shown in Figure 10a, it can be seen that the radiative heat loss reduces when the Froude number is increased. This is because at a lower Froude number, it is estimated that radiation losses through the aperture increases, namely, because more particles are suspended along the centreline are exposed directly to solar irradiation. In addition, the particle temperature is higher for low Froude number cases as more particles are exposed towards the centreline region despite a shorter particle residence time, which increases the radiation loss through the aperture. Hence, it is speculated that these particles reradiate the heat through the aperture allowing more radiant heat to be lost through the aperture. Meanwhile, under the cyclonic regime, the particles are centrifuged closely to the receiver wall, the absence of particles on the centreline region allows greater penetration of radiation to inner region of the device, which lessens the radiative losses through the aperture as majority of the radiant energy has been absorbed by both the wall and two-phase flow. The convective heat losses shown in Figure 10b through the aperture is increased due to the reduced temperature at the outlet section. As the inlet flow velocity is increased, air exchange through the aperture also increases as observed in the single-phase flow-field study [44], which results in greater convective heat loss through the aperture as ambient cold air is being mixed with the egressed hot air in the reactor through flow recirculation. For the current study, the Nusselt number was not assessed due to the high uncertainty level of heat loss from conduction, as reflection losses from the receiver is challenging to predict. Figure 10 c-d shows the coupling effects of particle loading on the heat transfer within the receiver. As shown in Figure 10c, it can be observed as the particle loading is increased, the reradiating losses through the aperture is reduced, this is because the higher loading of particles captures more radiant energy from the solar flux. Similarly, the particle temperature is lower for higher particle loading, and therefore reduces the radiative heat losses through the aperture. As shown in Figure 10d, the convective heat losses are reduced as the energy is being absorbed by the particles due to the longer particle residence time. Overall, the convective heat loss is greater than the radiative heat loss, as the current outlet temperature of the receiver is at a lower level (300 °C ~ 450 °C). However, the trend is expected to vary when temperature within the receiver is further elevated, eventually allowing radiative heat loss to dominate over convection losses. This is mainly

because radiative heat losses increase non-linearly with temperature (i.e., given that temperature has a power of fourth-order in radiation loss).

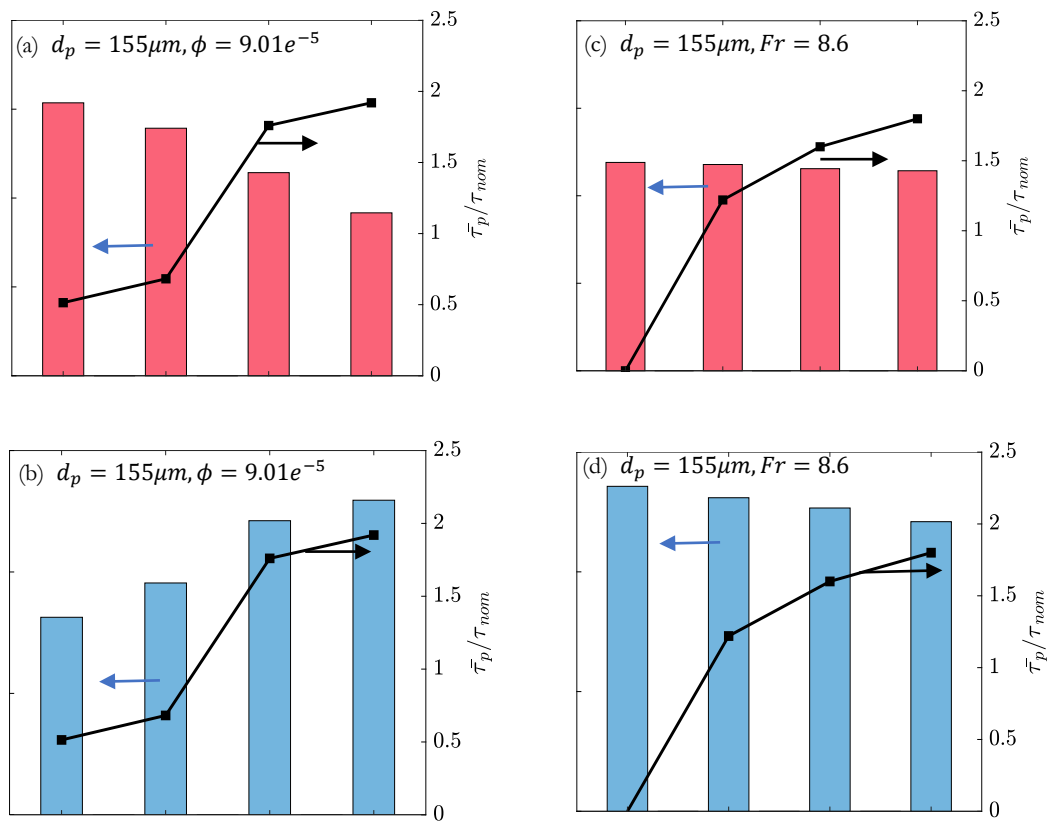


Figure 10:

- (a) Measured radiative heat loss through the aperture and simulated dimensionless particle residence time for different Froude number at a given particle loading and size.
- (b) Measured convective heat loss through the aperture and simulated dimensionless particle residence time for different Froude number at a given particle loading and size.
- (c) Measured radiative heat loss through the aperture and simulated dimensionless particle residence time for different particle loading at a given Froude number and particle size.
- (d) Measured convective heat loss through the aperture and simulated dimensionless particle residence time for different particle loading at a given Froude number and particle size.

## 4 Conclusion

The key outcomes of the current study are as follows:

- The particle loading has a strong influence on the particle residence time and thermal efficiency of the device. This is because the higher particle loading reduces the swirl intensity within the two-phase flow, which allow particles to dwell in the device for longer periods.
- Under the Froude-Stokes regime, the presence of more particles at the centreline region coupled with the direct absorption of incoming radiation through the aperture and flow recirculation allows convective heat transfer in the reactor wall and particles to be more

uniformly distributed. This is evident as the temperature distribution of the gas phase within the reactor is nearly equilibrium between the two-phases along the radial distance ( $r/R$ ). The flow recirculation contributes to better mixing of particles and gas within the device. However, radiation losses are expected to be much higher due to reradiation from particles through the aperture.

- Meanwhile, the cyclonic regime shows that the particles are centrifuged closely to the receiver wall; the absence of particles on the centreline region allows better penetration of radiation to the aperture end of the device as the flux profile is nearly Gaussian distributed. This results in a lowered particle temperature at the centreline and mid-wall region because of the lower particle volume concentration. In contrast, near-wall regions demonstrate that temperature between the two-phases are almost of equilibrium, since most particles flow in the near wall region due to the strong inertia generated by the vortex flow.
- The ratio of the normalised enthalpy between the two phases shows that more convective and radiative heat is being transferred from the particle phase to the gas phase. The mixing of two-phases shows that this is beneficial for an industrial reactor but is not limited to potential applications in air heating and reacting flows. It is as expected that the two-phase mixing will increase with scale due to the greater residence time. Hence, a preliminary hypothesis predicts that the reactor can potentially operate as a particle reactor.
- The Froude number (i.e, flow velocity) has significant influence on the convective heat loss through the receiver aperture. As the Froude number increases, the rate of air exchanged at the aperture also increases, despite the same air ingress rates (33% for the cases in this study). This is as expected because the flow recirculation allows more hot air from within the cavity to egress through the aperture, while cold ambient air ingresses the device through back mixing from the recirculating flow, which increases the convective heat loss at the aperture plane. To reduce further convective heat loss through the aperture, a flow mitigation technique is necessary to reduce hot air egress while preventing cold air ingress through the aperture.
- The CFD results of the current lab-scale receiver have predicted that the temperature difference between the two phases has little to no changes. However, it is expected that the temperature difference between the two phases may be more significant in a scaled-up device. This is because the increased reactor volume allows greater radiant heat absorption and residence time for the particle phase and therefore temperature of



particles can be much higher than that of the local air phase. Hence, further modelling is required to understand the heat transfer between the two-phase in the SEVR at scale.

### Acknowledgements

The author gratefully acknowledges the financial support of the Australian Renewable Energy Agency, ARENA, through the RND054 Bayer program as well as the Divisional Scholarship provided by the Faculty of ECMS, University of Adelaide. The author would also like to thank Dr Timothy Lau, Dr Zhiwei Sun and Mr Yining Tang for their constructive feedback throughout the experimental and numerical study.

### Nomenclature

$L$	Receiver Length [mm]
$D_c$	Receiver Diameter [mm]
$\theta$	Cone angle [°]
$d_{ap}$	Aperture diameter [mm]
$r_{ap}$	Aperture radius [mm]
$d_{in}$	Inlet jet diameter [mm]
$d_{out}$	Outlet jet diameter [mm]
$P_{sp}$	Particle Sphericity
$L_{ins}$	Insulation thickness [mm]
$k$	Thermal conductivity [W/mK]
$c_{p,p}$	Particle specific heat capacity [kJ/kg]
$c_{p,a}$	Air specific heat capacity [kJ/kg]
$\varepsilon_p$	Emissivity of Particle
$\varepsilon_{eff}$	Emissivity of reactor wall
$\dot{V}_{in}$	Inlet volumetric flow rate [SLPM]
$U_{in}$	Inlet flow velocity [m/s]
$\dot{V}_{out}$	Outlet volumetric flow rate [SLPM]
$U_{out}$	Outlet flow velocity [m/s]
$d_p$	Mean particle diameter [ $\mu m$ ]
$\dot{m}_{a,i}$	Air mass flowrate at the inlet [kg/s]
$\dot{m}_{a,o}$	Air mass flowrate at the outlet [kg/s]
$\dot{m}_{p,i}$	Particle mass flowrate at the inlet [kg/s]

$\dot{m}_{p,o}$	Particle mass flowrate at the outlet [kg/s]
$Fr$	Froude number
$Sk_c$	Stokes number
$\phi$	Inlet particle volumetric loading
$T_w$	Wall temperature [K]
$T_{a,o}$	Outlet air temperature [K]
$T_{p,o}$	Outlet particle temperature [K]
$T_{a,o,tp}$	Outlet air temperature of the two-phases in CFD [K]
$\Delta T_{p-a,o}$	Temperature difference between particle and gas [K]
$T_a$	Air temperature within the receiver [K]
$T_p$	Particle temperature within the receiver [K]
$\omega$	Particle volume fraction within the receiver
$\dot{Q}_s$	Input Solar Flux [kW]
$\alpha$	Net Air Ingress/Egress [%]
$\dot{Q}_{abs}$	Energy Absorbed [W]
$\dot{Q}_{cond}$	Conductive heat loss [W]
$\dot{Q}_{loss,ap,conv}$	Convective heat loss through aperture [W]
$\dot{Q}_{loss,ap,rad}$	Radiative heat loss through aperture [W]
$\eta_{th}$	Thermal Efficiency [%]
$\eta_{th,air}$	Thermal Efficiency of gas phase [%]
$\eta_{th,particle}$	Thermal Efficiency of particle phase [%]
$\Delta H_{a-p}$	Enthalpy ratio
$\Delta T_{p-a,o}$	Temperature difference between two-phases [K]
$U_{t,max}$	Maximum tangential velocity [m/s]
$\bar{\tau}_p$	Mean particle residence time [s]
$\tau_{nom}$	Nominal particle residence time [s]
$V_R$	Internal volume of receiver [m <sup>3</sup> ]
$S$	Swirl number
$\psi$	Particle volume concentration

## Abbreviations

CFD	Computational Fluid Dynamics
SVR	Solar Vortex Receiver
SEVR	Solar Expanding Vortex Receiver
CSR	Concentrated solar radiation

## References

- [1] IEA (2020) WEO, IEA, Paris <https://www.iea.org/reports/world-energy-outlook-2020>.
- [2] Ellabban O, Abu-Rub H, Blaabjerg F. Renewable energy resources: Current status, future prospects and their enabling technology. *Renewable and Sustainable Energy Reviews*. 2014;39:748-64.
- [3] Pedraza J, Zimmermann A, Tobon J, Schomäcker R, Rojas N. On the road to net zero-emission cement: Integrated assessment of mineral carbonation of cement kiln dust. *Chemical Engineering Journal*. 2021;408:127346.
- [4] Eglinton T, Hinkley J, Beath A, Dell'Amico M. Potential applications of concentrated solar thermal technologies in the Australian minerals processing and extractive metallurgical industry. *Jom*. 2013;65:1710-20.
- [5] Wang P, Ryberg M, Yang Y, Feng K, Kara S, Hauschild M, et al. Efficiency stagnation in global steel production urges joint supply- and demand-side mitigation efforts. *Nature Communications*. 2021;12:2066.
- [6] Wang W, Shuai Y, Lougou BG, Jiang B. Thermal performance analysis of free-falling solar particle receiver and heat transfer modelling of multiple particles. *Applied Thermal Engineering*. 2021;187:116567.
- [7] Ho CK, Iverson BD. Review of high-temperature central receiver designs for concentrating solar power. *Renewable and Sustainable Energy Reviews*. 2014;29:835-46.
- [8] Coventry J, Arjomandi M, Asselineau C-A, Chinnici A, Corsi C, Davis D, et al. Development of ASTRI high-temperature solar receivers. *AIP Conference Proceedings: AIP Publishing LLC*; 2017. p. 030011.
- [9] Ebert M, Amsbeck L, Rheinländer J, Schlögl-Knothe B, Schmitz S, Sibum M, et al. Operational experience of a centrifugal particle receiver prototype. *AIP Conference Proceedings: AIP Publishing LLC*; 2019. p. 030018.
- [10] Ho CK. A review of high-temperature particle receivers for concentrating solar power. *Applied Thermal Engineering*. 2016;109:958-69.
- [11] Tregambi C, Troiano M, Montagnaro F, Solimene R, Salatino P. Fluidized Beds for Concentrated Solar Thermal Technologies—A Review. *Frontiers in Energy Research*. 2021;9.
- [12] Kodama T, Bellan S, Gokon N, Cho HS. Particle reactors for solar thermochemical processes. *Solar Energy*. 2017;156:113-32.
- [13] Wu S-Y, Xiao L, Cao Y, Li Y-R. Convection heat loss from cavity receiver in parabolic dish solar thermal power system: A review. *Solar energy*. 2010;84:1342-55.
- [14] Abbasi-Shavazi E, Hughes G, Pye J. Investigation of heat loss from a solar cavity receiver. *Energy Procedia*. 2015;69:269-78.
- [15] Venkatachalam T, Cheralathan M. Effect of aspect ratio on thermal performance of cavity receiver for solar parabolic dish concentrator: An experimental study. *Renewable Energy*. 2019;139:573-81.
- [16] Loni R, Asli-Areh EA, Ghobadian B, Kasaeian A, Gorjian S, Najafi G, et al. Research and review study of solar dish concentrators with different nanofluids and different shapes of cavity receiver: Experimental tests. *Renewable Energy*. 2020;145:783-804.
- [17] Z'Graggen A, Haueter P, Maag G, Vidal A, Romero M, Steinfeld A. Hydrogen production by steam-gasification of petroleum coke using concentrated solar power: reactor experimentation with slurry feeding. *International Solar Energy Conference 2006*. p. 23-7.

- [18] Chinnici A, Arjomandi M, Tian Z, Lu Z, Nathan GJ. A novel solar expanding-vortex particle reactor: influence of vortex structure on particle residence times and trajectories. *Solar Energy*. 2015;122:58-75.
- [19] Sarker M, Mandal S, Tuly SS. Numerical study on the influence of vortex flow and recirculating flow into a solid particle solar receiver. *Renewable Energy*. 2018;129:409-18.
- [20] Elghobashi S. On predicting particle-laden turbulent flows. *Applied scientific research*. 1994;52:309-29.
- [21] Jaber F. Temperature fluctuations in particle-laden homogeneous turbulent flows. *International Journal of Heat and Mass Transfer*. 1998;41:4081-93.
- [22] Z'Graggen A, Steinfeld A. Hydrogen production by steam-gasification of carbonaceous materials using concentrated solar energy—V. Reactor modeling, optimization, and scale-up. *international journal of hydrogen energy*. 2008;33:5484-92.
- [23] Z'Graggen A, Haueter P, Maag G, Vidal A, Romero M, Steinfeld A. Hydrogen production by steam-gasification of petroleum coke using concentrated solar power—III. Reactor experimentation with slurry feeding. *International Journal of Hydrogen Energy*. 2007;32:992-6.
- [24] Trommer D, Hirsch D, Steinfeld A. Kinetic investigation of the thermal decomposition of CH<sub>4</sub> by direct irradiation of a vortex-flow laden with carbon particles. *International Journal of Hydrogen Energy*. 2004;29:627-33.
- [25] Hathaway BJ, Davidson JH. Demonstration of a prototype molten salt solar gasification reactor. *Solar Energy*. 2017;142:224-30.
- [26] Müller FL. *Solar Reactor Development for Thermochemical Gasification and Calcination Processes*: ETH Zurich; 2018.
- [27] Koepf E, Villasmil W, Meier A. High temperature flow visualization and aerodynamic window protection of a 100-kWth solar thermochemical receiver-reactor for ZnO dissociation. *Energy Procedia*. 2015;69:1780-9.
- [28] Chinnici A, Davis D, Lau TC, Tian ZF, Saw W, Nathan GJ. First-of-a-kind investigation on performance of a directly-irradiated windowless vortex-based particle receiver. *AIP Conference Proceedings*: AIP Publishing LLC; 2020. p. 140002.
- [29] Davis D, Jafarian M, Chinnici A, Saw WL, Nathan GJ. Thermal performance of vortex-based solar particle receivers for sensible heating. *Solar Energy*. 2019;177:163-77.
- [30] Davis D, Troiano M, Chinnici A, Saw WL, Lau T, Solimene R, et al. Particle residence time distributions in a vortex-based solar particle receiver-reactor: An experimental, numerical and theoretical study. *Chemical Engineering Science*. 2020;214:115421.
- [31] Davis D, Troiano M, Chinnici A, Saw WL, Lau T, Solimene R, et al. Particle residence time distributions in a vortex-based solar particle receiver-reactor: The influence of receiver tilt angle. *Solar Energy*. 2019;190:126-38.
- [32] Kitzmiller KW. *Design, construction, and initial testing of a solar simulator and lab-scale small particle solar receiver*: Engineering; 2013.
- [33] Krueger KR. *Design and characterization of a concentrating solar simulator*: University of Minnesota; 2012.
- [34] Moumin G, Tescari S, Sundarraj P, de Oliveira L, Roeb M, Sattler C. Solar treatment of cohesive particles in a directly irradiated rotary kiln. *Solar Energy*. 2019;182:480-90.
- [35] Tescari S, Sundarraj P, Moumin G, Duarte JPR, Agrafiotis C, de Oliveira L, et al. Solar rotary kiln for continuous treatment of particle material: Chemical experiments from micro to milli meter particle size. *AIP Conference Proceedings*: AIP Publishing LLC; 2020. p. 140007.
- [36] Steinfeld A, Schubnell M. Optimum aperture size and operating temperature of a solar cavity-receiver. *Solar Energy*. 1993;50:19-25.
- [37] Marchioli C, Picciotto M, Soldati A. Particle dispersion and wall-dependent turbulent flow scales: implications for local equilibrium models. *Journal of Turbulence*. 2006:N60.

- [38] Tian ZF, Nathan GJ, Cao Y. Numerical modelling of flows in a solar-enhanced vortex gasifier: Part 1, comparison of turbulence models. *Progress in Computational Fluid Dynamics, an International Journal*. 2015;15:114-22.
- [39] ANSYS Inc. ANSYS CFX Users Guide 19.1. 2019.
- [40] Lau TC, Nathan GJ. Influence of Stokes number on the velocity and concentration distributions in particle-laden jets. *Journal of Fluid Mechanics*. 2014;757:432-57.
- [41] Cortes C, Gil A. Modeling the gas and particle flow inside cyclone separators. *Progress in Energy and Combustion Science*. 2007;33:409-52.
- [42] Shilapuram V, Krishna DJ, Ozalp N. Residence time distribution and flow field study of aero-shielded solar cyclone reactor for emission-free generation of hydrogen. *international journal of hydrogen energy*. 2011;36:13488-500.
- [43] Gupta AK, Lilley DG, Syred N. *Swirl flows*. Tunbridge Wells. 1984.
- [44] Long S, Lau TC, Chinnici A, Nathan GJ. The flow-field within a vortex-based solar cavity receiver with an open aperture. *Experimental Thermal and Fluid Science*. 2021;123:110314.